# Laserspektroskopische Untersuchungen zur Stickoxid - Bildung an einem optisch zugänglichen Viertakt-Ottomotor mit Direkteinspritzung

# Laser-Spectroscopic Investigations of Nitric Oxide Formation in a Transparent Spark Ignited Engine with Direct Injection

von
Dipl.-Ing. Udo Fissenewert
aus Minden

von der Fakultät V – Verkehrs– und Maschinensysteme
der Technischen Universität Berlin
zur Erlangung des akademischen Grades

Doktor der Ingenieurwissenschaften
– Dr.-Ing.–

genehmigte Dissertation

Promotionsausschuss:

Vorsitzender: Prof. Dr-Ing. P. U. Thamsen
Gutachter: Prof. Dr.-Ing. H. Pucher
Gutachter: Prof. Dr. rer. nat. V. Sick

Tag der wissenschaftlichen Aussprache: 19. August 2005

**BERLIN 2005**
**D 83**

## Acknowledgements

This work was facilitated by the help and support of many people; I would have not been able to complete it without them. First and foremost I like to thank Professor Dr. Volker Sick for being such an exceptional advisor. He encouraged me in every way possible. His suggestions and support were crucial in completion of this project. I also like to thank Professor Dr. Helmut Pucher for his evaluation of this thesis.

My gratitude goes out to Dr. Nicole Wermuth for all her help and advice during the experiments, the development of the heat release program and many fruitful discussions. In addition, I would like to express my appreciation towards my current and former colleagues from the quantitative laser diagnostics lab: Dr. Boris Stojkovic, Dr. Mong Tung Lin, Dr. Charlie Funk, Doug Frieden, Fabrice Ponti, Jay Smith, Rui Zhang, Claudia Fajardo, Vinod Natarajan, Jordan Snyder, Brian Petersen and Jessamyn Margoni.

Further I am obliged to Dr. David Reuss for sharing his vast experience during the design and setup of the optical engine. In this context I would like to thank the technical staff of the Auto Lab: John Mears, Bill Kirkpatrick, and Kent Pruss; as well as the administrative staff: Susan Clair and Janet Lyons.

A big thank you goes out to the friends I made during the years at the UM: Dr. Aristotelis Babajimopoulos, Christos Chryssakis, Dr. Guntram Lechner, Alexander Knafl, as well as Jason Martz. It just would not have been the same without them.

Also I like to acknowledge the financial, technical and scientific support that was provided by the General Motors collaborative research lab, from which so many grad students benefit. Finally I would like to express my thankfulness for the loving support of my wife as well as my parent's during this enterprise.

## Contents

## Summary

The spatial and temporal formation of nitric oxide in an optical engine operated with iso-octane fuel under spray-guided direct-injection conditions was studied with a combination of laser-induced fluorescence imaging, UV-chemiluminescence, and cycle resolved NO exhaust gas analysis.

Initially an appropriate experimental apparatus had to be developed consisting of an optically accessible engine and necessary instrumentation. Therefore a single cylinder engine with optical access was designed and built. Key features are the custom made fully balanced crankcase made by FEV, a Bowditch-style elongated piston with interchangeable crown, a cylinder head with windows in the flat sides of the pentroof, and a quartz cylinder liner covering the full stroke. The spray guided combustion system required a dished piston. A significant part of the combustion takes place in the piston bowl thus making it necessary to implement side windows in addition to the window in the piston top.

The optical engine was the precondition for the application of optical diagnostics methods for investigations of a spray-guided direct injection combustion system. Cycle-resolved simultaneous measurements of OH-chemiluminescence, NO laser induced fluorescence, and fast NO exhaust gas sampling allowed a detailed view of the formation process of NO in this engine.

A detailed analysis of uncertainties of the NO-LIF measurements was conducted and their impact on the accuracy of the results quantified. The major contributors are absorption of laser and signal light by $H_2O$ and $CO_2$ and signal quenching due to its dependence on the unknown local burned gas – temperature and – composition.

NO formation during early and late (homogeneous vs. stratified) injection conditions were compared. Strong spatial preferences and cyclic variations in the NO formation were observed depending on engine operating conditions. While engine-out NO levels are substantially lower for stratified engine operation, cyclic variations of NO formation are substantially higher than for homogeneous, stoichiometric operation.

The influence of variations in intake air temperature and simulated exhaust gas recirculation was examined. Overall, it was found that cycle-resolved information is

needed to explain the differences found between operating conditions, since the initial high stratification of fuel leads to large spatial gradients in the NO concentration. Averaged in-cylinder NO distributions do not adequately reflect the formation process rather than show a smoothed distribution that may even be counter-intuitive based on averaged chemiluminescence data. The strong impact of the high level of fuel stratification is also reflected in the temporal evolution of the in-cylinder NO concentrations. Spatially averaged peak concentrations can reach 2700 ppm for engine operation with 90 °C intake air temperature and no EGR. This compares to approximately 300 ppm as measured in the exhaust gas. This ratio is high for spark-ignition engines. However, given the high level of fuel stratification in this spray-guided engine, the observations are plausible and are supported by the measured high local concentrations of NO.

## Zusammenfassung

Die räumliche und zeitliche Stickoxidbildung wurde in einem optisch zugänglichen, direkteinspritzendem Ottomotor mit strahlgeführtem Brennverfahren untersucht. Dazu wurde eine Kombination von Laser-induzierter Fluoreszenz, UV-Chemilumineszenz und zyklusaufgelöster NO-Abgasanalyse eingesetzt.

Zunächst ist ein passender experimenteller Aufbau, bestehend aus einem Transparentmotor und der notwendigen Instrumentierung, entwickelt worden. Dazu musste ein Einzylinder-Motor mit optischem Zugang entworfen und aufgebaut werden. Schlüsseleigenschaften sind das nach Vorgaben von der FEV gefertigte Kurbelgehäuse mit vollständigem Massenausgleich, ein verlängerter „Bowditch"- Kolben mit auswechselbarem Oberteil, ein Zylinderkopf mit Fenstern in den flachen Seiten des dachförmigen Brennraumes und ein Quarz-Zylinderrohr, das den vollen Hub abdeckt.

Das strahlgeführte Brennverfahren erfordert eine Kolbenmulde. Da ein erheblicher Teil der Verbrennung in der Mulde stattfindet, war es nötig, diese zusätzlich zum Fenster im Kolbenboden mit seitlichen Fenstern zu versehen.

Der optische Motor war die Voraussetzung, um optische Diagnose-Methoden zur Untersuchung des strahlgeführten Brennverfahrens anwenden zu können. Zyklus-aufgelöste, simultane Messungen der OH-Chemilumineszenz und der NO-Konzentration mit Hilfe der Laser-induzierten Fluoreszenz, und schneller NO-Abgasanalyse ermöglichten eine ausführliche Darstellung des Stickoxid –Bildungsprozesses in diesem Motor. Die Haupt-Fehlerquellen sind die Absorption von Laser- und Signallicht durch $CO_2$ und $H_2O$ und Fluoreszenzlöschung aufgrund der Abhängigkeit von den nicht bekannten Werten von lokaler Abgas-Temperatur und –Zusammensetzung.

Die NO-Bildung bei früher und später Einspritzung (homogen und geschichtet) wurde verglichen. Starke räumliche Präferenzen und zyklische Schwankungen der NO-Bildung wurden abhängig vom Betriebsmodus des Motors beobachtet. Während die absolute Höhe der NO-Konzentration im Abgas im geschichteten Betrieb wesentlich niedriger ist, sind die zyklischen Schwankungen deutlich höher als im homogenen, stöchiometrischen Betrieb. Der Einfluss der Einlaßlufttemperatur und der simulierten Abgasrückführung wurde untersucht. Insgesamt wurde festgestellt, dass zyklusaufgelöste Daten erforderlich

sind, um die Unterschiede zu erklären, die zwischen den Betriebsbedingungen gefunden wurden, da die ausgeprägte Schichtung des Kraftstoffs zu großen räumlichen Gradienten der NO-Konzentration führt. Gemittelte NO-Verteilungen im Zylinder reflektieren den Bildungsprozess nur unzureichend, sondern zeigen eine geglättete Verteilung, die den gemittelten Chemilumineszenz-Daten zufolge sogar intuitiv widerspricht. Der starke Einfluß der ausgeprägten Kraftstoffschichtung wird auch von der zeitlichen Entwicklung der NO-Konzentrationen im Zylinder reflektiert. Räumlich gemittelte Höchstkonzentrationen können 2700 ppm für den Betriebspunkt mit 90 °C Einlass-Lufttemperatur ohne EGR erreichen. Im Vergleich dazu werden ungefähr 300 ppm im Abgas gemessen. Dieses Verhältnis ist für Ottomotoren hoch. Zieht man jedoch die starke Ladungsschichtung des strahlgeführten Brennverfahrens in Betracht, dann sind die Beobachtungen plausibel und werden durch die gemessenen hohen lokalen Konzentrationen untermauert.

# 1 Introduction

Growing environmental concerns, such as global warming due to the emission of the greenhouse gas $CO_2$ by automotive power plants, lead to the need for cleaner and fuel saving combustion systems. Direct injection combustion systems applied to the spark ignited engine might be a way to improve the efficiency particularly by reducing pumping and heat losses during part load while maintaining the advantages of high power density and engine speeds during high loads [Zhao, Lai et al., 1999]. Initially, wall guided combustion systems were pursued, but high hydrocarbon and soot emissions led to the investigation of spray guided systems. Here a higher degree of stratification is possible, which yields improved emissions [Drake, Fansler et al., 2004; Honda, Kawamoto et al., 2004]. Nonetheless, due to high oxygen availability and locally rich mixture, the nitric oxide formation is comparably high. This is detrimental as the widely employed exhaust aftertreatment by a three way catalytic converter is inefficient for overall lean mixtures. NO storage catalytic converters are widely employed, but require rich exhaust gas to reduce the stored NO. This is generated by operating the engine homogeneous-rich for a brief period of time, which of course comes with a fuel consumption penalty [Tamura, Kikuchi et al., 2001; Krebs, Pott et al., 2002]. A reduction of in-cylinder nitric oxide is desirable to minimize the number of regeneration cycles. Hence the understanding of in-cylinder NO formation is important, so that the necessary scientific background for improvement of the combustion system is provided. An assessment of the NO formation process inside the engine exclusively by drawing conclusions from engine out emissions is difficult, because of the highly inhomogeneous nature of the stratified charge combustion process. Also, due to high cyclic variability cycle resolved measurements are desirable, which conventional emissions analyzers are not capable of.

There are a number of fast NO analyzers, that can sample from high pressure environments, e.g. the fast chemiluminescence detector from Cambustion. This device has been employed for the experiments described in this thesis to measure cycle resolved engine out NO concentrations. Although this device proved very useful for this purpose, it can only deliver in-cylinder measurements for a part of the high pressure cycle

[Peckham, Hands et al., 1998b; Peckham, Hands et al., 1998a]. This problem is remedied when using fast gas sampling valves. However, these valves only provide volume-integrated measurements. Less important setbacks are that they time integrate over a number of crank angles, and even mix sampling gas from different cycles. Thus only an averaged time history can be measured [Müller and Zillmer, 1998; Zhao and Ladommatos, 2001; Corcione, Merola et al., 2002; Suck, Jakobs et al., 2004].

The imaging of laser induced fluorescence (LIF) of nitric oxide provides a measure of a two-dimensional distribution inside the cylinder. Moreover, with laser pulses as short as 20 ns the imaging is almost instantaneous. So, cyclic variability can be assessed with the limitation that only one image per cycle can be taken, due to the slow readout of the camera chip and the repetition rate of the laser. Due to the highly inhomogeneous nature of the stratified charge combustion process, high spatial variation of the NO concentration inside the cylinder is to be expected. Laser induced fluorescence can be used to visualize local high NO concentrations.

There are inherent difficulties in applying laser diagnostics inside an engine, such as absorption of laser light and signal mostly by $H_2O$ and $CO_2$ and background signals from $O_2$, $CO_2$ and PAH. A number of excitation and detection techniques have been suggested to reduce the intrinsic problems of this measurement method as described above. [Stoffels, Boom et al., 1999] obtained qualitative NO measurements in a diesel engine by employing a tunable ArF excimer laser to excite the D-X (0,1) band at 193nm. The Laser beam was attenuated significantly by the commercial diesel fuel and combustion products during the high pressure phase. [Dec and Canaan, 1998] were able to reduce the absorption of the laser beam by operating their diesel engine with low-sooting fuel. In this case A-X (0,0) excitation at 225 nm was employed with light from an optical parametric oscillator (OPO). Previously, [Schulz, Yip et al., 1995] reported the first attempt to use the A-X (0,2) band. They concluded that their strategy had some advantages compared to the aforementioned excitation strategies. The O12 bandhead within this band corresponds to a minimum of the $O_2$ B-X transition thus improving selectivity. The absorption of the laser beam by combustion products is reduced compared to excitation in the A-X(0-0) band. [Hildenbrand, Schulz et al., 1999] showed that blue shifted detection features superior interference suppression of PAH and $CO_2$

LIF. Advantages and disadvantages of different excitation/detection strategies have been discussed in detail in a series of recent articles [Bessler, Schulz et al., 2002; Bessler, Schulz, Lee et al., 2003a; Bessler, Schulz, Lee et al., 2003b] . Common to all excitation detection schemes is that the signal depends on pressure, temperature and gas composition, thus further complicating the application of this measurement technique to engines. Quantification is complicated but very well feasible.

In the work presented, NO-LIF imaging with excitation through an excimer laser at 248 nm, OH imaging and cycle resolved exhaust gas measurements of NO concentrations have been conducted simultaneously. With these techniques the formation of nitric oxide in a transparent single cylinder engine featuring a spray guided combustion system was assessed. While NO-LIF and the exhaust gas measurements provide direct information about NO concentrations, the imaging of the naturally occurring UV light emitted by the hydroxyl radical is an indicator for the spatial development of the flame front. This is a well established technique that has been successfully applied to stratified charge engines [Drake, Fansler et al., 2004; Stojkovic, Fansler et al., 2004]. OH is a precursor of NO via the extended Zeldovich mechanism, so the OH-chemiluminescence is, to some extent, an indirect measure for NO.

Initially, this thesis introduces the reader to the theoretical background of the topics relevant to the work presented. Chapter 2 reviews the chemical mechanisms of nitric oxide formation and destruction during technical combustion processes.

The technology of the spark ignited, direct injected gasoline engine is reviewed in Chapter 3, with focus on the spray guided combustion system.

Chapter 4 establishes the fundamentals of the optical techniques employed in the experiments described in this thesis. The spectroscopic principle of LIF as well as the mathematical model necessary for the quantification is explained. The most important issues in detecting nitric oxide with LIF are summarized. The imaging of the NO-LIF is complemented with imaging of the naturally occurring UV light emitted by the hydroxyl radical formed during the combustion process. A brief introduction to OH chemiluminescence has been included.

A description of the experimental setup can be found in setup in Chapter 5, with focus on the development of the optical engine and its unique features. The instrumentation and

data acquisition as well as the optical diagnostics are concisely introduced. Chapter 6 elaborates on the operation conditions that were investigated. Initially injection and ignition timings had to be found for various amounts of EGR and intake air temperatures. An overview of the experiments conducted can be found there as well. The processing of the data obtained is discussed in Chapter 7. The data reduction of the signal obtained with the fast NO analyzer is explained. The procedure of NO-LIF quantification is laid out. The uncertainty of each step is analyzed and a total error is quantified.

A number of operation conditions are then evaluated with the methods described above. Each of those have been compared to a baseline point with stratified charge, no EGR and 90ºC intake air temperature. The results are presented in Chapter 8 and can be divided in three groups: Initially the differences of homogeneous and stratified combustion are studied as laid out in Chapter 8.1. The impact of intake air temperature on NO formation is assessed in Chapter 8.2, while the effect of EGR is investigated in Chapter 8.3. The results of all three experimental methods are extensively compared to each other, both on a single-cycle basis as well as averaged. Particularly, the correlation of the results obtained with each technique is examined. Additionally, thermodynamic analysis of cylinder pressure traces is presented.

The conclusions drawn from the results are presented in chapter 9. The combination of three experimental techniques enabled the validation of the results obtained with one technique against another, thus providing an inclusive insight in the NO formation process. Even though NO-LIF depends on the unknown local temperatures and equivalence ratios, it could be shown that meaningful results can be obtained with this technique. It is found that OH* correlates with NO-LIF but not with the cycle resolved engine out NO. Another focus of the study is on cyclic variability as averaged data alone proved insufficient in assessing the NO formation process. The thesis concludes with suggestions for future investigations, such as identifying the relative importance of the NO reducing mechanisms introduced by EGR such as oxygen dilution, thermal and chemical effects within this particular combustion system. Recommendations are made to enhance the accuracy of the NO-LIF measurements. A strategy to improve the correlation of OH and particularly engine out NO is outlined.

# 2 NO Formation and Destruction

Emissions of combustion engines contain three types of oxides of nitrogen:

- Nitric oxide (NO)
- Nitric dioxide ($NO_2$)
- Nitrous oxide ($N_2O$)

Nitric oxide is the most significant source of nitrogen oxide in most combustion processes. Spark ignited engines typically emit less than 2% of the total NOx in the form of nitric dioxide. For compression ignited engines the $NO_2$ mole fraction can be as much as 30% of the total oxides of nitrogen. [Heywood, 1988].

There are three major reaction mechanisms for NO formation in combustion [Glassman, 1996]:

- Oxidation of atmospheric nitrogen via the thermal mechanism
- Prompt NO mechanism
- Oxidation of nitrogen bound in fuel components

## 2.1 Thermal or Zeldovich NO Mechanism

Thermal NO is formed by the following reactions:

$$O + N_2 \rightleftharpoons NO + N \tag{2.1}$$

$$N + O_2 \rightleftharpoons NO + O \tag{2.2}$$

This mechanism was first postulated by [Zeldovich, 1946], and later amended by [Lavoie, Heywood et al., 1970] :

$$N + OH \rightleftharpoons NO + H \tag{2.3}$$

Reaction (2.1) requires a high activation energy due to the triple bond of the N2 molecule and thus high temperatures are required to achieve sufficient reaction rates, hence the name thermal NO. [Warnatz, Maas et al., 2001] This is the primary mechanism for nitric oxide formation in combustion engines. It is relatively slow compared to the combustion process, therefore NO formation depends more on burned gas (post flame) temperature

and equivalence ratio. This explains also, why nitric oxide concentrations are highest under slightly lean combustion conditions, where temperatures are high, and sufficient oxygen is available. With burned gas temperatures dropping during the expansion stroke reaction rates decrease rapidly. Below 2000K the NO concentration "freezes" if the burned gases cooling off sufficiently during the expansion stroke. [Heywood, 1988]

### 2.2 Prompt NO

Prompt NO, first described by [Fenimore, 1978] is formed in the flame front of fuel rich hydrocarbon flames via the CH radical. The latter is an intermediary species that combines with atmospheric nitrogen to form cyanide, which quickly reacts to nitric oxide. This reaction is much faster and the activation energy is about a third compared to the thermal mechanism. As a result prompt NO is formed already at temperatures of about 1000K.

$$CH + N_2 \rightarrow HCN + N \rightarrow ... \rightarrow NO \tag{2.4}$$

This mechanism is dominant in both fuel rich premixed combustion and diffusion flames where it accounts for up to 50% of the total NO production. [Bowman, 1992] .

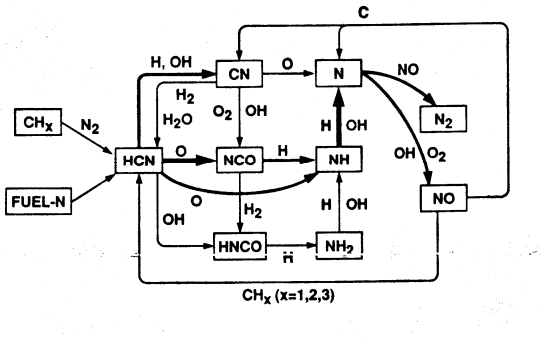


*Figure 2-1; Reaction path diagram illustrating the major steps in prompt NO formation, the conversion of fuel nitrogen, and reburning [Bowman, 1992]*

### 2.3 Conversion of fuel bound nitrogen to nitric oxide

Nitrogen chemically bound in fuel is also a source of nitric oxide. It is formed in similar fashion to the prompt NO mechanism (also see Figure 2-1) in the flame front via the formation of $NH_3$ (ammonia), CN and HCN (cyanide) [Bowman, 1992]. These conversion reactions are very rapid, on a similar order as the combustion reactions. Under

stoichiometric to lean conditions almost 100% of the fuel bound nitrogen is converted to NO. Lower yields were found under fuel rich mixtures. Lighter crude oil distillates such as gasoline contain less than 0.1% nitrogen compounds. [Heywood, 1988]

### 2.4 Reburn

Under fuel rich conditions NO can be recycled by reaction via small hydrocarbon radicals ($CH_x$) back into cyano compounds (CN, HCN), similar to the mechanism described in 2.2 and Figure 2-1. This reaction process is termed reburn. [Bowman, 1992]

### 2.5 Exhaust Gas Recirculation

A well known method to reduce engine out NO emissions is exhaust gas recirculation. The exhaust gas, which is composed mostly from water, CO2 and nitrogen acts as an inert gas that increases the heat capacity of the cylinder charge and consequently lowers the combustion temperature. The reduction in flame temperature and – speed and subsequently NO emissions is independent of the diluent gas as long as the heat capacity, which is the product of diluent mass flow rate and specific heat, is constant [Quader, 1971]. In throttled SI engines, EGR is introduced as additional charge to the intake air flow, consequently increasing the charge mass. In diesel engines, (or SIDI engines running stratified ) which are not throttled, EGR replaces a part of the air charge mass, thereby lowering the oxygen / fuel ratio as well as increasing the thermal capacity. [Ladommatos, Abdelhalim et al., 1997b] While the thermal effect is the main cause for NOx reduction in SI engines, in CI engines the reduction of oxygen availability increases mixing time and burn duration, ultimately resulting in lower flame temperatures as well. A minor contributor to the reduction of NO formation is the endothermic dissociation of water vapor and carbon monoxide. [Ladommatos, Abdelhalim et al., 1996a; Ladommatos, Abdelhalim et al., 1996b; Ladommatos, Abdelhalim et al., 1997a; Ladommatos, Abdelhalim et al., 1997b]

# 3 Gasoline direct injection

The idea to inject fuel directly into the cylinder was already developed in the 1930s for airplane power plants. Compared to the then available carburetors the direct fuel injection was so successful in improving mixture preparation, fuel consumption and improved performance through charge cooling that it became standard for Daimler Benz airplane engines. Soon it was adapted for racing engines and a mass produced sports car. However, this homogeneous charge injection system proved too complicated and expensive for everyday vehicles and was replaced with cheaper and simpler port fuel injection (PFI) systems [Scherenberg, 1961]. Research interest on gasoline direct injection combustion systems was renewed during the 1990s as a means to introduce a stratified charge into the cylinder and ultimately reduce fuel consumption. After Mitsubishi [Kume, Iwamoto et al., 1996] introduced a mass produced gasoline direct injection system [Cole, Poola et al., 1998] in 1997, almost every car manufacturer developed a stratified charge SIDI engine on its own.

## 3.1 Advantages and Disadvantages of SIDI engines

The SIDI engine offers a number of advantages compared to a PFI engine as summarized in [Zhao, Lai et al., 1999; Zhao, Harrington et al., 2002]:

- Improved fuel economy:
  - Reduced pumping loss
  - Less heat loss
  - Higher compression ratio
  - Improved fuel cut off during deceleration
  - Less acceleration enrichment required
- Improved drivability:
  - Transient response
  - Improved cold start
- Combustion stability:
  - High EGR tolerance

Of course there are also disadvantages of SIDI:

- Complicated control systems with multiple modes required
- Injector and spark plug fouling due to impingement
- Exhaust after treatment difficult
- Soot formation

*Table 3-1: Summary of contributions to the improvements of fuel economy of a SIDI versus a similar PFI engine*

| | **[Kume, Iwamoto et al., 1996]** | **[Alkidas and El Tahry, 2003]** |
|---|---|---|
| ***Reduced pumping loss*** | 15% | 10% |
| ***Reduced heat loss*** | 5% | 2% |
| ***Improved thermodynamic properties*** | 5% | 7.5% |
| ***Reduced dissociation*** | 2% | -- |
| ***Higher Compression ratio*** | 3% | 3% |
| ***Lower combustion efficiency*** | -- | - 4% |
| ***Higher friction (due to higher peak pressures)*** | -- | -4% |
| ***Total improvement vs. PFI*** | 30% | 15% |

The SIDI engine operates unthrottled and relies on the fueling rate for load control. This drastically reduces pumping loss as compared to a PFI engine. The stratified charge employed during part load reduces direct contact of the flame and the hot burned gases with the cylinder wall therefore reducing heat loss. The benefit of the charge cooling effect by injecting fuel directly into the cylinder is twofold: The knock tendency of the engine is reduced allowing for higher compression ratios. Particularly during high load operation with early injection the volumetric efficiency is increased resulting in higher power output.

The fuel film formation in the intake port is eliminated, thus improving response during acceleration reducing the necessity of cold start enrichment and response to load change.

However, film formation continues be a problem inside the cylinder and particularly on the piston, where it is a cause for hydrocarbon (HC) and particulate emission. [Drake, Fansler et al., 2003] Due to the inhomogeneous nature of the mixture forming process, both overmixed (too lean) and undermixed (too rich) regions are present. The former have been identified as the major source of HC, while the latter lead to the formation of smoke. The relatively high formation of $NO_x$ can also be attributed to richer areas of the combustion, where reaction temperatures are high. SIDI engines tolerate higher amounts of EGR compared to PFI engines, thus NO emission can be effectively lowered. [Kume, Iwamoto et al., 1996; Jackson, Stokes et al., 1997] Conventional three way catalysts cannot operate with such lean exhaust gas typically emitted from SIDI engines, so lean burn catalysts have been developed. The Iridium catalyst continuously reduces NOx with HC in lean burn phases with an efficiency of 30% to 50%. The NOx storage catalyst requires periodic rich burn operation to reduce the NO stored during lean operation to $N_2$. Its conversion efficiency is >90%, but the regeneration cycles increase fuel consumption.

However exhaust gas recirculation is still required to minimize regeneration cycles and the associated fuel efficiency penalty.[Krebs, Pott et al., 2002]

### 3.2 Combustion systems

The SIDI combustion systems can be classified by the interaction of internal air flow, fuel spray, and piston respectively cylinder wall. For wall controlled combustion systems fuel is injected on an in-cylinder surface, usually a well defined piston cavity. The fuel evaporates, forms a cloud and is transported via a supporting swirl [Alkidas, Lippert et al., 2002] or tumble [Solomon and Szekely, 2003] flow to the spark plug. This way the injection can be relatively early and more time for mixture preparation is available. Oftentimes the flow conditions have to be adjusted for different loads with swirl valves or tumble flaps [Fischer, Kettner et al., 2002]. Curved intake runners to introduce swirl can reduce the volumetric efficiency, so that at high loads sufficient air flow has to be provided with split or bulk flow ports. Air guided or flow controlled systems rely mostly on the charge motion to form the mixture and transport it to the spark plug. Fuel film formation and thus particle and soot production are reduced. The spray guided or jet controlled combustion system is based on the close proximity of injector and spark plug.

Here the fuel is transported solely by the impulse of the spray. A comparison of all three combustion systems can be found in [Ortmann, Arndt et al., 2001].

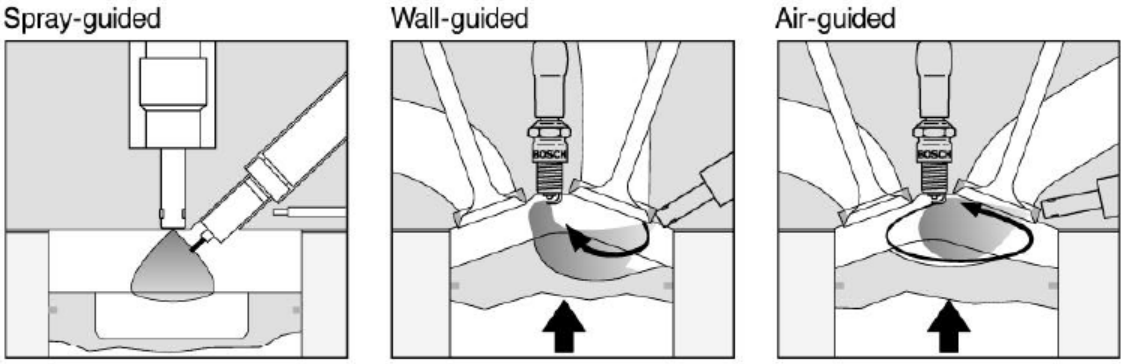


*Figure 3-1: Classification of SIDI combustion systems as spray guided or jet controlled, wall guided or -controlled, and air guided or flow controlled. [Preussner, Döring et al., 1998; Geiger, Grigo et al., 1999]*

### 3.3 Advantages of Spray Guided Combustion Systems

In contrast to wall-guided designs, spray-guided systems allow higher stratification over a wider range of loads. Reduced impingement of fuel on the piston results in less soot formation [Drake, Fansler et al., 2003; Honda, Kawamoto et al., 2004]. Overall, the piston shape is less critical. In fact, [Stan, Stanciu et al., 2004] demonstrated the feasibility of a spray-guided combustion concept in a small high-speed engine without the need of a supporting air movement generated by intake runners or a piston bowl. Spray-guided operation with pressure-swirl injectors is potentially affected by the strong susceptibility of the spray shape as a function of temperature and in-cylinder pressure [Schänzlin, 2003]. Since the fuel cloud has to be targeting the spark plug, a stable spray pattern is important for reliable operation of a spray-guided direct-injection engine. For this reason, the use of multi-hole injectors has become very popular. Spray patterns from this type of injector are less sensitive to changes in ambient pressure [Ortmann, Arndt et al., 2001] compared to pressure-swirl sprays.

### 3.4 Disadvantages of Spray Guided Combustion Systems

The spray guided combustion system has a few downsides compared to other SIDI systems as well. Mostly an extended spark plug has to be employed to reach towards the vicinity of the spray plume. Spray guided systems require exact timing of the injection and ignition, and the sequence of both events to assure proper mixture formation and high combustion stability. Therefore combustion phasing cannot necessarily be optimized from the thermodynamic point of view. The fuel spray either impinges the spark plug or passes in close vicinity which can lead to fouling. The requirement of rich mixture with equivalence ratios of 1.5 to 2 at the spark plug for optimum engine operation [Fansler, Drake et al., 2003] leads to rich pockets with subsequent soot formation, which at least partially oxidizes through mixing with hot oxygen rich exhaust gases. Rich burning of liquid fuel deposited on the spark plug contributes significantly to soot emission [Drake, Fansler et al., 2004].

### 3.5 Combustion system under Investigation

The combustion system studied in the following sections is defined by a number of features as shown in Figure 3-2:

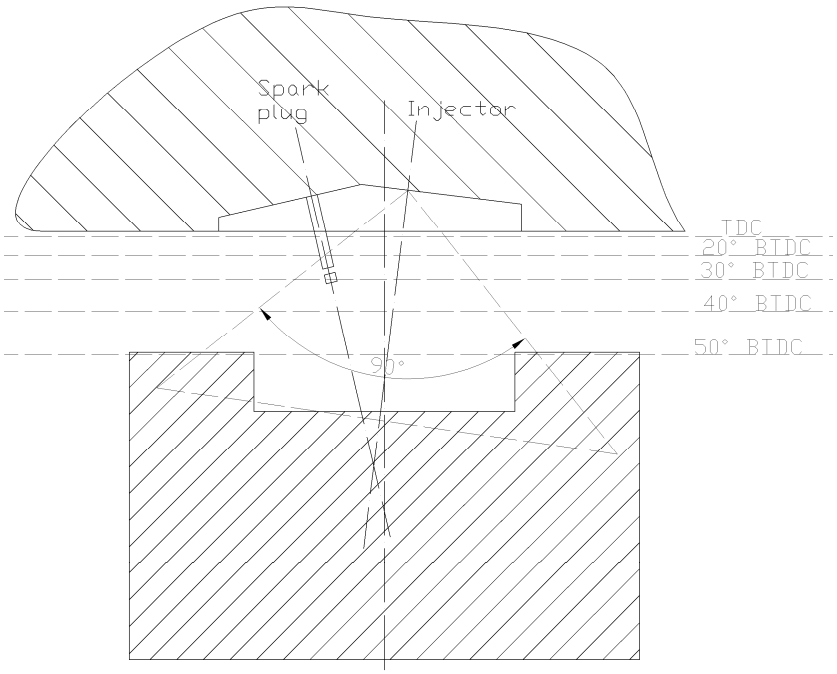


*Figure 3-2: Simplified cross section through the combustion chamber.*

The combustion chamber inside the head is shaped as a pent roof. Spark plug and multi-hole injector are centrally located in a narrowly spaced arrangement with the spark plug located between the exhaust valves. They are inclined towards each other. The spark plug is elongated such that it reaches in the curtain area of the ninety degree spray cone as symbolized by the dashed triangle in Figure 3-2. One of the spray jets is impacting the spark plug gap as shown in the series of spray images in Figure 3-3. The cylinder head is shaped such that a pronounced squish is produced in conjunction with the piston. The latter features a centrally located dish in the piston with a rectangular cross section. The dashed horizontal lines in Figure 3-2 illustrate the positions at a number of crank angles close to TDC.

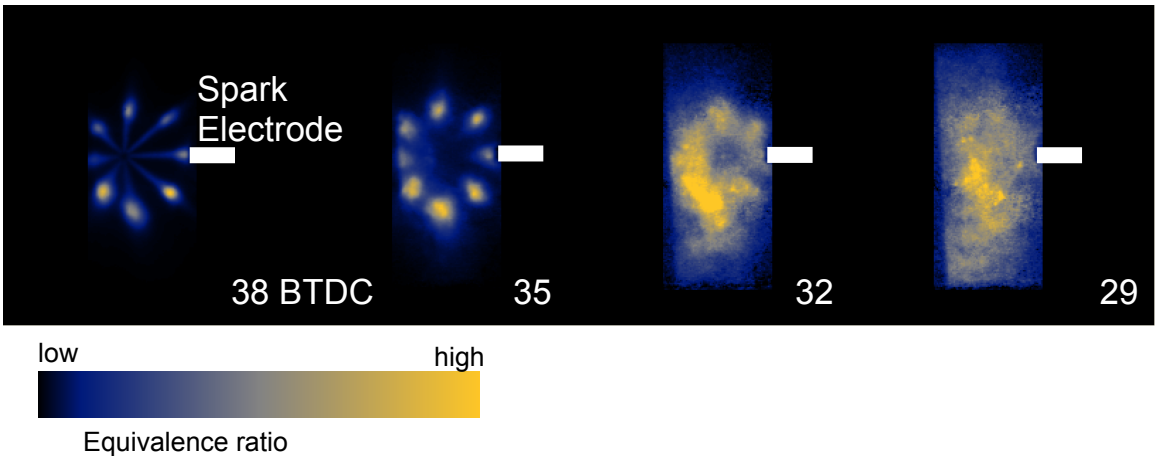


*Figure 3-3: An example of the spray evolution with one of the spray jets impacting the spark plug gap*

# 4 Fundamentals

This chapter briefly summarizes the basics of the experimental techniques applied in this thesis, such as imaging of chemiluminescence of the hydroxyl radical, and laser induced fluorescence spectroscopy of nitric oxide.

## 4.1 OH Chemiluminescence

Chemiluminescence light measurement is a convenient way to investigate technical combustion processes, because the light emission occurs naturally. In hydrocarbon combustion the most common chemiluminescence emitters are OH*, CH*, $C_2^*$, and $CO_2^*$. The emission of the electronically excited hydroxyl radical is relatively strong and thus this molecule is particularly well suited for optical diagnostics. In contrast to PLIF imaging, chemiluminescence imaging provides a two-dimensional representation of a three-dimensional intensity distribution. But even in SIDI engines under highly stratified operating conditions, imaging of the chemiluminescence of OH radicals ($OH^*$) provides a high level of detail about the combustion process [Stojkovic, Fansler et al., 2003; Stojkovic, Fansler et al., 2004].

The hydroxyl radical is an intermediate product occurring during the combustion of hydrocarbons via the reaction of molecular oxygen of the CH radical. Another reaction path is via formyl radicals (HCO) and oxygen atoms [Haber and Vandsburger, 2003]. The strength of OH* emission is dependent on the equivalence ratio and strongest for $\phi$ = 0.9 to 1. It also depends on flame strain rate and can be a reasonable good marker for heat release rate [Hardalupas and Orain, 2004]. However, the latter might not hold true under all combustion conditions as [Najm, Paul et al., 1998] suggested.

As the extended Zeldovich mechanism states, OH is one of the precursors of NO. OH chemiluminescence measurements might then be a simple way to predict local nitric oxide concentration.

### 4.2 Laser Induced Fluorescence

Laser induced fluorescence is the spontaneous emission of light by a molecule that has been excited into a state of higher potential energy by absorption of a photon produced by a laser. These energetic states are defined by quantum physics as discrete steps and are subdivided into electronic, vibrational, and rotational states.

$$E_{pot} = E_{el} + E_{vib} + E_{rot} \tag{4.1}$$

Planck's law states that, if an electron returns to a lower energetic state by emitting a photon the frequency of the emitted light is proportional to the difference of the higher and lower energetic state. The proportionality factor is *Planck's constant h*.

The energy spacing is such, that $\Delta E_{el} > \Delta E_{vib} > \Delta E_{rot}$ and the associated radiation is ultraviolet or visible, infrared or microwave respectively. One could think of the electronic states being subdivided into vibrational states, which are themselves subdivided into rotational states. Not all transitions from one state to another have the same probability to actually take place. These probabilities are described by the selection rules as imposed by quantum physics. Details can be found in [Banwell and McCash, 1994] or [Eckbreth, 1996].

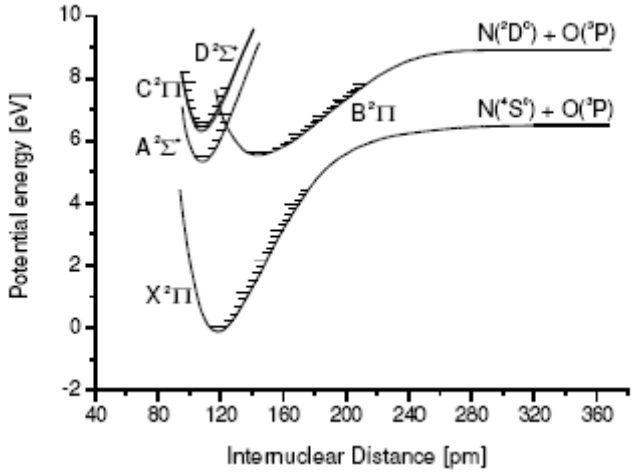


*Figure 4-1: A potential energy diagram for the NO molecule. [Gilmore, 1965]*

The energy levels of the NO molecule are illustrated in Figure 4-1. The electronic ground state is marked with X, while the higher states are marked with A, B, C, D in rising order.

The little horizontal lines attached to the potential energy curves describe the vibrational bands which are subdivided in rotational lines.

### 4.3 Mathematical Modeling of LIF

Mathematical modeling of the energy transfer processes has been simplified by a rate equation approach. In the simplest case a two level model is used as depicted in Figure 4-2. The rates for absorption and stimulated emission are $b_{12}$ and $b_{21}$. They are related to the Einstein $B$ coefficient through $b = \frac{BI_\nu}{c}$ with the speed of light c and the spectral irradiance $I_\nu$ [$Wcm^{-2}s^{-1}$] of the laser. $A_{21}$ is the spontaneous emission rate given by the Einstein $A$ coefficient, a molecule specific constant. The rate of predissociation $P$ and the rate of photo-ionization $W_{21}$ are included but negligible for our application. This is true for the induced emission rate $A_{21}$ as well. Collisional (electronic) quenching as described by quenching rate $Q_{21}$ is a relaxation processes without emission of radiation. It has a significant impact on LIF measurement of nitric oxide.

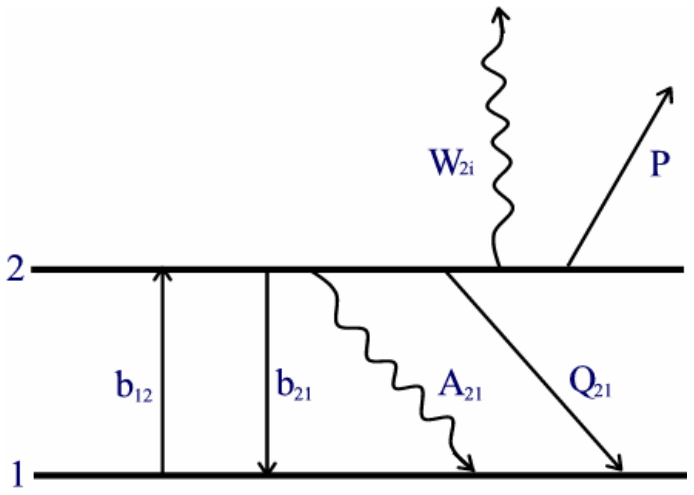


*Figure 4-2: Simple two level LIF model.*

The absolute number of molecules is the number of molecules in state 1 and in state 2. The total rates to and from each state is determined by summing up all rates mentioned above. We obtain then two differential equations describing the total rate of depletion of each state, where $N_1$ and $N_2$ are the number densities of molecules in each state.

$$\frac{dN_1}{dt} = -N_1 b_{12} + N_2(b_{21} + A_{21} + Q_{21}) \tag{4.2}$$

$$\frac{dN_2}{dt} = N_1 b_{12} - N_2(b_{21} + A_{21} + Q_{21} + W_{2i} + P) \tag{4.3}$$

A number of assumptions can now be made:

- Predissociation and photo ionization are negligible $P \approx 0$ and $W_{2i} \approx 0$
- The number of molecules is constant and the population of level 2 is negligible before the laser pulse: $N_2^0 = 0$ and $N_1 + N_2 = N_1^0$
- The laser pulse is long compared to all the other processes that the population of level 2 can be considered at steady state. This holds true for the pulse duration of the Excimer laser used during the course of this work.
- The spectral laser line shape is considerably wider than the probed absorption line.
- The spectral intensity that this laser can provide, particularly when spread over a relatively large volume, is much smaller than the saturation intensity. $I_v << I_{v\,sat}$

Using the aforementioned constraints and boundary conditions, the differential equations (4.2) and (4.3) can be solved with

$$N_2 = N_1^0 B_{12} I_v \frac{A_{21}}{A_{21} + Q_{21}}. \tag{4.4}$$

Considering now that only a part of the fluorescence is collected in the detector the fluorescence power is described as

$$P_{lif} = h\nu \frac{\Omega}{4\pi} \eta V B_{12} N_1^0 I_v \frac{A_{21}}{A_{21} + Q_{21}}. \tag{4.5}$$

The solid angle $\Omega$ and the detector efficiency $\eta$ are usually determined experimentally through a calibration. The detection volume $V$ is necessary to convert from number density $N_1^0$ to absolute number of molecules.

This model omits the fact that level 1 and 2 in reality are subdivided in a manifold of vibrational and rotational states. Under certain circumstances, such as fully equilibrated or fully frozen rotational level manifolds, this is acceptable. This is not necessarily the case for many experimental situations. The two level model is thus enhanced by two

additional levels, which account for rotational and vibrational energy transfer away from the directly laser coupled levels. In the case of the NO molecule, some simplification can be made though:

- Vibrational energy transfer in the ground state can be neglected.
- The quenching rate does not depend on excited state rotational levels resulting in a constant fluorescence yield.
- Fluorescence is detected over a relatively broad wavelength range, such that small changes due to energy transfer to neighboring rotational levels do not alter the level of recorded signal.

As a result, the two-level model can be sufficiently improved by adding a third ground level that is filled and depleted by rotational energy transfer processes only. So far the signal was related to the number of molecules in state 1. To be able to assess the total number of particles, the thermal population of the ground level as given by the Bolzmann fraction $f_b(T)$ must be known as well as the spectral overlap $\Gamma(P,T)$ of the laser with the absorption lines. Thus equation (4.5) becomes in the most general form:

$$I_{LIF} \approx N_0 I_\nu^0 \eta \underbrace{\sum_i f_{b,i} B_i \Gamma_i}_{Absorption} \underbrace{\sum_i \frac{A_{2j}}{\sum_k A_{2k} + Q}}_{Emission} \tag{4.6}$$

Indices:

i – Number of lines excited, particularly due to pressure broadening. In the simplest case i = 1.

j,k – Either 1 or 3 depending on to which ground level the transition takes place.

$I_{LIF}$ – spectral power density [$Wcm^{-2}s^{-1}$] is proportional to $P$

For a more detailed description of fluorescence modeling and underlying quantum physics , refer to [Eckbreth, 1996; Daily, 1997; Bessler, Schulz, Sick et al., 2003] which the preceding chapter has been a summary of.

## 4.4 Detecting Nitric Oxide

PLIF imaging of NO for engine applications has been developed and applied over the last decade. A range of different strategies is described in the literature to overcome inherent

difficulties with quantitative interpretation of the measured PLIF signals. Major problems are interference with background signal, particularly LIF signals from $O_2$ and polycyclic aromatic hydrocarbons (PAH), and absorption of laser and signal light by combustion products. But also the dependence of the LIF signals on pressure, temperature, and mixture composition makes quantitative NO imaging diagnostics in engines very challenging.

### 4.4.1 Background Signal

Fluorescence from species other than nitric oxide contributes to the measured signal in varying degrees depending on pressure, temperature and chosen excitation-detection strategy. Contribution from narrowband interference such as from hot oxygen can be minimized by choosing an appropriate excitation wavelength [Hildenbrand, Schulz et al., 2001].

Broadband emissions from carbon dioxide have been measured with excitations of 215 to 255nm. The signal has a maximum around 290nm and gently slopes off towards shorter wavelengths. It scales linearly with pressure and can be found over a wide range of equivalence ratios. In very rich flames the formation of polycyclic aromatic hydrocarbons becomes relevant. These molecules cause broadband interference as well [Bessler, Schulz et al., 2003].

### 4.4.2 Line (Pressure) broadening and shifting

The spectra of molecules are changed with increasing pressure through collisional broadening and shifting. In respect to spectroscopy of the NO molecule, two different effects have to be considered.

The wavelength of the laser stays constant while the absorption wavelength shifts with increasing pressure thus reducing the excitation efficiency. In experiments with controlled environments such as high pressure burners, this can easily remedied by tuning the laser to a more appropriate wavelength. When conditions change rapidly, such as in combustion engines, retuning the laser is hardly possible. In this case the excitation wavelength has to be a compromise and the loss of signal has to be accounted for in the data evaluation.

The NO emission spectra overlap with signals from other species, particularly oxygen. The emission of the latter is less dependent of pressure [Sick, Decker et al., 1996], which results in a pressure dependent overlap of NO and $O_2$ spectra. The NO signal is reduced with increasing pressure thus the relative height of $O_2$ background increases.

### 4.4.3 Signal / Laser absorption

Laser and signal light are also absorbed by combustion species other than NO, particularly by $H_2O$ and $CO_2$. The transmission $T_\lambda$ through hot exhaust gases depends besides on the absorbing species on path length $l$, and indirectly on pressure via the number density $N$.

$$T_\lambda = e^{-\sigma(T,\lambda)Nl} \tag{4.7}$$

The absorption cross section $\sigma$ is a function of temperature $T$ and the absorbed laser wavelength $\lambda$ [Schulz , Gronki et al., 2002; Schulz , Jeffries et al., 2002; Schulz, Koch et al., 2002].

### 4.4.4 Quenching

Quenching depends first of all on the species and its quenching cross section which is a function of temperature. The degree of quenching depends further on the number density and therefore scales linearly with pressure. It also depends on temperature in a more complicated relation, but scales with 1/T in first approximation. The strongest quenching molecules are CO, $H_2O$, and $CO_2$. The latter two are the most important due to their high concentration in combustion situations.

### 4.4.5 Excitation detection schemes

The vibrational structure of the ultraviolet NO transitions as shown in Figure 4-3 allows the efficient excitation with a variety of laser sources as illustrated with a few examples below. These laser sources provide pulse energies that are high enough to illuminate extended areas inside of an engine for imaging diagnostics. Figure 4-4 illustrates which detection band passes can be used with excitation around 225nm, 235nm or 248nm.

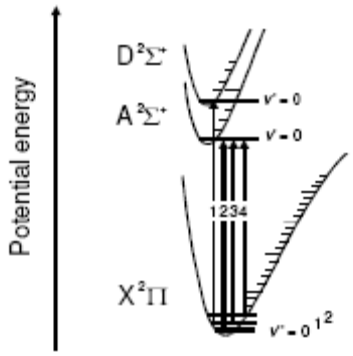


*Figure 4-3: Potential energy diagram of the NO X, A and D states. The arrows indicate different NO-LIF excitation strategies: 1. D–X(0,0) around 193 nm, 2. A–X(0,0) around 225 nm, 3. A–X(0,1)around 236 nm, 4. A–X(0,2) around 247 nm.[Bessler, 2003]*

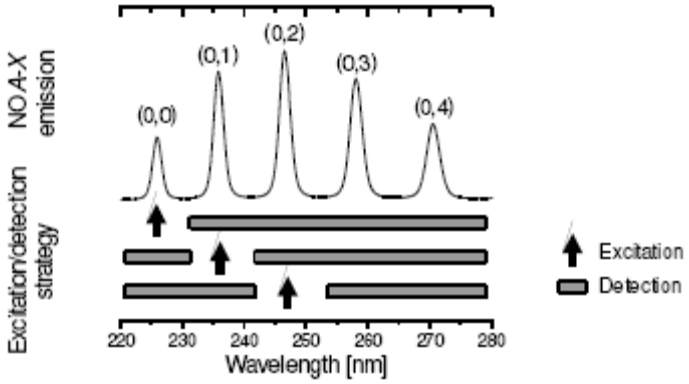


*Figure 4-4: Different options for NO-LIF detection with excitation in the A–X band. Excitation is possible within the A–X(0,0), (0,1) and (0,2) bands, while detection is possible in any bands red- or blue shifted relative to the excitation wavelength. [Bessler, 2003]*

Stoffels used a tunable ArF Excimer laser to excite the D-X (0,1) band at 193nm in a Diesel engine with commercial fuel for qualitative NO measurements. The limitation of this method is the high absorption of the laser beam by the fuel and combustion products [Stoffels, Boom et al., 1999]. A-X (0,0) excitation with light from an optical parametric oscillator (OPO) was used for measurements in a Diesel engine operated with low-sooting fuel to minimize laser beam attenuation [Dec and Canaan, 1998]. Previously, the first attempt on quantitative in-cylinder NO measurements in an SI engine using excitation in the same band was reported by [Bräumer, Sick et al., 1995]. They used a tunable KrF excimer laser and anti-Stokes Raman-shifting to produce laser light near 225nm. [Jamette, V.Ricordeau et al., 2001] also employed an OPO system but excited

within the A-X (0,1) band near 235nm to study NO formation in a gasoline direct-injection engine. Excitation of NO in the A-X (0,2) band, proposed by [Schulz, Yip et al., 1995], has some advantages compared to the aforementioned excitation strategies. The $O_{12}$ bandhead within this band corresponds to a minimum of the $O_2$ B-X transition. Blue shifted detection was shown to allow superior interference suppression of PAH and $CO_2$ LIF [Hildenbrand, Schulz et al., 1999]. Advantages and disadvantages of different excitation/detection strategies have been discussed extensively in some recent publications[Bessler, Schulz et al., 2002; Bessler, Schulz, Lee et al., 2003a; Bessler, Schulz, Lee et al., 2003b].

Common to all the listed NO-LIF excitation/detection approaches is that the signal strength is a function of temperature, pressure, and gas composition. Therefore, a quantitative analysis of LIF signals that links measured signal strength to number densities or mole fractions, must correct for the effects of these parameters, like for fluorescence quenching. In imaging experiments, these corrections work best for conditions with little spatial variation of temperature, pressure, and gas composition. Such conditions can be found for spark ignition gasoline engines with traditional port fuel-injection or premixed strategies [Hildenbrand, Schulz et al., 1998; Josefsson, Magnusson et al., 1998; Schulz , Wolfrum et al., 1998]. However, quenching corrections for non-premixed combustion conditions can substantially vary in space [Sick, Hildenbrand et al., 1998; Driscoll, Sick et al., 2002]. Unless the local mixture composition is known, spatially constant quenching corrections applied to the raw images will not fully correct for the impact of fluorescence quenching. The same arguments hold for the influence of temperature on signal strength. With the appropriate choice of excitation wavelength, it will, however, still be possible to obtain results that are within uncertainty limits that for example allow a meaningful discussion of differences between operating conditions of an engine. Using such strategies, NO PLIF studies were successfully performed for a variety of stratified conditions in Diesel and SI applications.

# 5 Experimental Setup

This chapter describes the installations necessary to conduct optical experiments. First of all the engine should have as much optical access as possible, while maintaining realistic performance. All necessary equipment has to be located such, that there is room to arrange optics, cameras and equipment. The engine itself should be well balanced to avoid interference with the imaging. To further ensure realistic performance and short operation, oil and water need to be temperature-conditioned. Ideally, this would be the case for intake air temperature as well as humidity. Further, a low and a high speed data acquisition system should be installed for thermodynamic and combustion analysis as well as engine surveillance. A simple, easy to clean fuel system had to be designed as well as a skip fire controller to ensure thermal stability.

## 5.1 Optical Engine

The engine is equipped with a four valve cylinder head with dual overhead cams. Each intake valve has its own port, one of which can be switched off to introduce a strong swirl. Injector and spark plug are in close arrangement. Technical data are summarized in Table 5-1.

*Table 5-1: Summary of the technical data of the cylinder head*

| | |
|---|---|
| Design | 4 Valves DOHC |
| Combustion Chamber | Pent Roof w/ End windows |
| IVO/ IVC (Primary / Secondary) | 357° bTDCF / (140° bTDCF / 129° bTDCF) |
| Lift (Primary / Secondary) | 10.3mm / 9.2 mm |
| EVO / EVC | 137° aTDCF / 373° aTDCF |
| Lift | 10.3 mm |
| Spark Plug length | 12 mm |
| Swirl Number (Low / High) | 0.8 / 5.5 |

The engine is based on an FEV crankcase, which is fully balanced. This is achieved by two counterweights that oscillate parallel to the piston. They are driven by eccentric disks ground on the crankshaft with 180º offset relative to the crank. This way both first and

higher order oscillating forces are eliminated. The simplicity of this setup is superior to the balancing with eccentric shafts. In the latter case two shafts for each order are required.

*Table 5-2: Technical data of the Engine*

| | |
|---|---|
| General | Fully Balanced Single Cylinder 4-Stroke |
| Connecting Rod | 159.2 mm |
| Bore | 86 mm |
| Stroke | 86 mm |
| Cylinder liner | Fused Silica |
| Compression Ratio | 9.0 |

### 5.1.1 Optical Access

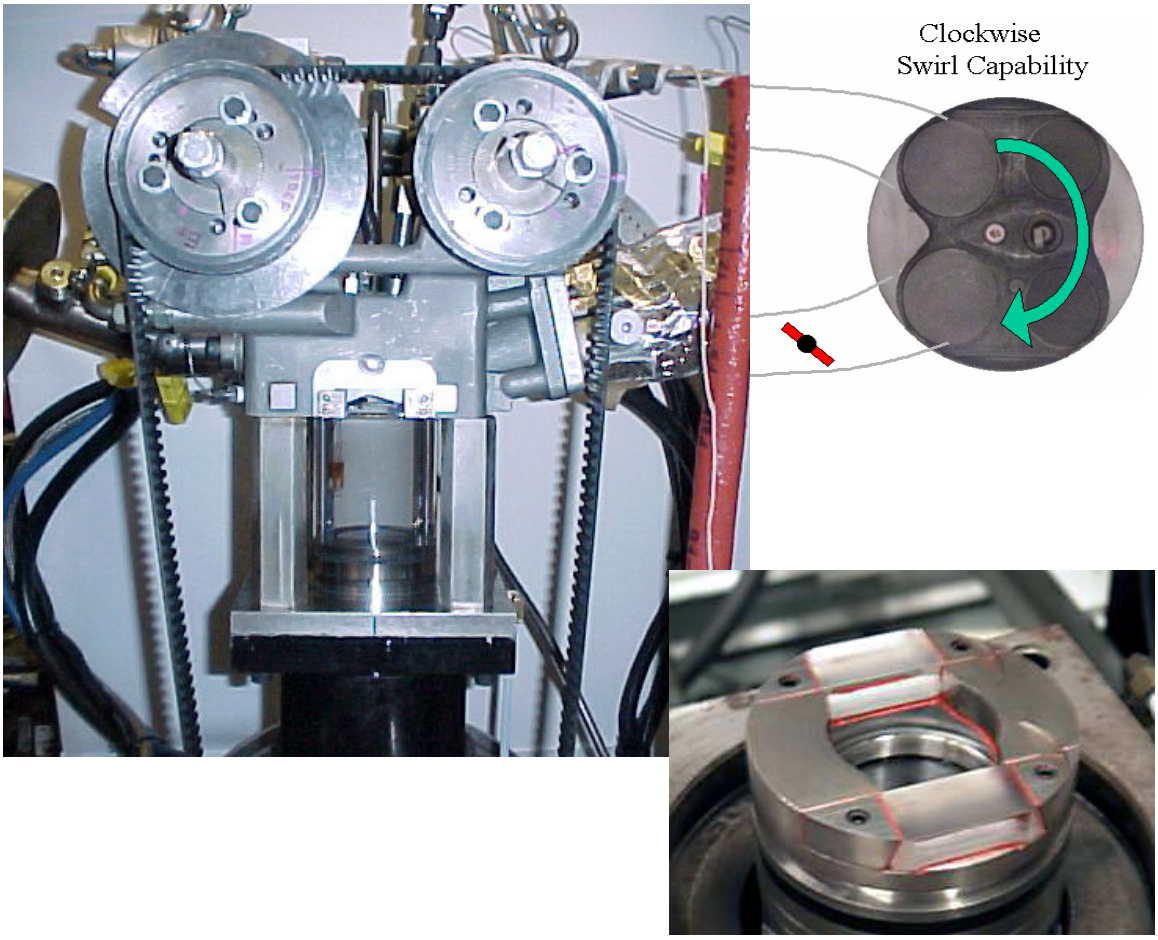


*Figure 5-1: The image on the left shows the quartz liner and the head windows. The picture on the lower right displays the dished piston while the image on the upper right depicts how the intake system introduces swirl into the cylinder.*

The engine grants optical access to the combustion chamber through a full quartz cylinder liner, two little windows in the pent roof of the cylinder head and a quartz plate in the piston crown. An extended, so called "Bowditch"- piston named after its inventor [Bowditch, 1961] allows the view towards the cylinder head via a mirror tilted at 45º. This is an essential part of the engine array since most laser based diagnostics require optical access in two perpendicular axes. The piston crown can be exchanged to run a flat piston or different bowl shapes.

### 5.1.2 Piston and bowl shape

The piston features a bowl with a simple rectangular cross section. The bowl is centered in the piston and is 11mm deep and 44mm in diameter. End windows have been added to facilitate measurements inside the piston bowl. The bowl had to be compromised slightly to allow for these windows to be flat. (see Figure 5-2) This minimizes light scattering when the laser beam penetrates the bowl. The piston is made from INVAR, a low expansion alloy. The heat expansion of the windows is still about ten times lower. The clamps holding the end windows and a spacer beneath the crown window help maintain a positive clamping force. Additionally the windows are sealed with GRAFOIL, which is extremely heat resistant and within limits elastic to take up any slack through thermal expansion. Details on the gasket thickness calculation can be found in [Fissenewert, 1999]

*Table 5-3: Thermal properties of materials used for the piston (Aluminum provided for comparison only)*

| ***Material*** | | ***Reference*** | ***Coefficient of expansion*** | | | |
|---|---|---|---|---|---|---|
| | | | 100 | 200 | 300 | T [C] |
| Steel: | SAE 1020 annealed | ASM Handbook Vol. 1 [N.N., 1999a] | 11.7 | 12.1 | 12.8 | $\gamma$ [1/C*10$^{-6}$] |
| Al | pure Al | ASM handbook Vol. 2 [N.N., 1999b] | 23.6 | 24.5 | 25.5 | $\gamma$ [1/C*10$^{-6}$] |
| AL | 6061 | ASM handbook Vol. 2 [N.N., 1999b] | 23.6 | - | - | $\gamma$ [1/C*10$^{-6}$] |
| fused silica | | Esco Products [N.N., 2003b] | - | - | 0.59 | $\gamma$ [1/C*10$^{-6}$] |
| INVAR 36 | | Ed Fagan [N.N., 2003a] | 1.18 | 1.72 | 4.92 | $\gamma$ [1/C*10$^{-6}$] |

As an added benefit of machining the piston from INVAR, the crown window gasket can be made from fairly thin material (~ 1 mm). It is also cut slightly larger on the inner diameter leaving a groove app 0.5 to 1 mm deep. The protection of the gasket material with silicone is now unnecessary. The gap acts as a flame arrestor.

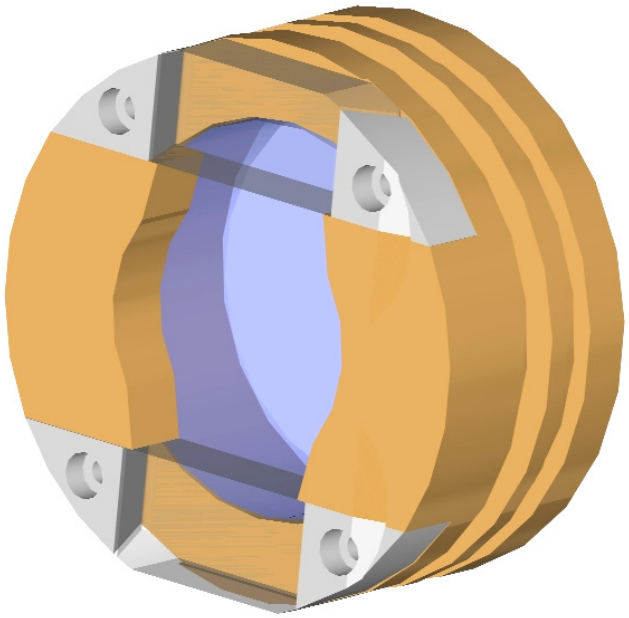

*Figure 5-2: Dished piston with crown and end windows*

The piston is running completely un-lubricated on carbon rings. Both the compression ring and the rider ring consist of two segments. The top ring acts as a compression ring made from St. Mary carbon grade 75, whose two segments are spring loaded. Here the end gap dimension has to be closely controlled to ensure sufficient sealing on one hand while accommodate thermal expansion on the other hand. A too small gap was found to cause the hot ring to bind and subsequently break during operation. The rider ring is made from a high strength antimony doped carbon. Due to its brittleness the axial clearance in the groove was found to be critical of the susceptibility of the ring to breaking. Too high of an axial clearance (~0.05 to 0.07 mm) introduces oscillations of the ring in the groove that are even visible in the cylinder pressure trace. This is particular true for sudden load change, which caused the ring to break. A slip fit of no more than 0.02 to 0.04mm clearance remedied that problem entirely.

### 5.1.3 Support Systems

The engine is equipped with a dry sump lubrication system. Both oil and water circuits are equipped with heaters and coolers to condition the engine to a desired temperature. The crankcase is evacuated by a vacuum pump to minimize the risk of oil leaks. Engine oil fluoresces and absorbs over a wide wavelength range so that even minimal oil leaks can cause substantial errors in optical measurements.

The test cell is equipped with a low inertia hydrostatic dynamometer made by Electromechanical Associates. A compact hydraulic motor (~8"by 8" by 12") is fitted to the engine crankshaft, while the main unit can be located elsewhere. The latter consists of an electrically driven pump to motor the engine and a controller operated valve for firing operation. In the latter case the hydraulic motor acts as a pump and the valve applies the brake torque by restricting the flow. This unique setup allows access to the engine on all four sides, and a smooth transition from motoring to firing. The main unit also contains a radiator to control the temperature of the hydraulic oil and the oil reservoir.

### 5.1.4 Injection System

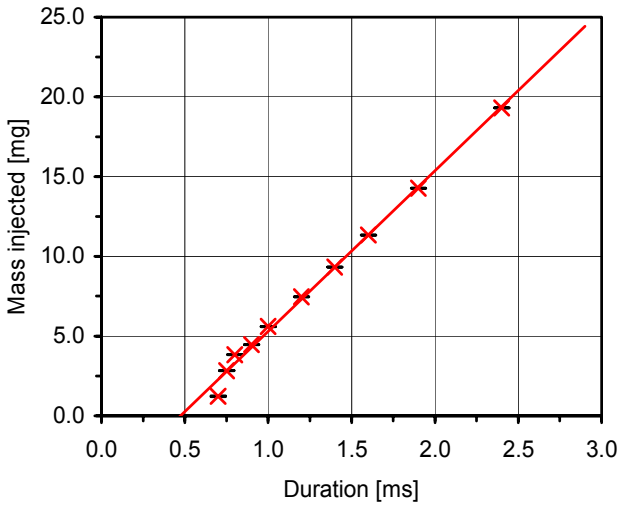


*Figure 5-3: Injector fuel mass flow calibration versus electronic trigger signal duration. Courtesy Scott Parish, General Motors*

A simple high pressure fuel system consisting of a nitrogen driven piston type hydraulic accumulator was designed. This system was deliberately kept very simple for ease of

flushing or cleaning. This is essential when different fluorescence tracers are used. For the same reason a fuel flow meter was not implemented. Instead the fuel metering was determined by a calibration of the injector against a piston type positive displacement meter manufactured by MAX in a test rig specifically for spray experiments. During this calibration fuel was injected into atmospheric pressure. During engine operation depending on injection timing the ambient pressures can be substantially elevated. The resulting metering error for pressures encountered at the injection timing used was estimated to be less than 3%. This is on the order of the uncertainty of the injector calibration. [Parish, 2003]

## 5.2 Instrumentation

A schematic overview of the high speed and the low speed data acquisition and engine control system as well as the imaging system is shown in Figure 5-4.

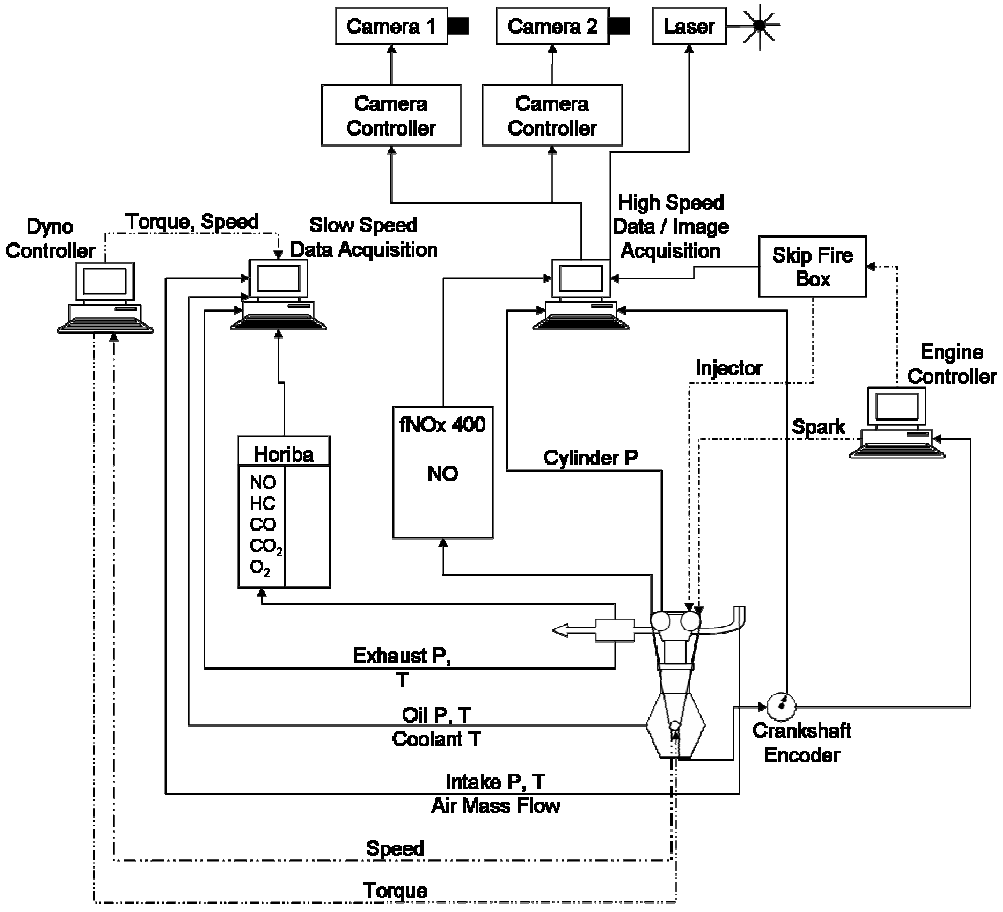


*Figure 5-4: Overview of engine instrumentation and control system.*

### 5.2.1 Air metering system

The correct measurement of the air mass flow into a single cylinder engine is challenging due to the pulsating nature of the flow. Pulsations have been reduced by adding a plenum with a volume of 25 l to the intake system. A volume of 50 times the displacement has been shown to effectively reduce the pulsation of the intake air flow [Taylor, 1985]. An intake runner with about 3" diameter further reduces the pulsation amplitude. Columnar vibration of the intake air is not only potentially detrimental on the flow measurement, but could also impact the engine performance. Advantages and disadvantages of different measurement methods are discussed in [Polak, Pande et al., 1999b; Polak, Pande et al., 1999a]. A popular flow measurement device for use with combustion engines is the laminar flow element due to its large measurement range of up to 1:100 and its relatively small sensitivity to pulsations [Millar, Gilllig et al., 1961]. It can thus be used for the whole range of flow rates encountered in engine testing. However it requires a very accurate pressure transducer, since the pressure differential over the laminar flow element is very small for low flow rates. In addition, upstream pressure and temperature as well as relative humidity have to be measured. Also, careful design of the connecting tubing is required to avoid the introduction of turbulence otherwise errors of up to 100% can occur [Stone, 1989]. If strong pulsations or backflow occur, it might be required to measure the differential pressure with crank angle resolution and calculate a root mean square in order to avoid aliasing effects [Martz, 2000].

An air flow measurement method completely unaffected by pulsating flow is the critical orifice meter. It makes use of the fact that the flow velocity through an orifice is limited to sonic speed. Once sonic speed is reached and the flow becomes choked, the mass flow is only dependent on pressure $P_0$ and temperature $T_0$ upstream of the orifice, since any pressure change downstream can only propagate with sonic speed as well. The critical pressure ratio $P_1/P_0 \approx 0.528$ for air can be used to monitor the presence of critical flow. The mass flow rate of air through an orifice is given by $\dot{m} = \frac{P_0 A C^* C_D}{\sqrt{RT_0}}$. The throat area is described by $A$; $R$ is the ideal gas constant. The critical flow function $C^*$ is a thermodynamic state variable depending on pressure and temperature at the throat. $C_d$ is

the discharge coefficient and corrects for deviation from the one dimensional, isentropic flow theory. For a constant temperature the mass flow $\dot{m}$ becomes a linear function of pressure, whose proportionality factor can be determined by calibration to a primary flow standard [Arnberg, 1962; Caron and Kegel, 1996; Jones and Seidel, 1997; Schulz , Jeffries et al., 2002].

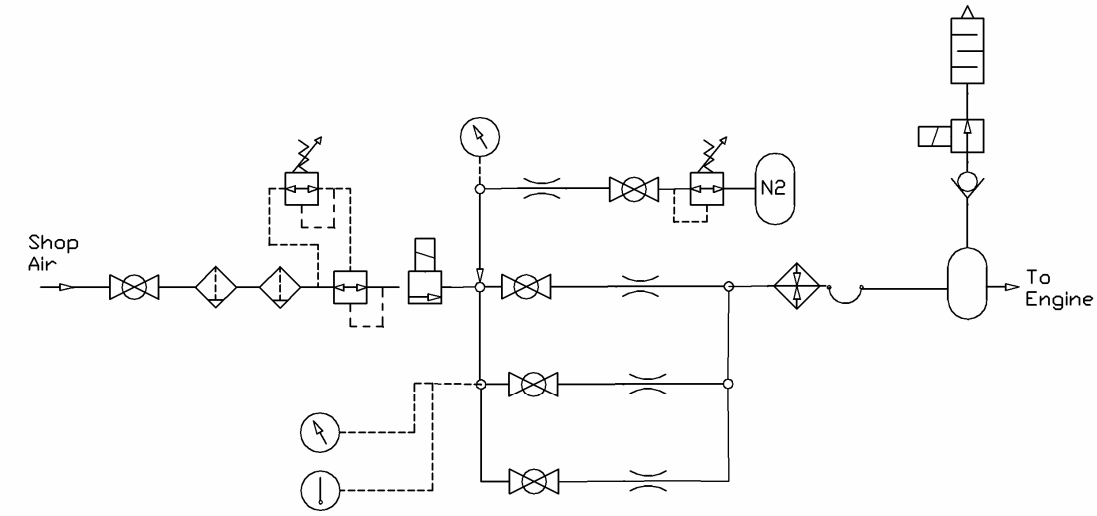


*Figure 5-5: The layout of the air flow measurement system based on critical orifices.*

The critical flow system as shown in Figure 5-5 is fed by the shop air system of the laboratory which supplies a pressure of approximately 90psi. Water is removed by a cooling unit and self draining filters. The remaining relative humidity is approximately 10%, which results in a negligible error on the discharge coefficient [Britton, 1998]. As an added benefit, the supply air temperature is fairly constant (22±2ºC). The line pressure upstream of the critical orifices is remotely controlled with a Nullmatic 42 precision pressure regulator. Supply pressure can be shut off with a solenoid valve. The required flow range is adjusted by selecting one of the three critical orifices with diameters of 0.125", 0.081", and 0.052". They are supplied with pressure by manual ball valves. Upstream pressure is measured with a Druck PTX1240 pressure transducer. Measurement of upstream temperature is conducted with a type K thermocouple. Diluents can be added to the intake air via an additional critical orifice from a gas bottle with a pressure regulator. The air flow enters the intake plenum via a heater that conditions it to a desired temperature. If an absolute pressure higher than approximately

1100 mbar builds up in the plenum a check valve blows off air. In case the engine is supposed to be supercharged, the check valve can be overridden with a solenoid valve.

### 5.2.2 Slow Speed DAQ

The slow speed data acquisition system consists of a PC equipped with a 64 channel analog digital card operating in differential mode. The readout software is programmed in LABVIEW for maximum flexibility. The time resolution is approximately 2Hz, while 10 points each are averaged and recorded to disk.

*Table 5-4: Pressures and temperatures recorded with the slow speed data acquisition.*

| | |
|---|---|
| Pressures | Intake |
| | Exhaust |
| | Critical orifice (for air flow measurements) |
| | Ambient |
| | Oil |
| Temperature | Intake |
| | Exhaust |
| | Coolant into Engine |
| | Coolant out |
| | Oil into Engine |
| | Oil out |
| | Quartz cylinder liner |
| | Air temperature (for air flow measurement) |
| Dynamometer | Torque |
| | Engine speed |
| Emissions | NO |
| | HC |
| | $O_2$ |
| | CO |
| | CO2 |

### 5.2.3 High Speed Data Acquisition system

A high speed data aquisiton system AVL Indiwin 3.1 was used to record signals with crank angle resolution, such as cylinder pressure and the signal from the fast chemiluminescence detector fNOx 400 by Cambustion.

Cylinder pressure was recorded with a piezoelectric pressure transducer 6125 manufactured by Kistler equipped with a flame arrestor to minimize thermal shock. [Rosseel, Sierens et al., 1999] This could be a problem particularly for skip fire operation. The transducer with its amplifier was calibrated with a RUSKA dead weight tester on a regular basis. Initially a two point calibration was done to determine the slope of the relation of amplifier voltage output and pressure. Therefore a pressure of approximately 80% of the maximum pressure in operation is applied. The transducer is pressure relieved and the difference in voltage output between loaded and unloaded recorded. Then in a similar fashion various pressures are recorded to determine repeatability and linearity. The transducer shows an error of 0.9% on average mostly due to deviations at the lower end of the measurement range and a repeatability error of 0.26%

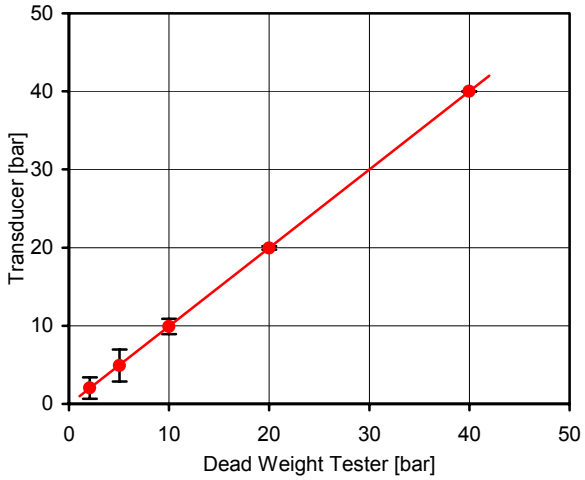


*Figure 5-6: The Kistler 6125 pressure transducer shows excellent linearity and accuracy.*

### 5.2.4 Engine Set Point Controller and Skip fire box

The Engine is controlled with a proprietary General Motors steady state engine set point controller with 12 channels. Four channels are designated to trigger ignition drivers, while up to eight injector drivers or any other device can be controlled. Dwell or injection time can be controlled in 0.001ms increments while injection respectively ignition timing can be adjusted from 360 BTDC to 360 ATDC in up to 0.1º steps depending on the resolution on the crank angle encoder.

To enable skip firing capability, a circuit basically consisting of a counter chip was developed that would interrupt up to three trigger signals for up to sixteen cycles.

### 5.2.5 Emissions analysis

A conventional emissions bench made by Horiba was available for steady state measurements when operating the engine continuously fired. It has the capability to measure HC, $NO/NO_2$, $O_2$, CO (two channels), and $CO_2$. Exhaust gas was measured on a dry basis. The $NO_2$ to NO converter can be switched off. Prior to experiments a two point calibration was performed by flushing the device with nitrogen as a zero gas and then flushing with a gas of the appropriate concentration of the species to be measured.

For cycle resolved nitric oxide emissions measurements a fast chemiluminescence detector (Cambustion fNOx 400) was available. It consists of a compact sampling head that can be mounted in close proximity to the measurement object while the main unit can be placed up to 6m away. The sampling head consists of a reaction chamber, a pre-chamber to dampen out pulsations and a 200mm long sampling line with an attachment to deliver calibration gases for in situ calibration.

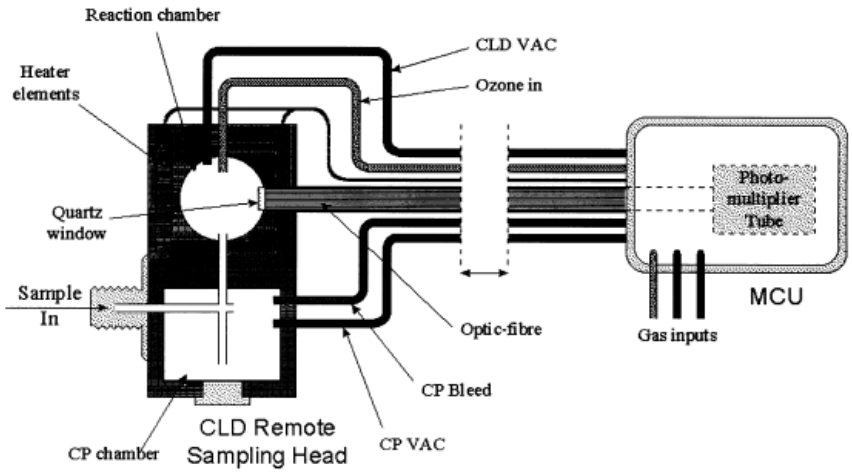


*Figure 5-7: Schematics of the fast NO detection system.[Peckham, Hands et al., 1998a]*

When comparing the readings of this instrument to a conventional $NO_x$ analyzer, it has to be kept in mind that this arrangement only measures NO. But this holds true for the NO-LIF measurements as well. Also in a SI engine no more than 5% $NO_2$ can be expected [Heywood, 1988]. The device measures on a wet basis, while emissions are mostly reported on a dry basis. The chemiluminescence is quenched by water vapor at a rate of 0.7% per 1% of water vapor. Additionally $CO_2$ quenches with 0.3% per 1% concentration.

### 5.3 Optical setup and Laser Diagnostics

Excitation of NO within the A-X(0,2) band was achieved with a tunable KrF excimer laser (Lambda Physik EMG 150 TMSC) near 247.95 nm. This laser was operated with single-pass amplification only to ensure proper locking at the short wavelength end of its tuning range. The wavelength-selecting grating was tuned with a stepper motor unit that was controlled via the camera and image processing software (LaVision DaVis 6.2). Excitation scans in an acetylene torch flame, showing NO and OH transitions at atmospheric pressure, were used to calibrate the laser wavelength and in conjunction with spectral simulations using LIFSIM (www.lifsim.com) the stepper motor settings for on- and off-resonant (with NO) excitation were selected to be 247.94 nm and 248.08 nm, respectively. As the rectangular laser beam had to travel for a distance of approximately 10 m from the laser to the engine setup, a spherical lens with f = 5 m was placed 0.5 m after the laser exit to re-collimate the beam before using a cylindrical lens (f=1m) as shown in Figure 5-8 and rectangular apertures to shape a light sheet with a cross section of 40 mm x 0.5 mm (up to 0.8 mm). For typical pulse energies of 40-60 mJ the energy density was calculated to be approximately 0.25 J/cm$^2$. After the aperture, a quartz wedge placed in the beam split off a small fraction of the beam energy that was directed onto a scattering glass and measured with a photodiode to track the pulse energy of each laser pulse. The light sheet intersected the cylinder at about 2.5 mm below the firedeck such that it passed through the spark plug gap.

A second photodiode was placed on the opposite side of the engine for measurements of the laser pulse energy once the beam had passed through the engine. This allowed measurements of beam attenuation due to combustion products as well as beam attenuation due to additional quartz windows in the piston crown. This was important for crank angles between -16 and +16 CAD ATDC. LIF signals were imaged onto an intensified CCD camera (LaVision FlameStar IIF) using a UV objective (Halle, f = 100 mm) via a UV-enhanced aluminum mirror that was mounted in the Bowditch piston of the engine. The position of the OH and NO-LIF images as seen through the piston crown are displayed in Figure 5-9. Signals were spectrally filtered to a) isolate NO A-X (0,1 and 0,0) fluorescence signals from $O_2$, OH and potential other fluorescence and b) to suppress any resonant scattering. A set of four narrowband reflective filters coated for best

performance in the range from 225-235 nm and a narrowband reflective filter for 248 nm were used for this purpose.

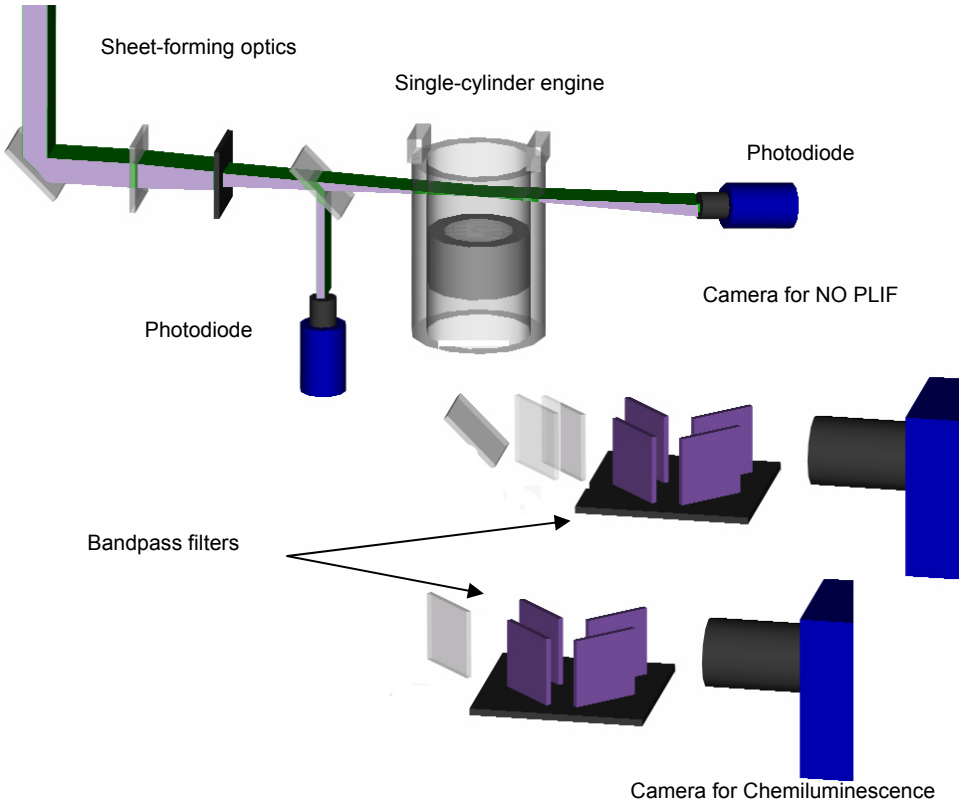


*Figure 5-8: Schematic illustration of LIF imaging setup. UV-chemiluminescence was recorded simultaneously by placing a dichroic beam splitter into the signal path before the 248nm bandpass filter. A similar four-way reflective filter was then used to filter out chemiluminescence around 310nm.*

Since the purpose of the present study was to combine optical imaging and traditional engine emission and thermodynamic analysis, we recorded pressure data and fast-NO emission data (described below) with crank angle resolution for each cycle were PLIF images of NO were recorded. The analysis and processing of these data was greatly facilitated by an analog-digital converter unit (LaVision) that recorded the pressure, fast-NO signal, laser energy, amongst other data with crank angle resolution and stored it along with the PLIF images in a single file that then was processed simultaneously for NO images and thermodynamic data on a per-cycle basis.

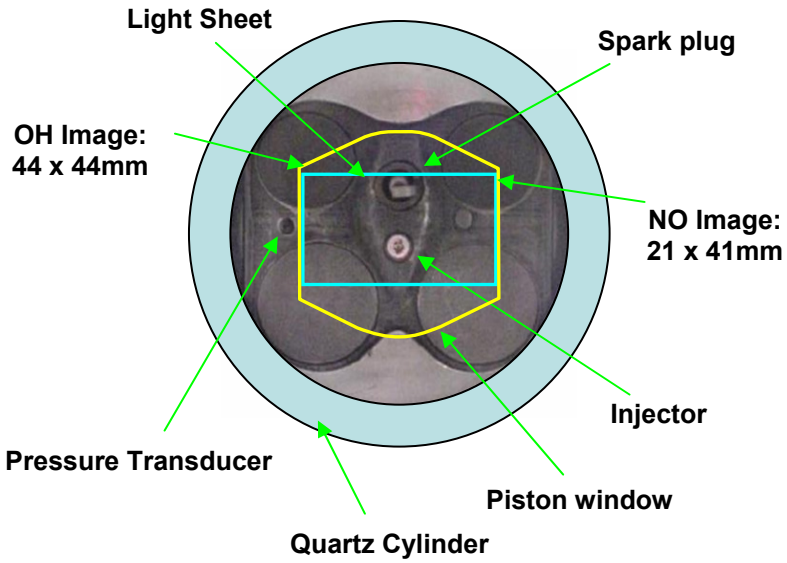


*Figure 5-9: The view through the piston crown towards the cylinder head. The yellow frame outlines the piston window. The blue frame indicates the LIF image area.*

### 5.3.1 UV-Chemiluminescence Setup

Chemiluminescence of OH radicals was recorded simultaneously with the NO PLIF images using a second intensified CCD camera (LaVision FlameStar IIF) using a UV objective (Halle, f = 100 mm) after the signals had passed through a set of four narrowband reflective filters coated for best performance in the range from 290 - 330 nm. The signals were separated with a dichroic mirror from shorter wavelength signals, i. e. the NO LIF signals. The gate width of the image intensifier was set to 10 µs for the chemiluminescence camera to acquire significant signals. This timing corresponds to approximately 0.12 CAD at 2000 rpm. The image intensifier was triggered with a delay of 1 µs to miss the laser pulse in order to avoid imaging of LIF from toluene or other combustion products.

# 6 Experiments

The experimental investigation of the nitric oxide formation described in this thesis can be subdivided in three parts: The comparison of early and late injection, the impact of intake air temperature, and the influence of intake air dilution. A representative point of operation was selected at 2000 rpm, near wide open throttle, and a constant fueling rate of 10 mg. This represents a steady-state cruise condition with highly stratified part-load operation with indicated mean effective pressures of 2 to 3 bar. [Drake, Fansler et al., 2003; Drake, Fansler et al., 2004] A preliminary study was necessary to characterize the optimal injection and ignition timings. All imaging experiments were conducted skip-fired to ensure thermal stability due to the relatively high friction of the unlubricated rings and the poor heat transfer of the quartz cylinder. Oil and coolant temperature were kept at 90º C. Also note that the fuel was 95% iso-octane and 5% toluene (by vol.) since this is a fuel mixture that is used frequently for fuel tracer measurements and we kept it to make sure that the combustion conditions remained unaltered [Zhang, Wermuth et al., 2004].

## 6.1 Optimization of Operation Parameters

The combustion stability in a highly stratified spray guided SIDI engine depends not only on injection and ignition timing but on the phasing of both events. The time lapsed between end of injection and ignition characterizes the mixture at the spark plug and therefore ignitability. The goal of the engine mapping is to assure a stable operation as indicated by a low COV of IMEP while maintaining a high IMEP. A number of spark - and injection timing sweeps have been conducted for various diluent rates and for 45º and 90º C. A dwell angle of 6 CAD between end of injection and ignition was found to yield the best COV of IMEP independent of end of injection. This was true even for conditions with nitrogen dilution. End of injection and therefore ignition timing had to be adapted to account for the longer flame development angle (see Figure 6-1 (b)), when EGR was added. The rapid burn angle is only marginally affected. The timings found for lowest COV of IMEP and highest IMEP respectively are presented in

Figure 6-1(a). The differences between both are on the order of 2 CAD or less, which was estimated to be within the uncertainty of the measurements. For all experiments the "best COV" injection and ignition timings were used. For operation conditions other than EGR, ignition and injection timing refer to Table 6-1.

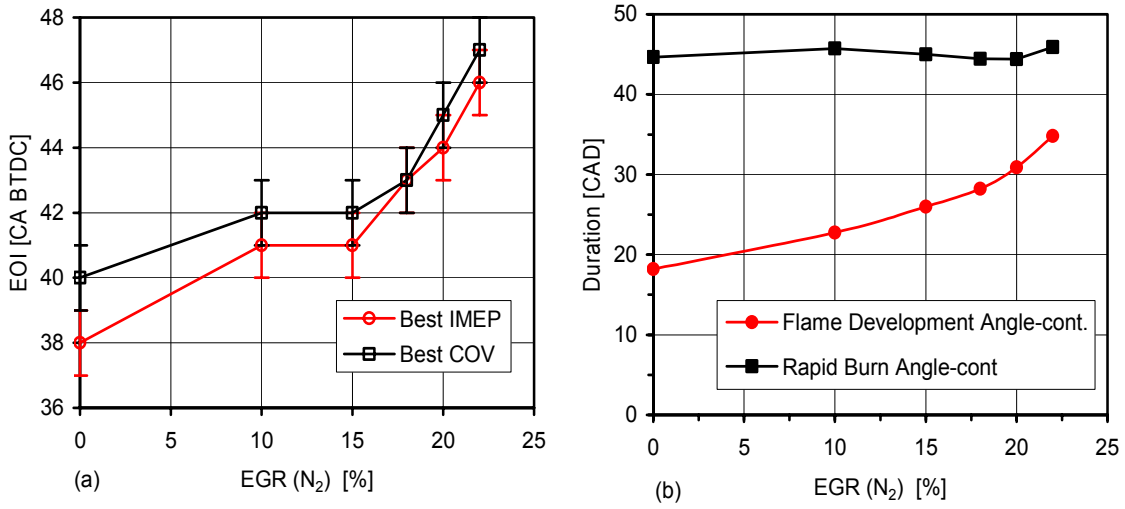


*Figure 6-1 (a): Injection timing for best IMEP and COV of IMEP respectively. The error bars represent an uncertainty of 1 CAD. (b) Impact of dilution on flame development and rapid burn angle.*

### 6.2 Comparison Stratified - Homogenous

A comparison between the characteristics of NO formation between stratified and homogeneous charge was made. The latter was achieved by injection during the intake stroke, while reducing the intake manifold pressure accordingly. The IMEP should stay roughly the same for both operational modes, while a slightly lean equivalence ratio was chosen under homogeneous charge to prevent NO reburn. Low and high swirl conditions were examined. The homogeneous condition was also used for the calibration of the LIF signal. A summary of the most important operational parameters is displayed in Table 6-1.

### 6.3 Effect of Intake Air Temperature and Dilution

Further two intake air temperatures and dilution with various amounts of nitrogen to simulate exhaust gas recirculation were compared. The timing was optimized for each EGR rate as shown in chapter 6.1. It was kept constant for the two intake air temperatures investigated. For details see Table 6-1.

*Table 6-1: Summary of operation conditions for stratified operation with varying degrees of dilution.*

| Engine speed | 2000 rpm | | | | | |
|---|---|---|---|---|---|---|
| Cycles skipped | 12 | | | | | |
| Oil / coolant temperature | 90 ºC | | | | | |
| Fuel | 95%Iso-octane/5%toluene | | | | | |
| Mode | Homogeneous | | Stratified | | | |
| Fuel mass / cycle | 13.3mg | | 10mg | | | |
| $\phi$ | 0.97 | | 0.37 | | | |
| MAP[1] | 45 kPa | | 95 kPa | | | |
| Swirl | High | Low | Low | | | |
| Intake air temperature | 90 ºC | | 45 ºC | 90 ºC | | |
| "EGR[2]" | 0% | 0% | 0% | 0% | 10% | 15% |

[1] Manifold Absolute Pressure
[2] EGR refers to dilution with nitrogen

# 7 Data processing and Evaluation

All of the data recorded besides the OH images required complex data reduction. The fast NO measurements required some post processing for its time response characteristics. Pressure traces were evaluated on an individual image basis. The problems with NO imaging as laid out in chapter 4.4 are addressed in the image correction procedure as laid out below.

## 7.1 Exhaust gas analysis

The Horiba NO system sampled from a mixing container (volume ~ 5 l) that was mounted after the exhaust runner. A 5 m long line delivered the gas sample to the NOx analyzer. The sample line for the fast NO system was introduced in the exhaust runner to extract gas approximately 15 mm behind one of the exhaust valves. Figure 7-1 shows an example of a time-resolved signal measured with the fast NO system. The transition time from the sample nozzle to the detector is approximately 11 ms. Figure 7-1 also illustrates the crank angle (time) frame after exhaust valve closing (EVC) in which the signals were integrated to obtain the data that are reported in the following as NO exhaust concentration data. The time integration approach was chosen for its simplicity.

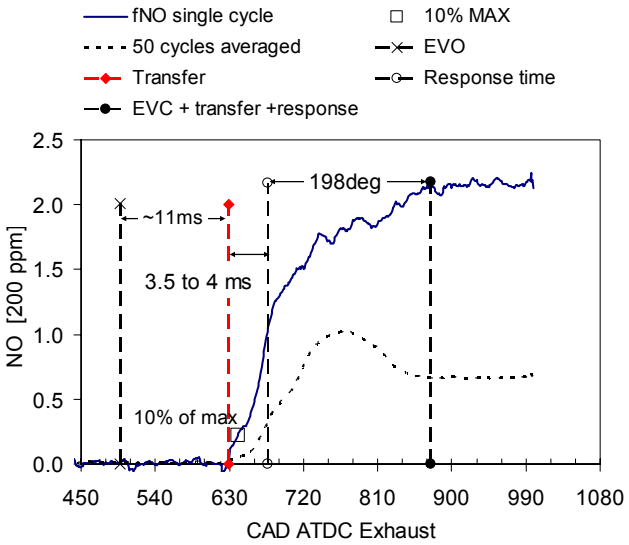


*Figure 7-1: Example of a NO signal measured with the fast NO chemiluminescence detector in the exhaust port.*

A number of researchers argued that the fNOx signal should be mass averaged to account for the highly unsteady flow of the exhaust gas during exhaust valve opening valve opening. [Ball, Stone et al., 1999] showed that NO concentrations obtained by time averaging are within 4% of those with mass averaging.

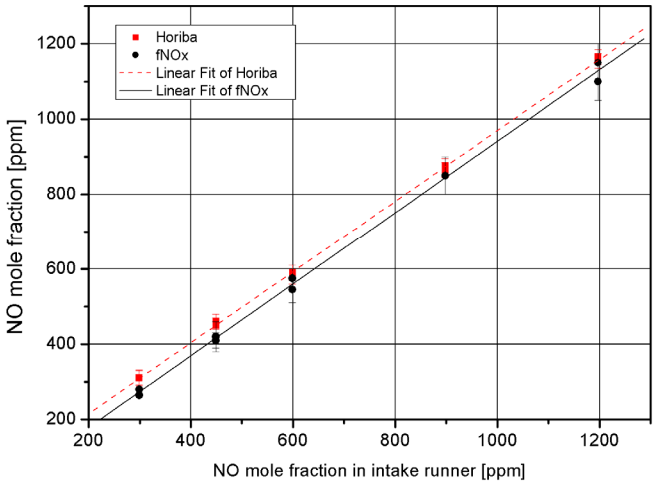


*Figure 7-2: Agreement in the readings of the fast NO and the slow NO emissions systems is found for motored engine tests with NO added to the intake air. No NO2 conversion was used. The lines illustrate the linear response of both devices.*

Both NO detection units were compared by measuring simultaneously from the exhaust while the engine was motored and known amounts of NO were added to the intake air (See Figure 7-2). A Tylan mass flow controller unit was used to select NO levels ranging from 300 ppm to 1200 ppm with a quoted accuracy of 1%. The $NO_2$ to NO converter in the Horiba system was turned off for this comparison; the Cambustion system was not equipped with a $NO_2$ converter. No corrections for water quenching have been made due to low humidity present. Even for combustion conditions, it was estimated that the quenching corrections would be on the order of 13% or less. Similarly, the difference between wet and dry emissions is small and not considered here. The errors shown in Figure 7-2 are estimated from the fluctuations in the readings of the instruments over the measurement period. Within these uncertainties, the agreement between the two instruments is excellent. This gives confidence in the use of the fast NO system for cycle-resolved measurements with skip-firing engine operation.

The finding is in agreement with the work of [Ford and Collins, 1999; Collier and Gregory, 2000; Puzinauskas, Olsen et al., 2003] who found the deviation of the fast exhaust gas analysis to a conventional system within 5%, 10% and 18% respectively.

### 7.2 Imaging

The NO PLIF images had to be processed in multiple steps to convert the raw fluorescence signals to NO mole fraction data (See Figure 7-3). This section describes the correction procedure and addresses systematic and random errors associated with the analysis.

The steady-state rate equation approach in the linear regime yields the following proportionality of the LIF signal with the number density of NO when laser light is absorbed via a single line :

$$I_{LIF}(p,T,\nu_{laser},x_{gas}) \sim f_B(T)\, N_{NO}\, I_\nu^0\, \Gamma(p,T,\nu_{laser},x_{gas})\, B \sum_i A_i / Q(p,T,x_{gas}) \quad (7.1)$$

where $f_B$ is the Boltzmann fraction of molecules in the ground state, $N_{NO}$ [$m^{-3}$] the total number density of NO molecules, $I_\nu^0$ [$W/cm^2$ $cm^{-1}$] the normalized spectral laser irradiance, $\Gamma$ the dimensionless overlap integral, $A$ [$s^{-1}$] and $B$ [$m^3/J$ $s^2$] the Einstein coefficients and $Q$ [$s^{-1}$] the quenching rate. It was assumed that $A << Q$. The summation $i$ is over all allowed emission transitions. The LIF signal is a function of pressure p [bar], temperature T [K], excitation wavenumber $\upsilon_{Laser}$ [$cm^{-1}$], and gas phase composition $x_{gas}$. A calibration is needed to account for optical and electronic efficiencies of the measurement equipment. Then eq. (7.1) can be scaled to yield absolute number densities from LIF measurements.

LIFSIM simulations were used to determine the expected dependence of the fluorescence signal on temperature, pressure, and gas composition. These simulations also take into account that usually more than a single transition absorbs the laser light. Measured fluorescence signals (at a given temperature, pressure, and gas composition) were then normalized by the corresponding LIFSIM value to obtain a relative NO number density. This procedure was first applied to calibration measurements where known amounts of NO were added to the intake air to determine the response of the optical system. In other words, this produced a calibration factor that was used to convert

camera counts into NO concentrations. NO values that are reported in this paper are given as mole fractions. Therefore, the results of the data analysis were normalized by the actual total number density as given by $N_{NO} = X_{NO} PVk/T$ . The introduction of T in the denominator into eq. (7.1) has been shown to reduce the temperature sensitivity of the LIF signal [Hildenbrand, Schulz et al., 2001].

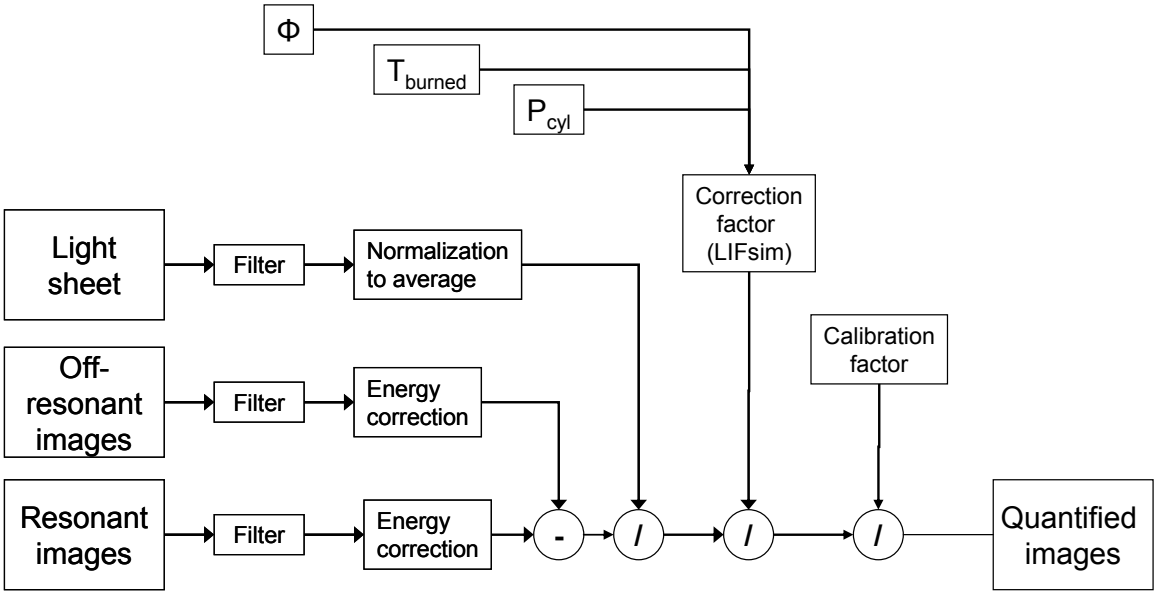


*Figure 7-3: Schematics of the correction process.*

### 7.2.1 Filtering

The level of NO concentration for the engine operation in this study can reach ~ 10,000 ppm at maximum with substantially less for most conditions. Even though a lens with large f# was used to collect signals, signals from a single cycle show significant shot noise. This is largely because excitation starts from the second vibrational level of the NO ground state and the associated low thermal population. As a result, the single cycle images exhibit a noise level that makes it difficult to correct the images for light sheet inhomogeneities etc. (as described below). The first step in the image processing routine therefore was a spatial filtering process with a median filter with a filter length of 5 pixels, which corresponds to 0.6 mm. This median filter removed outliers in the images that exhibited unduly high signal levels quite effectively. A further spatial filter, sliding average, with a filter size of 3 pixels (0.36 mm) produced images that could then be

processed further. It has been shown, that this approach reduces noise while preserving edge information [Schießl, Dreizler et al., 1999]. This filtering scheme was applied to both on- and off-resonant images. After the spatial filters were applied, each individual image was normalized with respect to the measured laser pulse energy.

### 7.2.2 Background Reduction

Background images were obtained with off-resonant (with NO) laser excitation. In comparison to other studies we selected a longer excitation wavelength (=248.08nm; See Figure 7-4) to avoid any potential NO excitation at higher pressures (line broadening effect). LIFSIM simulations were used to select the off-resonant excitation wavelength to correspond to a minimum in $O_2$ LIF signal levels.

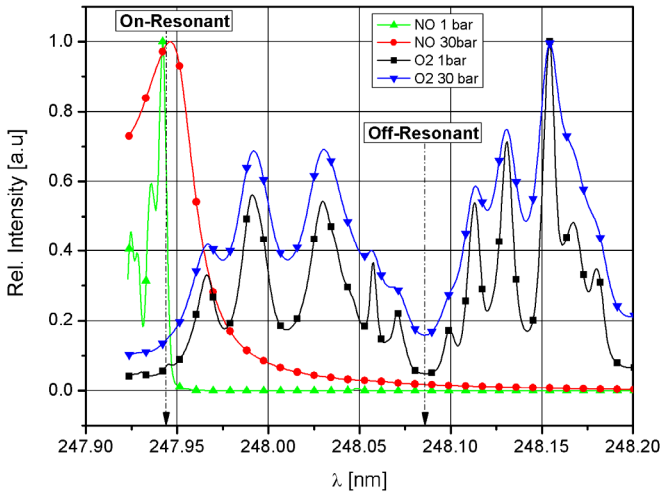


*Figure 7-4: $O_2$ and NO excitation spectra at 1 and 30 bar. On- and off-resonant laser wavelengths are marked by the dashed arrows.*

These simulations were experimentally confirmed to yield the same low level of $O_2$ signal in the NO detection bandpass as with an off-resonant wavelength of 248.07 nm. Any addition of NO, however, no longer produced an increase in measured off-resonant signals. Off-resonant excitation also yields LIF signals via broad absorption spectra of $CO_2$ [Bessler, Schulz et al., 2003] and PAH . The contribution to the measured LIF signals from these molecules is then also effectively removed from the NO LIF images via background subtraction.

The intensity of off-resonant signals relative to the on-resonant signals varied with crank angle as illustrated in Figure 7-5. It is apparent that the relative contribution of background signal to the overall signal is increasing for stratified engine operation. It is quite likely that, for stratified operation, locally fuel-rich conditions can lead to increased formation of intermediate PAH that in turn will produce a higher background signal.

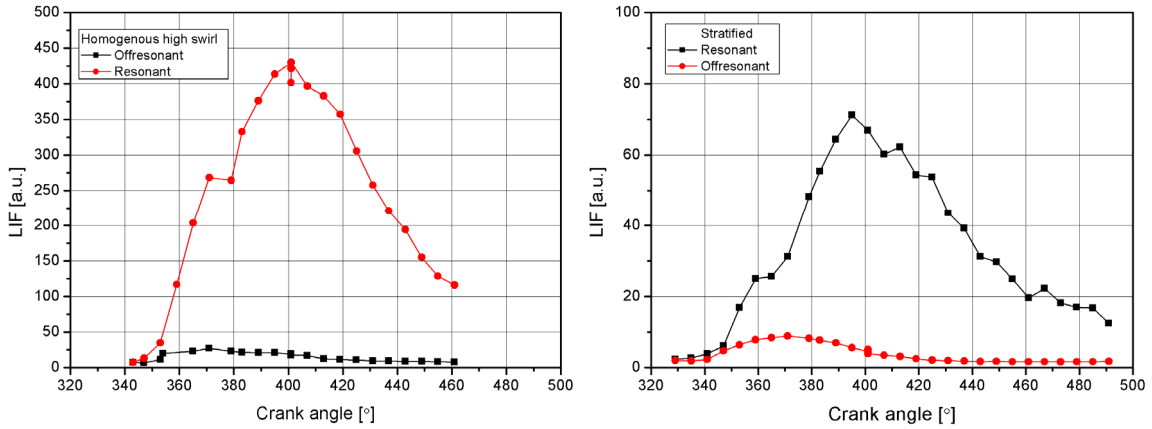


*Figure 7-5: Background fluorescence signal compared to NO LIF signal for homogeneous, high-swirl and stratified operating conditions.*

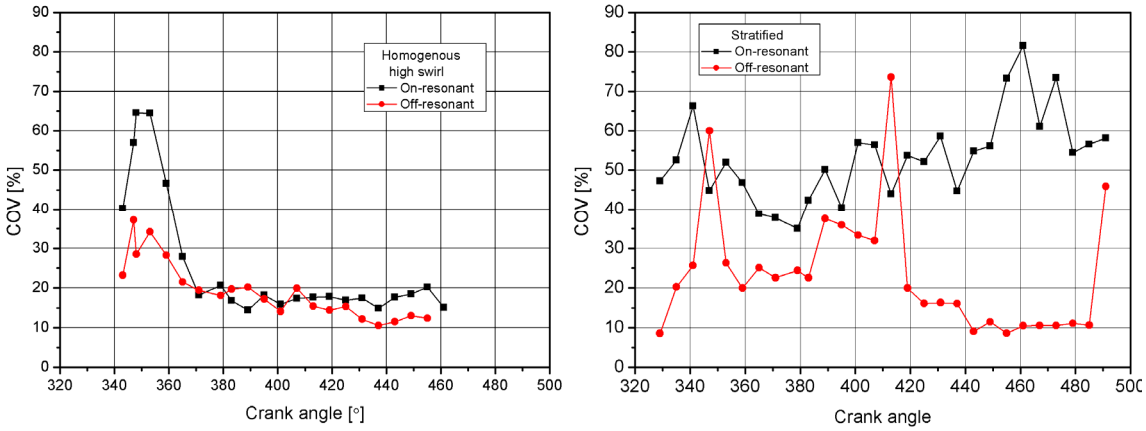


*Figure 7-6: The fluctuations of on-resonant and off-resonant signals are found to be similar for homogeneous engine operation. However, the variation of on-resonant signals is increased substantially for stratified charge.*

Averaged images of 50 off-resonant single-cycle images were computed for each crank angle and then subtracted from the single-cycle on-resonant images before proceeding. Note that an additional correction for light sheet intensity variations is necessary before the subtraction can be made. This will be described in the next section.

### 7.2.3 Light sheet correction

The filtered and energy-normalized on- and off-resonant fluorescence images were normalized with respect to the spatial laser energy distribution, i. e. the light sheet cross section. The laser light sheet intensity distribution was measured by introducing toluene into the motored engine and taking PLIF images at 60 CAD ATDC, after toluene had evenly mixed inside the engine. The second ICCD camera that was set up for chemiluminescence measurements around 310 nm was used for this purpose. The bandpass for these measurements is suitable to detect toluene LIF without any changes. Spatial registering between the two cameras ensured that the light sheet measured with one camera could be used to correct images taken with the other camera. After the sheet normalization process, the background (=off-resonant) images were subtracted from the NO images. The last step in the correction sequence was to account for temperature-, pressure-, and composition-dependent effects.

### 7.2.4 Spatial inhomogeneity issues

The following sections describe corrections and their influence on derived NO concentrations that were necessary to account for the effects of variable temperature, pressure, and mixture composition on the NO LIF signal strength. *Note: In principle, spatially resolved corrections are required to fully account for temperature, pressure, and mixture composition effects on LIF signal strength. Since the local values for these quantities can only be estimated within a range (to be discussed below), a fundamental level of uncertainty remains for the processed images. This affects in particular investigation of highly non-uniform conditions, i. e. stratified charge engine operation.*

### 7.2.5 Temperature Correction

The excitation scheme employed in this study yields strongly temperature-dependent LIF signals for temperatures below approximately 1800 K. The quantitative evaluation of measured PLIF images throughout the engine cycle therefore needs to include corrections for temperature variations. As already indicated in the previous paragraph, such a correction can only be applied globally, across the entire image, and therefore may be

limited in its local accuracy. However, the following discussion should illustrate the sensitivity to such an approach.

Temperatures were determined via a thermodynamic cycle analysis of the measured pressure traces for each individual cycle. However, since the temperatures are very different in burned areas compared to unburned areas, the thermodynamic temperature determination using a single-zone approach will only produce a bulk gas temperature that reflects an average temperature across the cylinder. For corrections of NO-LIF signals, however, temperature information about the hot, burned gas areas, are required. Bulk gas temperature and burned gas temperature approach the same level later in the cycle when all areas are burnt.

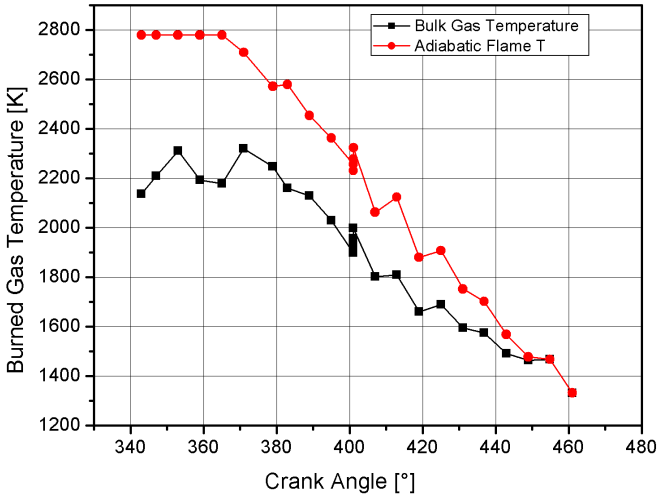


*Figure 7-7: Temperature profiles that were used to assess the overall sensitivity of the data reduction to temperature. These profiles bound the highest and lowest possible temperatures. See text for details.*

Figure 7-7 shows two temperature profiles that were used to correct the NO images obtained for homogeneous engine operation running at high swirl. The higher temperature curve was derived assuming that the temperature is given by the adiabatic flame temperature until the crank angle at which the maximum bulk gas temperature was determined. After this point the volume begins to substantially expand and then interpolation is used assuming a linear decrease of in-cylinder temperatures with crank angle towards the temperature at 460 CAD, which was determined from the thermodynamic pressure analysis. This was done on an individual cycle basis hence the slight scatter in the temperature data. The second data set shows the in-cylinder

temperature evolution based on the analysis of the bulk gas. In this case the burned gas temperature was assumed to be equal to the maximum bulk gas temperature from the start of combustion. After the crank angle at which the maximum bulk gas temperature occurs the burned gas temperature was assumed to be equal to the bulk gas temperature.

Both, the use of adiabatic flame temperatures or the bulk gas temperature for correction of the LIF signals is certainly extreme and unrealistic. However, as shown in Figure 7-8, the sensitivity of the result (NO mole fractions) is actually not too large.

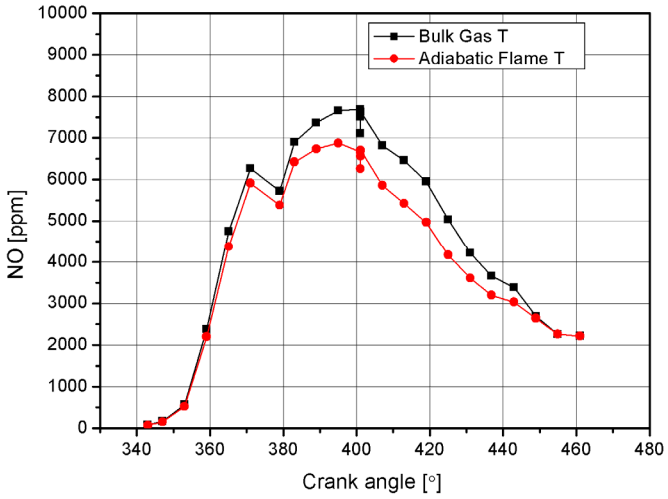


*Figure 7-8: The influence of the assumed temperature profile on the NO mole fraction is modest over the range shown. The two results shown illustrate the extreme outcomes if highest and lowest temperature assumptions are made as illustrated in Figure 7-5.*

Therefore, the initial choice of temperature profiles during the combustion phase and then a gradual transition towards the bulk gas temperature that can include cyclic variations appears reasonable and justified. However, if temperature drops below approximately 1500K, the sensitivity of the correction is very high and the errors in NO mole fractions will accordingly rise.

### 7.2.6 Quenching

The simulations shown in Figure 7-9 illustrate the combination of temperature and fluorescence quenching effects on LIF signals. Equivalence ratio affects measured signal strength because the exhaust gas composition changes and therefore the overall quenching rate changes. Interestingly, the highest quenching rate, hence lowest signal is observed for an equivalence ratio of 1. For this, the (relative) amount of water in the

exhaust is highest and therefore the quenching rate is high. Water is one of the strongest quenchers for NO at high temperature combustion conditions [Driscoll, Sick et al., 2002]. For changes in equivalence ratios from 0.8 to 1.2 the LIF signal (per molecule) does not change by more than approximately 12% over the temperature range of interest (>1000 K). As such, the use of exhaust gas composition to determine the concentration of major species quenchers of excited NO in the cylinder is justified, given the low sensitivity to variations. This also reduces the sensitivity of the resulting NO mole fractions to spatial variations in the gas composition.

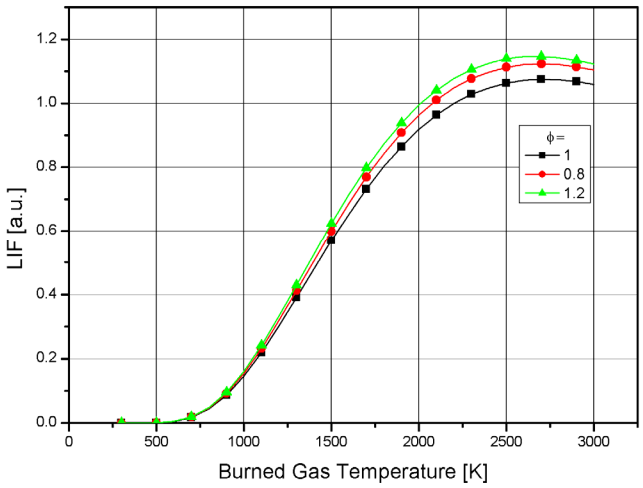


*Figure 7-9: The change of LIF signals (per mole fraction) via quenching is modest. The composition of the quenching gases is based on assumed exhaust gas composition for a range of equivalence ratios.*

However, for stratified-charge operation, the assessment of the quenching conditions is more difficult. Exhaust gas compositions cannot be directly used since the overall lean mixture composition is not representative for equivalence ratios where combustion (at least the bulk of it) occurs in the engine. For the reduction of the measured LIF signals for stratified engine operation we therefore used an equivalence ratio of 0.88. This is reasonable, because NO is mainly formed where local equivalence ratios are within 0.8 to 1.1 with a maximum around 0.9 [Akihama, Fujikawa et al., 1998]. Therefore the same conclusions about the variability of the quenching correction with temperature apply as they did for homogeneous mixing cases discussed above.

### 7.2.7 Absorption Signal / Laser

The NO images are also affected by absorption in the burned gas areas due to (mainly) hot $CO_2$ and to a lesser extent hot $H_2O$ [Schulz, Koch et al., 2002]. This absorption occurs for the laser beam and the LIF signal. The absorption path length for the laser beam can be directly determined from the NO images (=burned gas areas). The path length of burned gas (normal to the laser sheet direction) through which the signals travel has to be estimated. At early times this can be done by estimating that the flame kernel grows spherically.

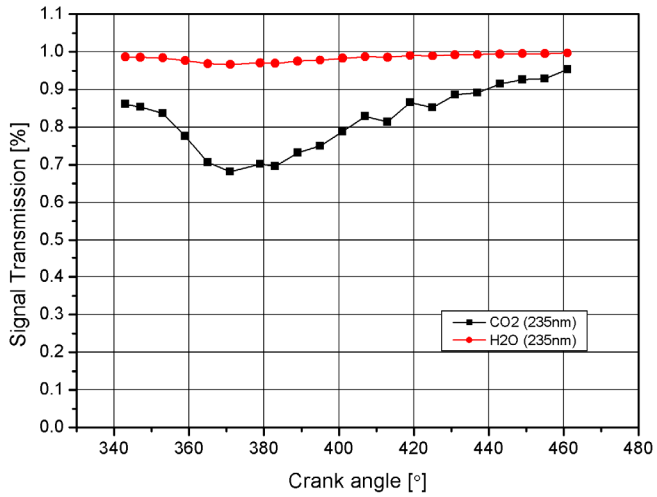


*Figure 7-10: Calculated signal transmission at the center of the detection bandpass (235nm) for homogeneous charge engine operation.*

With the bowl geometry of the engine under study, the flame reaches the bottom of the bowl within a few crank angle degrees and the absorption path length simply equals the geometric distance between laser sheet and bottom of the bowl. The temperature that was used to determine the absorption cross section for $CO_2$ was the same temperature that was used for computations of the quenching corrections..As such, temperature gradients near the piston were neglected. Figure 7-10 shows the evolution of the absorption of the LIF signals at different crank angles for homogeneous combustion. It is apparent that near TDC where the gases are hottest, the strongly temperature-dependent $CO_2$ absorption has its biggest effect. The result in Figure 7-10 illustrates the magnitude of the effect and while such data could be used to correct for some attenuation, we chose not to apply these corrections for two reasons. First, the NO-LIF signal calibration as a function of

added NO was performed under firing engine conditions (see below and in Figure 7-11) and therefore at least partially compensates for the effect of attenuation, especially towards the exhaust valve opening time. Second, especially under stratified-charge combustion conditions, the flame spread and NO distributions are so inhomogeneous, that a constant correction across a circular area approximating the flame front does no longer seem justified (equally relevant for temperature and quenching effects, see discussions of those above.)

Absorption as measured with the two photodiodes indicates even higher attenuation than the calculation. This is observed by [Suck, Jakobs et al., 2004] as well, where beam steering was identified as the main cause for the discrepancy between measured and simulated absorption.

Another source of light attenuation is the toluene tracer added to the fuel. In the homogeneous case the laser light transmission was estimated to be at a minimum of ~87% around top dead center, but to increase rapidly earlier in the compression stroke. Compared to regular gasoline, for which the transmission was estimated to be around 70% (based on the measured absorption coefficient of liquid regular gasoline that was adjusted for density of vaporized fuel [Wermuth and Sick, 2005]), absorption is small. However, in the stratified case locally high fuel concentrations or even droplets might be present and could cause intermittently higher absorption.

### 7.2.8 Calibration of corrected signal

For the calibration of the LIF signal strength as a function of NO concentration, the engine was operated with homogeneous charge, high swirl and an equivalence ratio $\phi$ of 0.88. PLIF signals were recorded at a crank angle position of 10 CAD BTDC. The equivalence ratio was chosen somewhat leaner than stoichiometric to ensure that no excessive NO reduction occurs [Schulz , Sick et al., 1999]

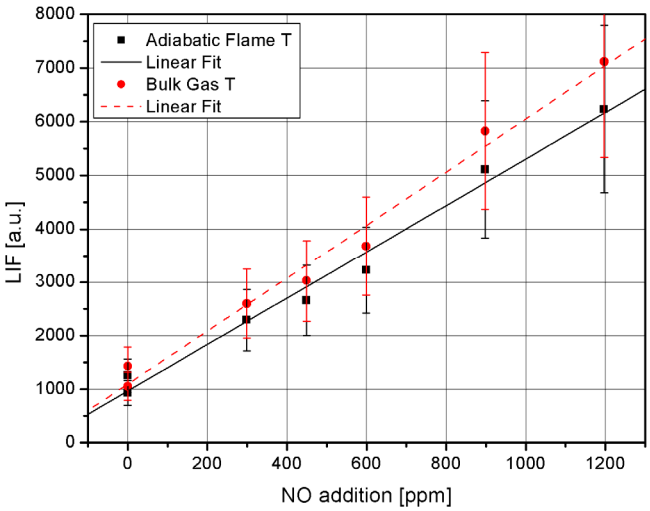


*Figure 7-11: A calibration constant can be derived, which includes all optical efficiencies and to some extent, the effects of absorption, from the measured linearity of measured (processed) LIF signals with added amount of NO to the intake air. Calibration images were taken at 10 CAD BTDC.*

These measurements were performed for 50 cycles for a range of known amounts of NO that was added. The result of this calibration measurement is shown in Figure 10. The calibration images were analyzed according to the same procedure as that described above. The resulting pixel values then were multiplied with a factor taken from the slope of a graph of processed pixel values vs. added NO concentration. This factor then includes all optical efficiencies since the setup is identical to the one used for the entire engine experiments. It also includes some of the attenuation effects due to absorption by hot $CO_2$; one of the reasons why we did not include this additionally in the data reduction process for the PLIF images.

Figure 7-11 shows data that were corrected based on factors derived with bulk gas temperature and adiabatic flame temperature, respectively. Calibration factors derived from each set are within 12% of each other. The equivalence ratio in the homogeneous case can be determined to within 3%. This uncertainty is governed by the metering error of air and fuel. The error in quenching correction resulting from uncertainty of composition under homogeneous conditions is estimated to be negligible. The calibration factor is assumed to be constant for all measured cases. Any error in this constant therefore impacts the absolute value of all measured concentrations. Thus, changes in NO concentrations that are observed for different operating conditions are not affected.

### 7.2.9 Error Analysis

As had been addressed earlier in this section, a quantitative interpretation of NO PLIF images is difficult. Within (mostly) assumed ranges of temperature and gas composition, the sensitivity of the result to these assumptions can be evaluated in quite some detail to provide better understanding of how significant the results are . Especially depending on the actual temperature conditions, the uncertainty can easily approach 50% or more. On the other hand, as was shown here as well, the quantitative agreement of processed NO PLIF images with exhaust gas measurements is very encouraging towards the use of the results for further investigations.

It has to be noted, however, that especially for highly stratified conditions, the assumption of spatially uniform temperature and gas composition may have a much more significant effect on the interpretation of NO PLIF images. One possible cause for occasional high levels of NO emissions for stratified charge operation may originate in spatial temperature peaks that lead to excessive NO formation. Depending on local temperature and quenching conditions, a local NO peak may be suppressed in the PLIF images.

The error introduced by the background correction is hard to quantify. In any case the background signal is approximately 10% of the signal. So the error introduced by the background correction cannot be more than 10% even if the background is 100% too high or too low.

Another important source of uncertainty is the absorption of both laser and signal light by $H_2O$ and $CO_2$. The transmission of signal light drops to 70% around 10º ATDC when number density and temperature are high but rises rapidly towards later crank angles. At the end of the expansion stroke transmission reaches levels of 90% and more. Laser light transmission follows a similar trend with the lowest transmission of ≈ 30% around 10 CAD to close to 0% at EVO. But one has to keep in mind that the laser beam is continually absorbed along the beam path. So the impact on the integrated signal is somewhat smaller. In a worst case scenario, the combined error due to absorption of laser and signal light can be estimated to 25%, when considering that the calibration partially compensates for absorption. The calibration itself introduces some error mainly due to temperature uncertainties, which is approximately 5%.

The total error can be calculated with $\frac{\Delta z}{z} = \sqrt{\frac{\Delta x}{x} + \frac{\Delta y}{y} + ...}$ to approximately 27%. This is of course a crude estimate, since the true error is dependent on so many parameters as discussed above.

# 8 Results

The results are separated in three parts for better comparison. The first part compares results from homogenous tests with a stratified point of operation with no exhaust gas recirculation and 90ºC intake temperature. In the second part we compare the influence of intake air temperature to the same stratified point of operation. Lastly the impact of EGR is investigated by adding various amounts of nitrogen to the intake air.

## 8.1 Comparison Homogeneous – Stratified

This study describes the comparison of the NO formation for two different direct-injection engine operating conditions, i.e. early fuel injection vs. late fuel injection. For late injection, the in-cylinder swirl was also varied as a parameter. Unthrottled operation of the optical single-cylinder engine at near-stoichiometric equivalence ratios is not possible because of the resulting high peak pressures at such high loads. Results that are reported for early injection are therefore from engine runs where the intake pressure had been throttled to 45kPa. In contrast to this, for late injection, unthrottled operation is possible since the overall equivalence ratio is low (~ 0.37) and peak pressures are well below the peak design pressure of the optical engine (~60bar). This difference in operating conditions needs to be kept in mind when discussing the results of this study.

### 8.1.1 Thermodynamics

The difference in cylinder pressure is illustrated in Figure 8-1, where averaged pressure traces (50 cycles) are shown for all three operating conditions. Interestingly, there is very little difference in the pressure trace for homogeneous operation with high in-cylinder swirl compared to operation with low in-cylinder swirl. This is in contrast to a previous observation for this engine made by [Frieden and Sick, 2003]. However, the earlier study had used a pressure-swirl injector, a flat piston, and operated the engine at a compression ratio of 11. The current engine configuration features a pronounced piston bowl and a compression ratio of 9. (see Chapter 6.1.1)

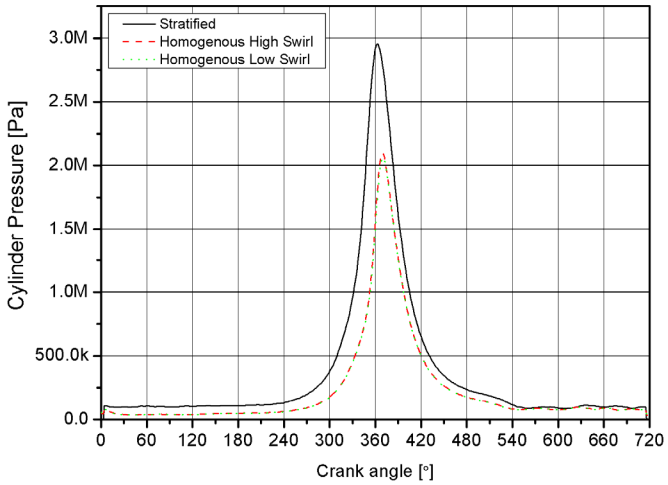


*Figure 8-1: Averaged (50 cycles) pressure traces for homogeneous and stratified engine operating conditions*

### 8.1.2 Flame front

The flame propagation can be studied via OH chemiluminescence. For stratified charge operation, the phase during which high levels of OH chemiluminescence signals are observed is shorter than it is for either of the homogeneous cases. The influence of the counter-clockwise swirl on flame spread is obvious from the image sequence in Figure 8-2. On average, the flame is moved to the side of the piston bowl by the swirling flow motion. For low swirl operation, the flame grows from the spark plug location and remains more centered in the bowl. Furthermore, it can be observed that the overall signal level is lower for stratified engine operation. This is best seen in the spatially averaged data presented in Figure 8-5(a). The error bars shown this figure (and subsequent similar figures in this paper) indicate a one standard deviation variation of the measured cycle-to-cycle fluctuation of the spatially averaged intensity based on image ensembles of typically 50 -150 individual cycle images.

The evolution of the OH chemiluminescence during the engine cycle shows a maximum after TDC for the homogeneous case and slightly before TDC for the stratified condition. A similar trend was also observed by [Stojkovic, Fansler et al., 2004] in an earlier study on soot formation and oxidation in direct-injection engines. During the expansion phase, the rapid decline of $OH^*$ signals indicates the end of combustion and decreasing temperatures.

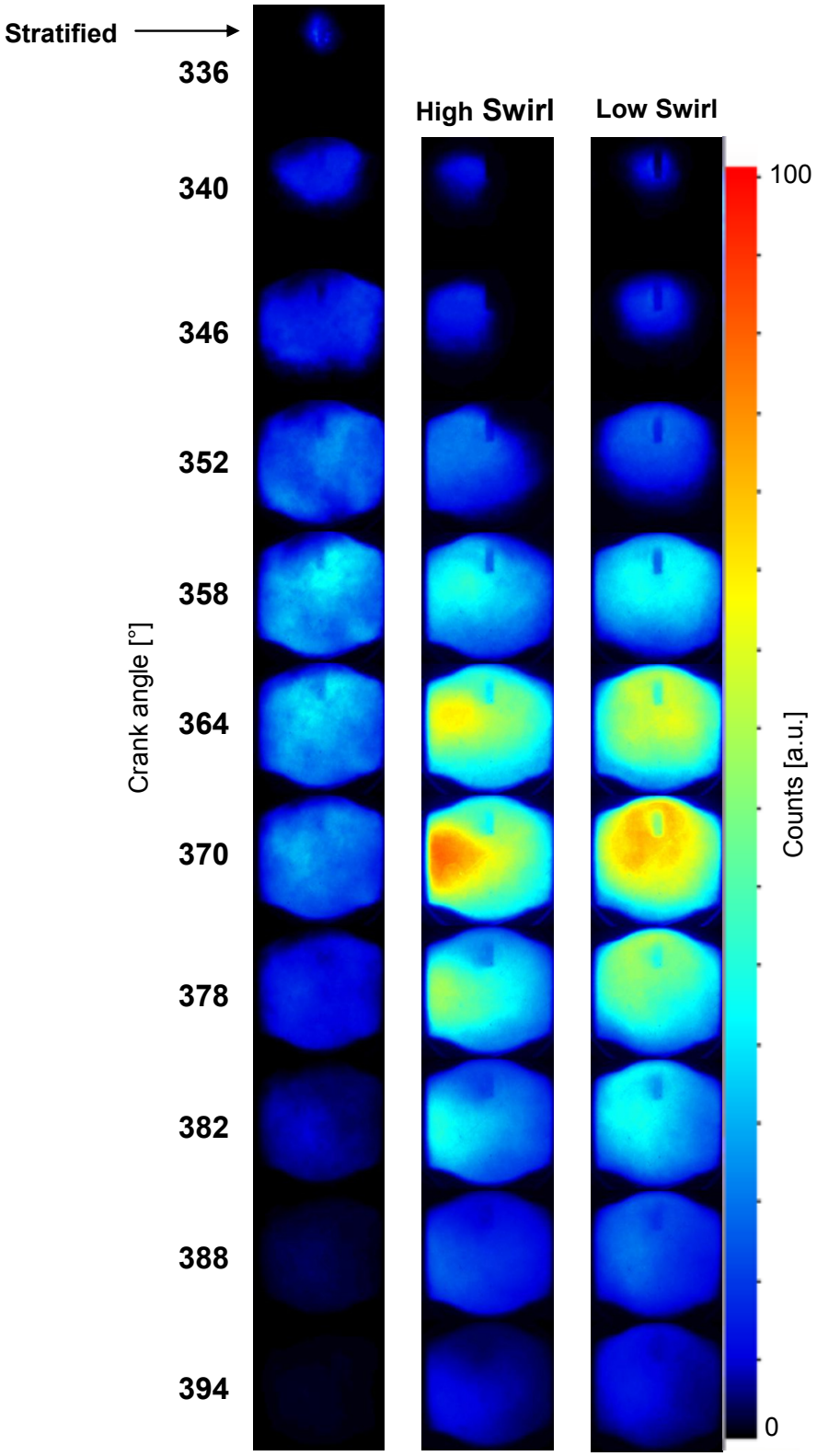


*Figure 8-2: Averaged (50 cycles) OH chemiluminescence images. Pronounced differences in flame spread patterns can be seen between operating conditions. The width of the images is 44mm*

The differences between $OH^*$ images from stratified and homogeneous operation become even more apparent when examining images from individual cycles. Figure 8-3 shows some examples of single-cycle images taken for homogeneous, high swirl conditions as well as for stratified operation. The images are selected for crank angles that correspond to maximum heat release rate. The $OH^*$ distribution for homogeneous conditions appears smooth and shows a consistent preference for the left side of the bowl. As discussed for the ensemble-averaged images (Figure 8-2) this reflects the influence of the swirl. In contrast to this, the images for stratified conditions are very inhomogeneous and show a strong structure with many areas where no combustion takes place.

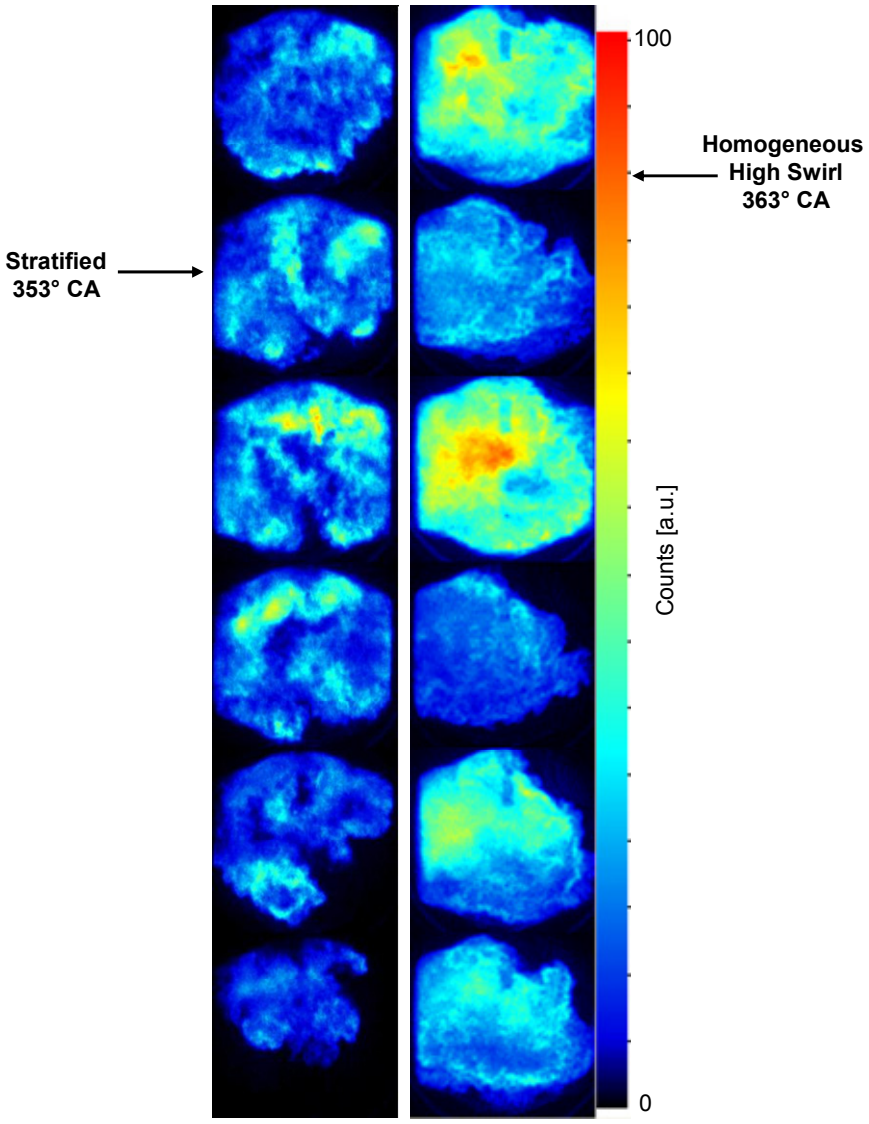


*Figure 8-3: OH chemiluminescence images taken at crank angle where maximum heat release rate occurs.*

### 8.1.3 Crank angle-resolved NO mole fractions

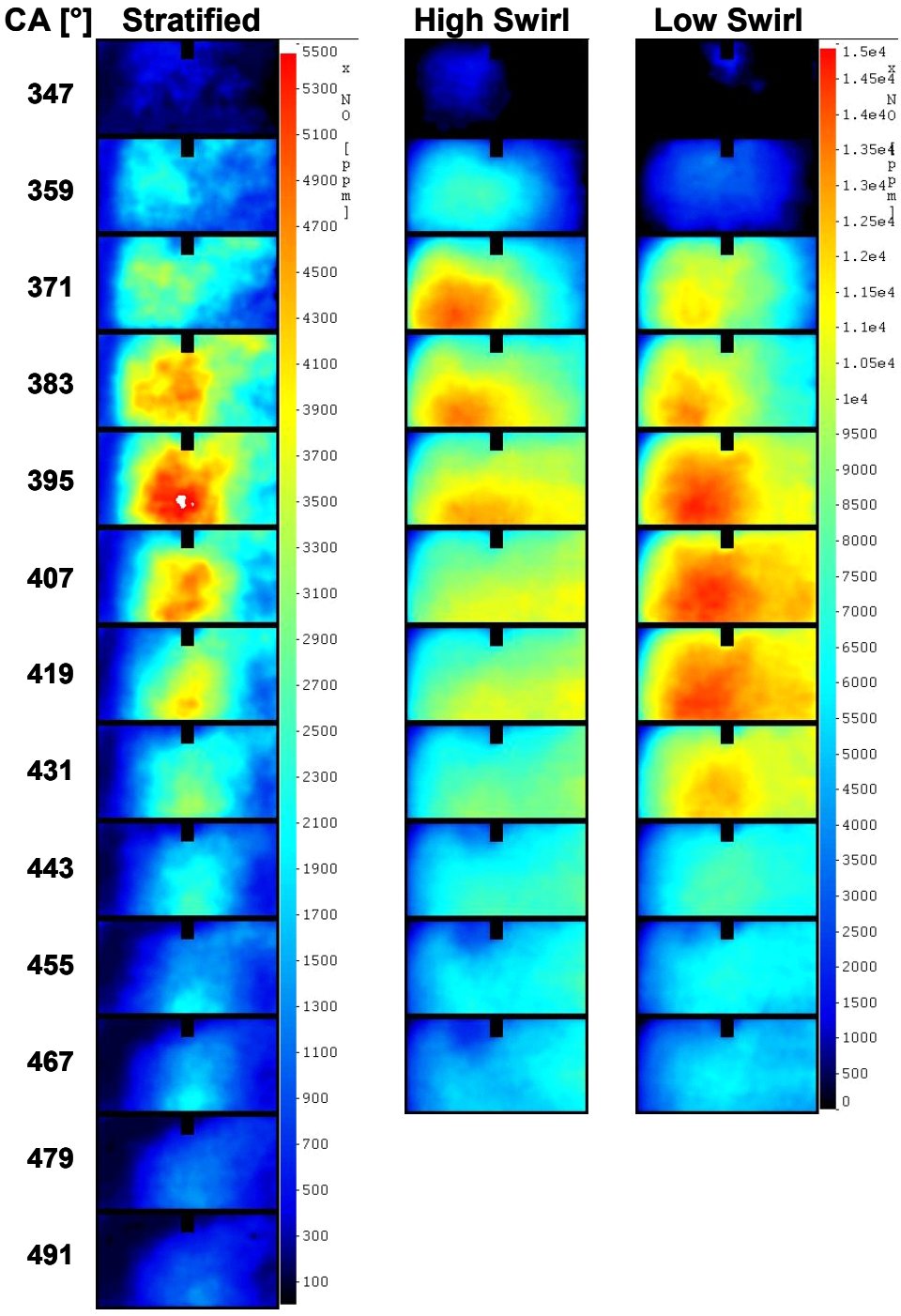


*Figure 8-4: Ensemble-averaged images (21x41mm) of the NO mole fraction distribution show a higher confinement of NO in the center of the piston bowl for stratified operation. The black, vertical, rectangle in the images marks the location of the spark plug. Note that the size of the images is smaller than those of $OH^*$.*

The observations made from the OH* images raise expectations for similarly strong differences between operating conditions in the NO distributions. Figure 8-4 presents an overview and comparison of ensemble-averaged (50 cycles) in-cylinder NO distributions. On average, NO is much more confined to the center of the piston bowl for stratified engine operation. For this type of engine operation, the goal is to concentrate the fuel cloud away from the walls and therefore NO will only be formed in these inner areas of the cylinder. In contrast to that, for early injection, where the fuel has time to mix with air throughout the cylinder, combustion will progress across the entire cylinder and will produce NO. The two right columns in Figure 8-4 clearly demonstrate this process. The evolution of the spatially averaged in-cylinder NO concentrations, from images as shown in Figure 8-4, is displayed in Figure 8-5.

After ignition, NO mole fractions begin to slowly increase at first, following the trend that was observed for the OH chemiluminescence. Then, for all operating conditions, NO formation accelerates and NO mole fractions in the 1000's of ppm are observed after TDC. Consistent with the inhomogeneity of the flame progress and continuing mixing as illustrated by both the OH* and NO images, the observed NO mole fraction values peak and then decrease substantially during the expansion stroke.

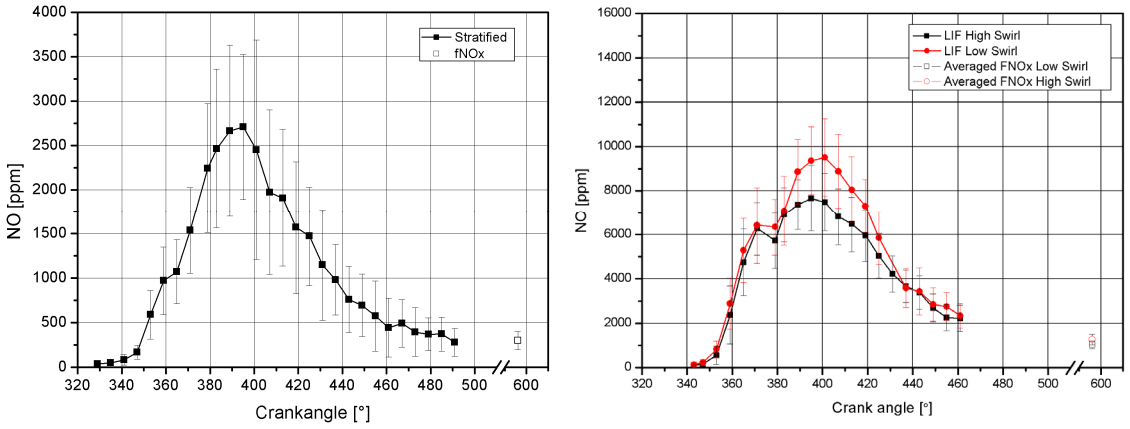


(a) (b)

*Figure 8-5: Spatial average of the ensemble-averaged images of the NO mole fraction distribution for stratified engine operation (a) and for early injection operation (b). The error bars indicate the range of NO mole fractions that were measured over 50 engine cycles. The data point at 580 CAD indicates the results of the measurements with the fast NO detector.*

Measured in-cylinder NO mole fractions approach the levels that were measured with the fast NO detector in the exhaust gas. More relevant discussion on this mixing effect and the limitations of PLIF measurements to provide a global measurement are given below.

The cyclic variability of the NO mole fractions is significantly higher for stratified engine operation (see Figure 8-5 ); the error bars in Figure 8-5 illustrate the range of measured NO levels. Figure 8-6 displays this as a COV of measured in-cylinder NO. Throughout the cycle, the NO levels vary in the range of 50% for stratified engine operation. Cyclic fluctuations in NO during homogeneous operation monotonically decrease until about 380 CAD and then remain at approximately 20%. The slight increase towards later crank angles most likely reflects increased uncertainty in temperature and its effect on calculated NO mole fraction (see section on temperature determination and its impact on NO evaluations).

The fluctuations observed in the cycle-resolved exhaust gas measurements compared very favorably with the PLIF data at 34% for stratified operation and substantially lower for homogeneous conditions with 16% for high swirl and 19% for low swirl flow conditions.

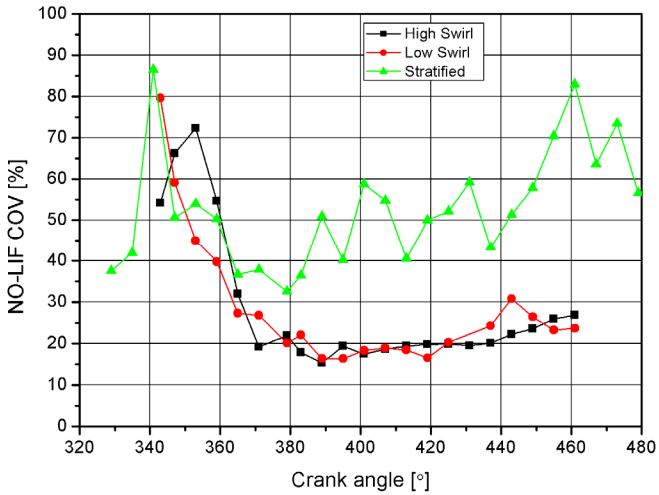


*Figure 8-6: Cyclic fluctuations of in-cylinder NO mole fractions are substantially higher for stratified engine operation.*

The NO images in Figure 8-7 illustrate the increased spatial variation in the NO distribution for stratified compared to homogeneous engine operation.

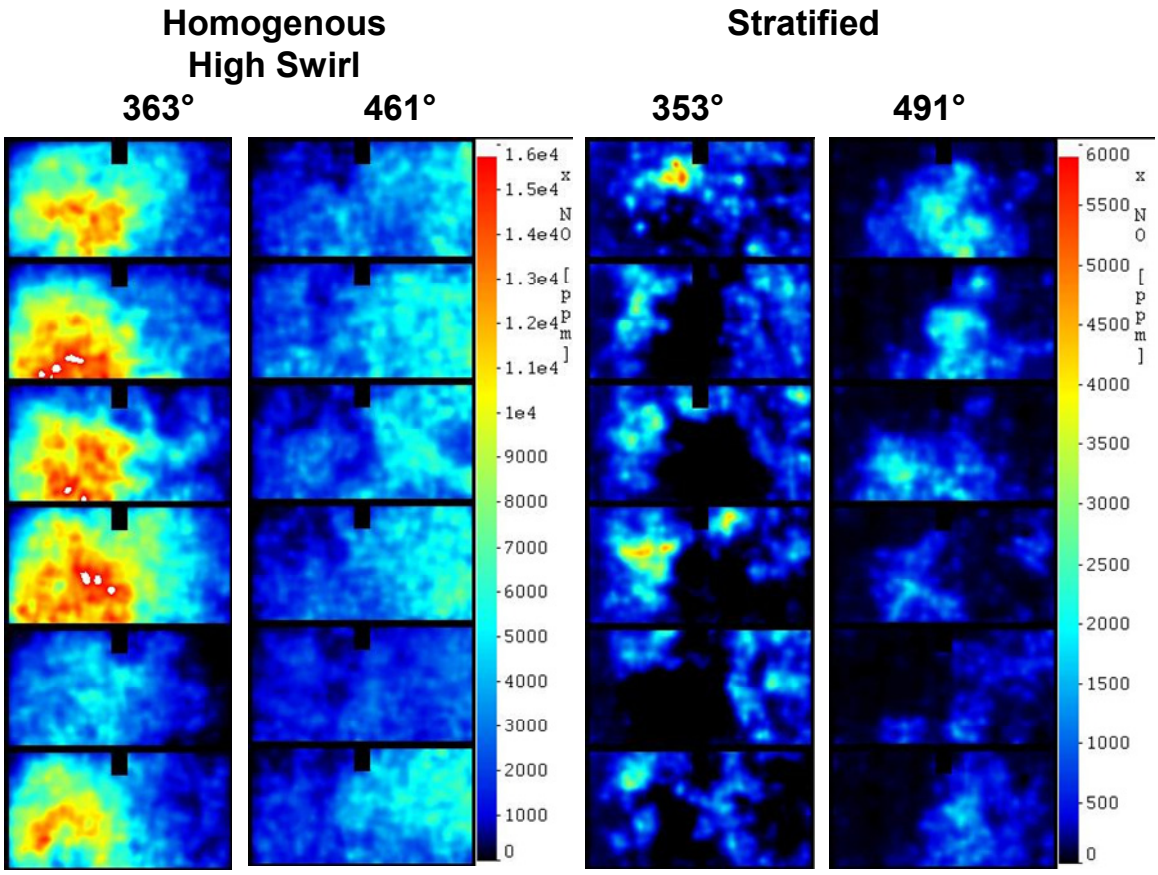


*Figure 8-7: NO mole fraction images, taken in individual engine cycles, illustrate the impact of mixture inhomogeneity on local NO formation. Compare this two-dimensional structure to the OH* structure shown in Figure 8-3.*

### 8.1.4 Correlation of in-cylinder data and exhaust NO levels

In this context, it has to be noted again that PLIF measurements provide information, albeit spatially highly resolved, in only two dimensions. Therefore, the observed cyclic fluctuations have to be further investigated to determine whether or not these are artifacts from sampling in only a "plane" that represents a fraction of the total in-cylinder volume. To facilitate this assessment, spatial averages of individual NO and OH images were compared to measured engine-out NO emissions for the corresponding cycles. Figure 8-8 shows a weak correlation between NO mole fractions measured with the fast NO detector and those determined by LIF imaging. The data do not show a clear trend as would be expected at least for homogenous engine operation. Combustion is complete at 461 CAD and the NO mole fraction does not change significantly beyond this crank angle (see Figure 8-5).

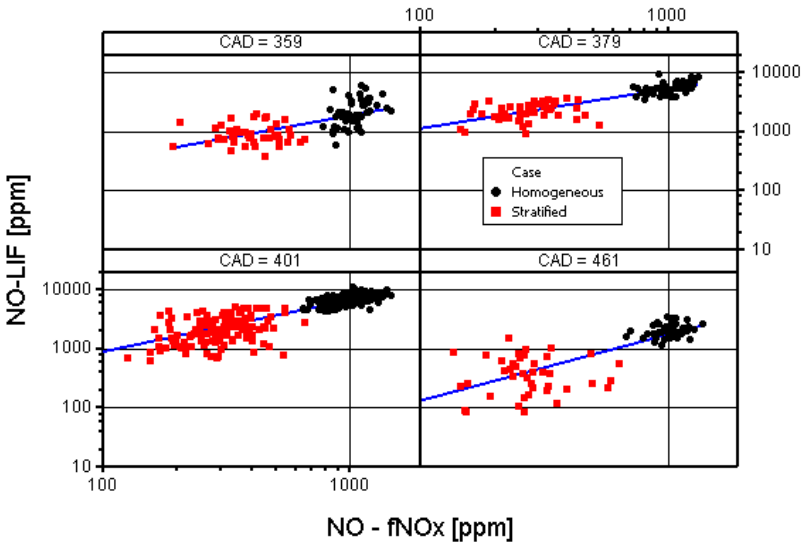


*Figure 8-8: Spatial averages of single-cycle NO in-cylinder concentration from PLIF measurements and NO exhaust gas measurements are only weakly correlated.*

Even though the data presented in Figure 8-5 show that the ensemble-averaged NO mole fractions from LIF and emissions measurements are in agreement shortly before the exhaust valve opens, this does not necessarily hold for cycle-by-cycle comparisons. As can be seen in the individual NO images (Figure 8-7), there are strong spatial variations within the cylinder. A single plane for PLIF measurements of the NO mole fractions is not in general a good representative of the overall cylinder volume. This effect adds to the fluctuation caused by cyclic variability of the combustion. The stronger scatter of the data taken under stratified conditions reflects the inhomogeneous nature of the combustion process. It seems that the mole fractions derived from LIF at 379 CAD and 401 CAD correlate better with the exhaust gas measurement than measurements taken at earlier (359) and later (461) crank angles. This would correspond to observations made by [Bessler, Hofmann et al., 2004]. Despite of the gas movement still proceeding after the end of combustion, it is surprising that LIF data taken later in the cycle would correlate less. One would expect that mixing is further proceeding and the NO stratification is reduced. The trend found from Figure 8-8 is confirmed with the data shown in Figure 8-9 where the average COV of the signal distribution over the image is shown. All graphs reveal a decreasing COV with increasing crank angle with a minimum around 400 CAD for high and low swirl cases. While the two homogeneous cases show a clear trend, the stratified case displays a strong scatter after 410 CAD.

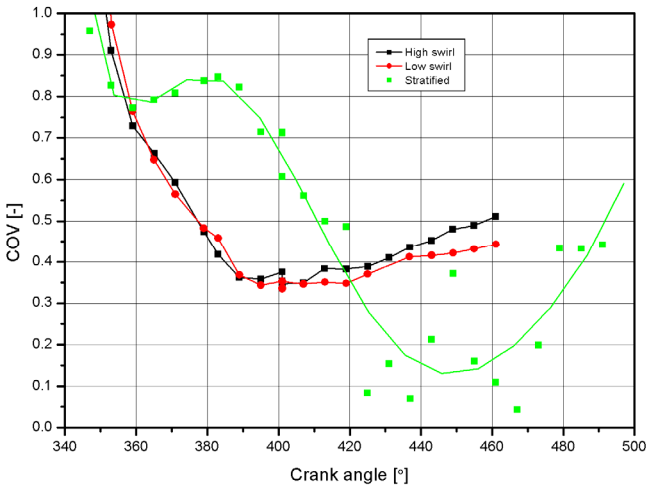


*Figure 8-9: The COV of the signal distribution over an image indicates the degree of uniformity of the NO mole fraction.*

However, the histograms in Figure 8-10 indicate, that the 50 images taken for each crank angle are not necessarily enough to draw a statistically valid conclusion.

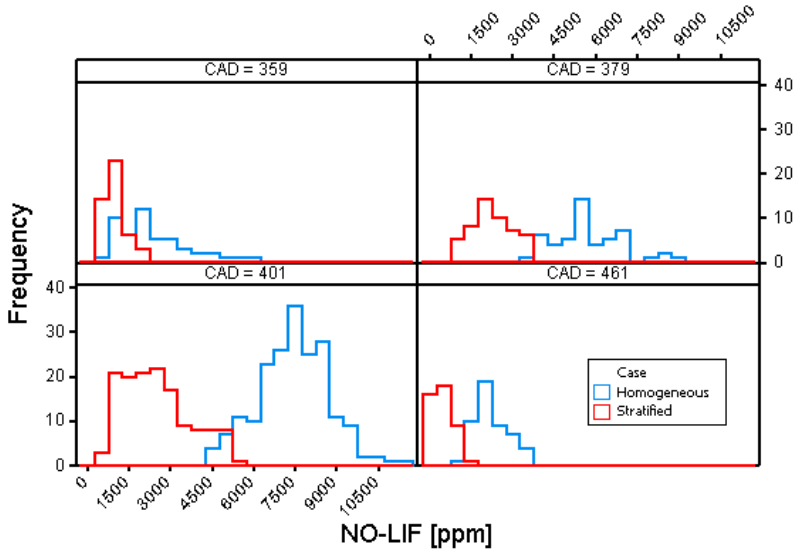


*Figure 8-10: Histograms of the spatially averaged NO mole fraction for selected crank angles. At each CAD 50 images were taken, except at 401 where 150 images were evaluated.*

At the beginning and the end of each crank angle series a set of 50 images at 401 CAD was taken to check the repeatability of the measurements. A total of 150 data points (images) are available for this crank angle. For this particular case a reasonable normal distribution is found, for all other cases the distribution seems somewhat skewed.

OH* signals that were recorded represent luminosity from the entire in-cylinder volume. If OH* could be related to NO PLIF results it may be possible to use the OH* signal to investigate fluctuations in NO production in a given cycle, without the need of NO PLIF measurements. Therefore, a first examination has to compare OH* with NO-PLIF data, as shown in Figure 8-11 and Figure 8-12 for stratified combustion. It is interesting to note that a significant level of correlation does exist between NO PLIF data and volume-integrated OH*. Most importantly, however, is to factor in that NO formation is a slow process and that measured exhaust gas levels represent the integrated amount that was produced during the entire cycle. In contrast to that, the OH* data provide information about the instantaneous condition of combustion.

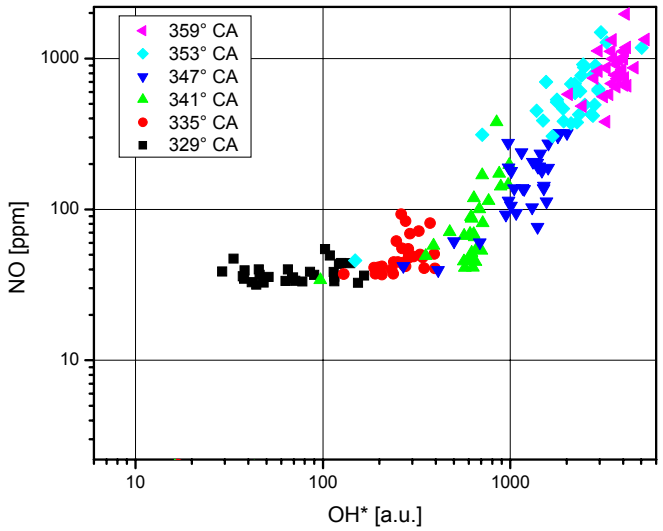


*Figure 8-11: During stratified engine operation, the measured NO concentrations correlate with OH* signals at early times during the cycle.*

Only if the evolution of OH* within a cycle always followed the same history a measure of the instantaneous values could be related to the overall combustion performance and eventually maybe related to NO exhaust levels. However, this seems unlikely, given the known cyclic fluctuations of combustion in internal combustion engines. Along these lines, it is observed that the correlation between NO PLIF and OH* does decrease over time (crank angle).

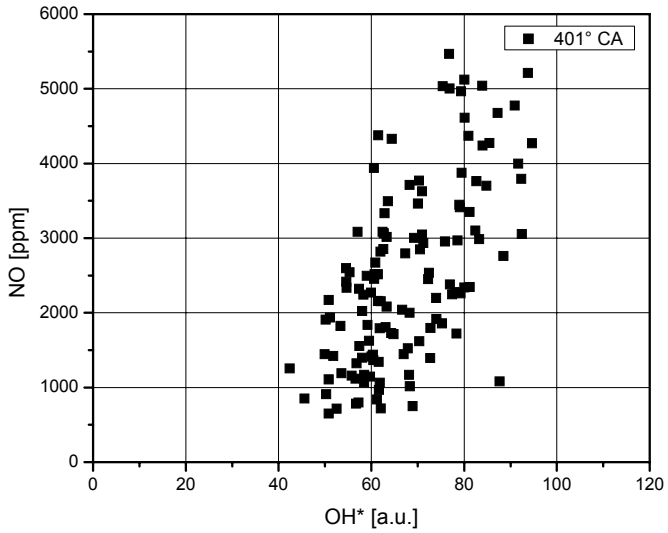


*Figure 8-12: During stratified engine operation, the measured NO concentrations correlate somewhat with OH* signals even late in the cycle.*

Figure 8-13 shows single-cycle spatially-averaged OH* signals at 379 CAD and the corresponding engine-out NO emissions. There is no correlation between the two signals. This might have two reasons. A high OH* concentration late in the cycle could be an indicator of a slow burning combustion cycle. This would result in overall lower temperatures and therefore lower NO emissions. On the other hand a high OH* signal could indicate a cycle with less stratification (compare Figure 8-3) which would result in higher engine-out NO emissions (Figure 8-5). These opposed effects could combine in not showing a clear trend at all. Hence, a correlation of instantaneous OH* signals, which provides information from the entire in-cylinder volume, with engine-out NO does not appear to yield a better correlation than in-cylinder NO PLIF data with engine-out NO. Similarly, instantaneous NO distributions have pronounced spatial concentration gradients for stratified engine operation – following the initial flame structure. The stratification in the NO distribution remains until very late in the exhaust stroke. Despite some limitations towards truly quantitative NO concentration data within individual images, fluctuations and average data are in very good agreement with ex-haust gas measurements. Cyclic fluctuations of in-cylinder NO decrease monotonically towards the exhaust stroke and stabilize at a COV of 20%. For stratified operation, the COV of NO remains at levels of 50% through the entire cycle. These results compare quite favorably

with data from cycle-resolved NO exhaust gas measurements, where fluctuations of 16% and 19% were found for homogeneous operation and 34% for stratified charge operation.

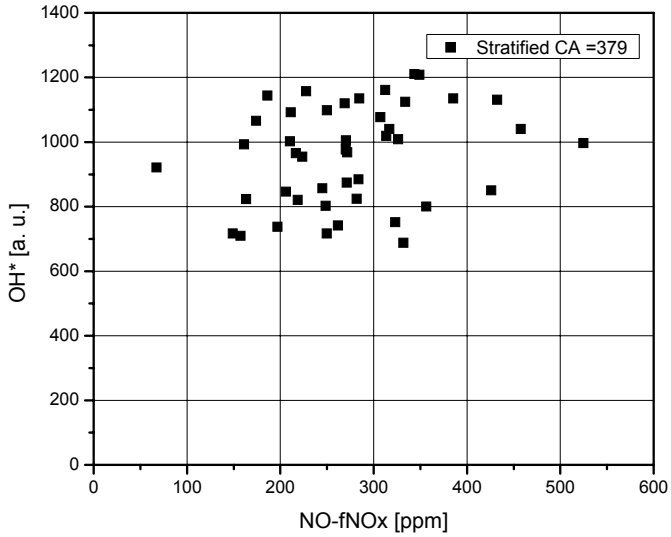


*Figure 8-13: Spatial averages of OH* do not correlate with engine-out NO concentrations.*

No significant correlation of the in-cylinder NO measurements with the fast NO measurements in the exhaust on a cycle by cycle basis was found. In-cylinder stratification, even for early injection operation, seems to be large enough such that the amount of NO that is measured within the laser light sheet is not representative for the overall cylinder contents for the engine under investigation.

A significant correlation between OH* signals and NO PLIF data but not with engine-out NO emissions was found. OH* imaging could therefore not be used for an assessment of cyclic variations of total in-cylinder NO, i.e. engine-out NO.

## 8.2 Impact of Temperature on NO Formation

The performance of the engine and NO exhaust gas concentrations for different operating conditions are displayed in Figure 8-14. The highest indicated mean effective pressure (IMEP) is achieved for an intake temperature of 45 °C. Increasing the intake temperature did not significantly change the measured IMEP and had only a small (positive) effect on COV of IMEP. The average nitric oxide engine-out emissions, as shown in Figure 8-14, were reduced by more than two thirds with a lower intake temperature.

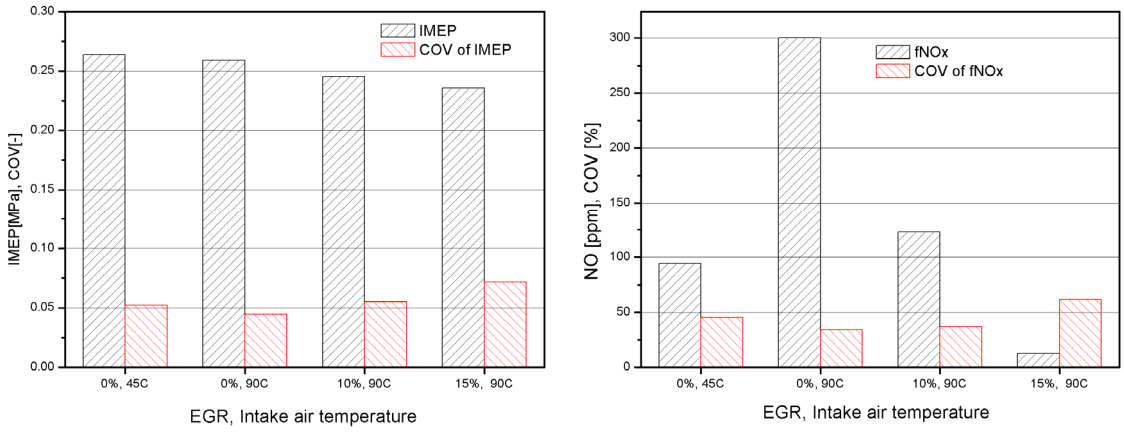


*Figure 8-14: Impact of intake air temperature and EGR on engine–out nitric oxide and IMEP.*

### 8.2.1 Combustion progress

Increasing the temperature of the intake air led to substantial changes in all observed in-cylinder quantities. While the pressure traces for both conditions are very similar as shown in Figure 8-15 it is noticeable that the heat release rate increased faster and reached somewhat higher levels for engine operation with higher intake air temperature (Figure 8-16). Increasing the intake temperature also advanced the combustion phasing. These findings are then compared to the ensemble average of the spatially averaged OH*-intensities over crank angle as illustrated in Figure 8-16(b).

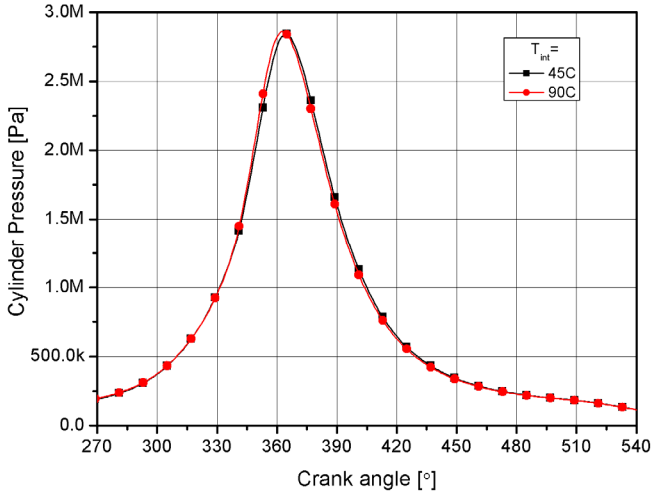


*Figure 8-15: Cycle-averaged (50 cycles) pressure traces are very similar for engine operation at different intake air temperatures.*

The rate of increase as well as the absolute magnitude of the OH*-signal is significantly higher for the 90 °C case as compared to the 45 °C intake air temperature case. It has to be stated, that for the lower intake air temperature the point at 360º is missing, which shows the highest intensity for the 90 °C case.

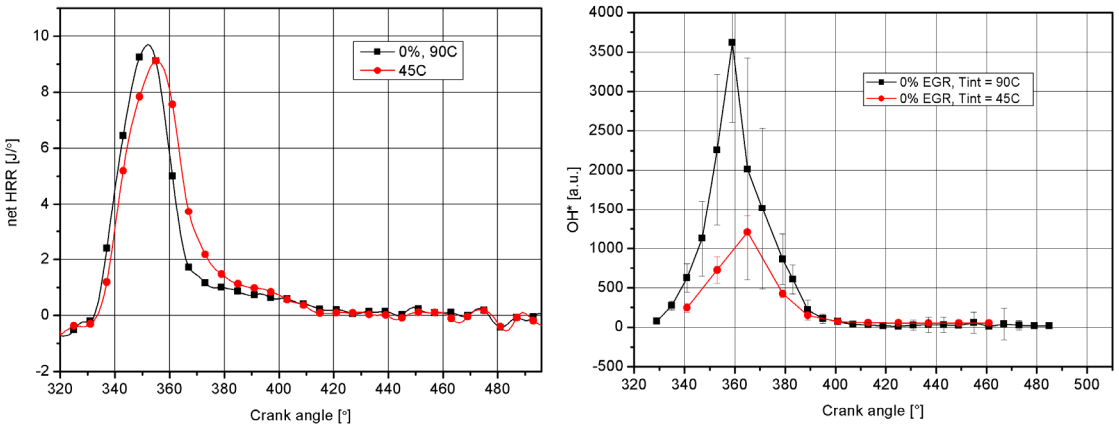


(a) (b)

*Figure 8-16(a): Heat release rate is affected by an increase in the intake air temperature. (b): The averaged OH* chemiluminescence signals reflect the increase in heat release rate for engine operation with higher intake air temperature with higher signal intensity during the combustion.*

Spatially averaged OH chemiluminescence data show similar trends as the heat release rate. However, the observed chemiluminescence signal evolution exhibits a time lag compared to the heat release rate data.

Additional information can be obtained from the averaged OH chemiluminescence images shown in Figure 8-17. They display noticeable differences in both intensity (as summarized in Figure 8-16(b)) and signal distribution for the two different intake air temperatures. For engine operation with lower intake air temperature the images display significantly less intensity and also a shift in the intensity distribution more towards the periphery of the area under observation. Note that this area shows the entire cross section of the piston bowl. Increased intake air temperatures could promote the evaporation of the injected fuel leading to a more homogenized air-fuel mixture and in turn a more evenly distributed combustion process.

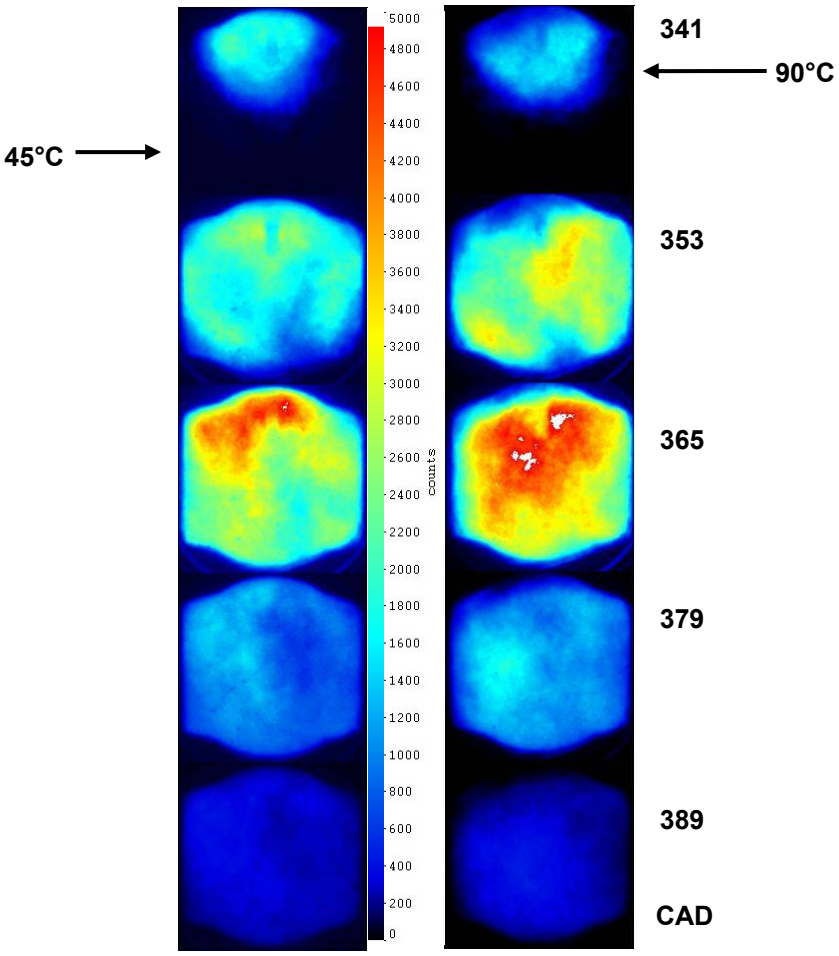


*Figure 8-17: For 90°C intake temperature the OH* intensity (averaged over 50 images) is higher and more evenly distributed than for 45 °C.*

Images from individual cycles shown in Figure 8-18 were taken at 353º, which is around the crank angle where the maximum heat release rate occurs. The images taken at the higher intake air temperature show substantially higher OH* intensity in regions scattered everywhere in the piston bowl. Most of those images indicate a more advanced combustion in agreement with the earlier heat release rate and the spatially averaged OH-chemiluminescence shown in Figure 8-16(b) and Figure 8-17, respectively.

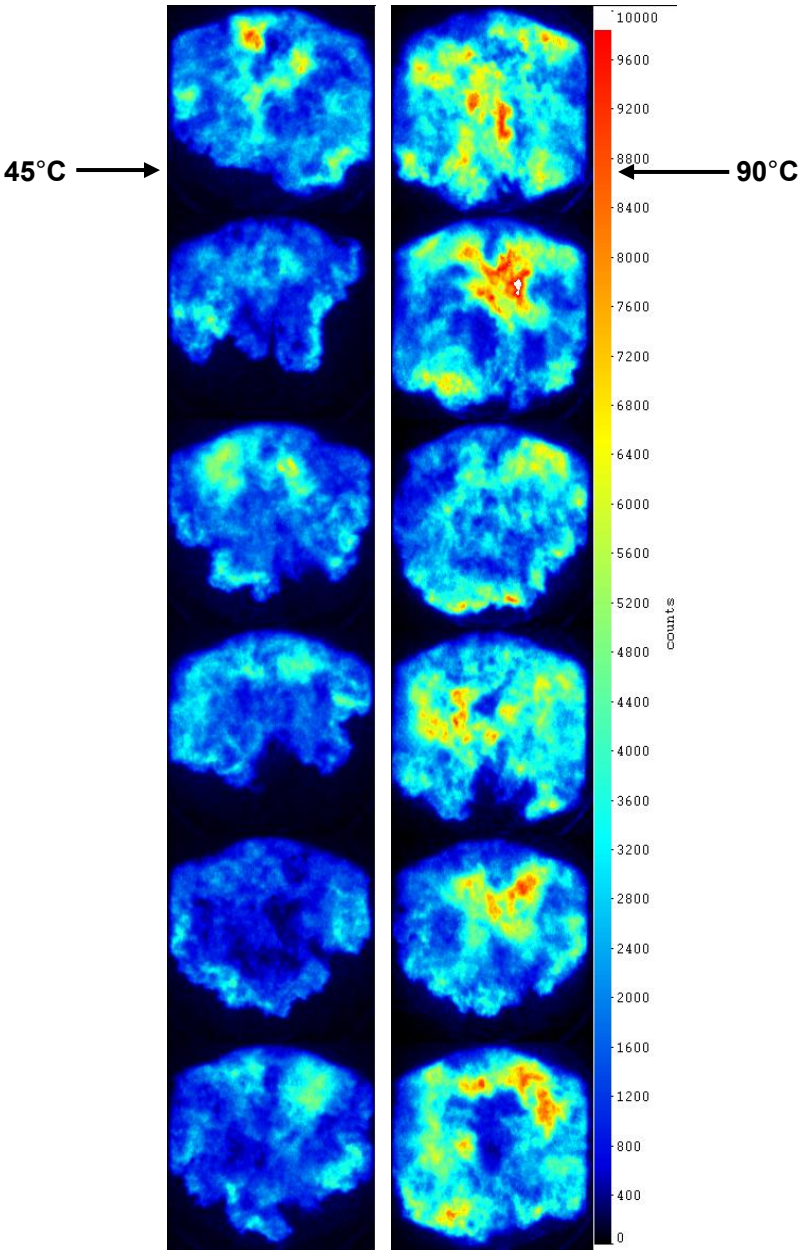


*Figure 8-18: For 90 °C intake temperature the OH* intensities in single cycles are higher and more evenly distributed than for 45 °C. Both images are taken at 353 °CA.*

In contrast to this, the chemiluminescence intensity distributions that are observed for lower intake temperature operation more often resemble the structure of a horizontal cross section of the original fuel jets. This again indicates that evaporation of the fuel is retarded for lower intake temperature. The individual images show more clearly than the ensemble averaged images that the flame has not fully filled the piston bowl.

### 8.2.2 Nitric Oxide

The exhaust gas measurements as shown in Figure 8-14 illustrate the strong impact of increasing intake air temperature on integral NO concentrations. Raising the temperature from 45 °C to 90 °C led to an increase of the NO exhaust concentrations by a factor of three. In contrast to this, the in-cylinder measurements in a single plane show a substantially different behavior (Figure 8-19). The ensemble averaged spatial averages of the NO mole fraction reach comparable peak levels for both cases. The increase is almost identical for both cases until the maximum is reached around 400 CAD. At later crank angles the lower intake air temperature case actually shows higher nitric oxide levels until the end of the expansion stroke.

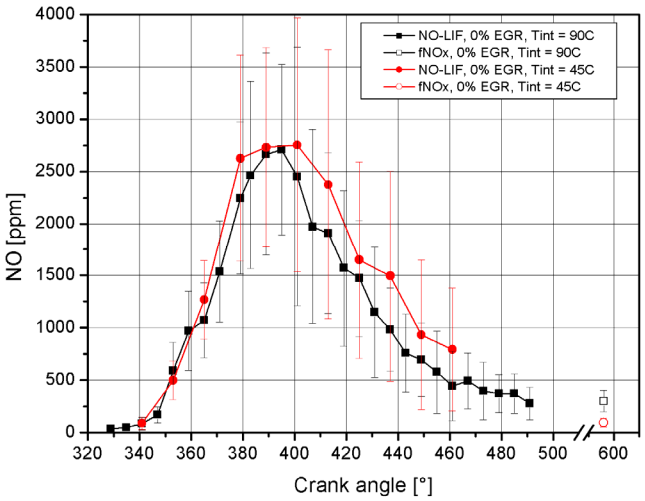


*Figure 8-19: In-cylinder ensemble and spatially averaged (50 cycles) NO concentrations. NO formation with 45 °C intake air temperature compared with 90°C. For 45 °C NO reaches approximately the same peak concentrations but NO levels seem to be delayed. Error bars illustrate the cyclic variation in NO concentrations. Open symbols show the exhaust gas data.*

This is in contrast to the exhaust gas measurement. It has to be stressed that only a small volume is probed with the LIF technique as opposed to the exhaust gas measurement, which gives a volume-averaged measure of the NO concentration.

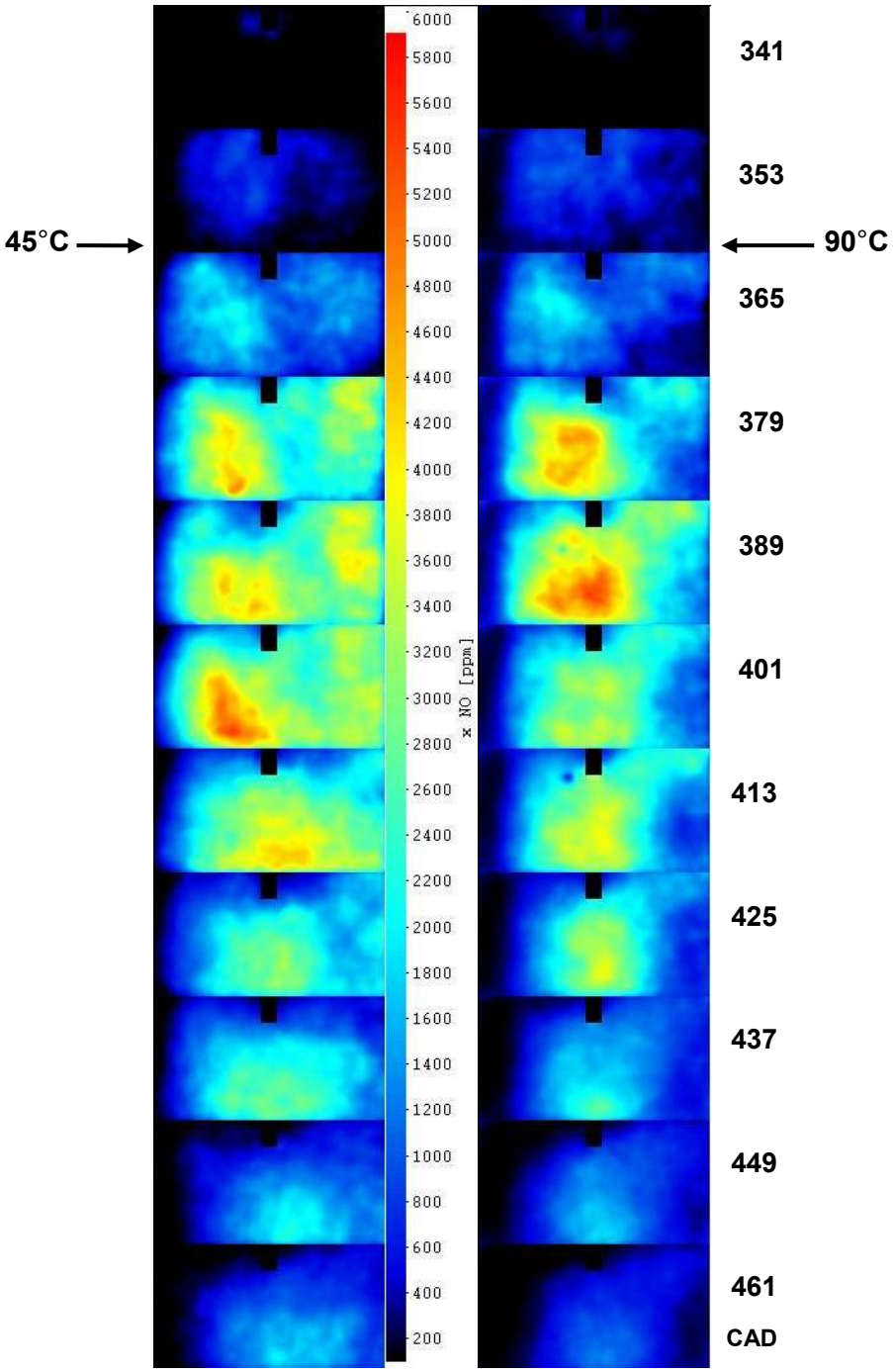


*Figure 8-20: Impact of intake air temperature on spatial and temporal NO formation. Images shown are averaged over 50 cycles.*

Given the higher stratification in the combustion as illustrated by the OH chemiluminescence, it appears reasonable to assume that the observed locally high NO concentrations may not be representative for the entire in-cylinder volume. As with the exhaust gas measurement, (Figure 8-16(b)) the cyclic variability as symbolized by the

error bars is substantially increased for low intake air temperature. The agreement between imaging results late in the cycle and fast exhaust gas measurement is very good for an intake air temperature of 90 °C. It appears that mixing of the produced NO for the low intake air temperature case is not completed at the latest crank angle that was measured. The NO mole fraction images averaged over 50 cycles are depicted in Figure 8-19. The images taken at a lower intake air temperature show lower and less dispersed NO concentrations for early crank angles. Later in the stroke the images exhibit significantly less stratification. This is coherent with the trend observed in the OH* images (Figure 8-17).

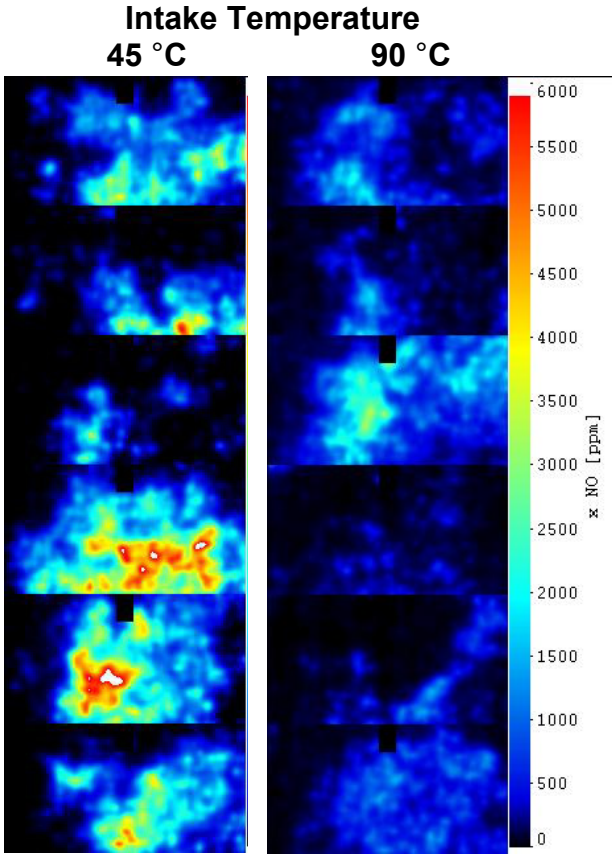


*Figure 8-21: Single shots of NO concentrations taken at 461 CAD, shortly before exhaust valve opening*

The individual NO images taken at late crank angles (Figure 8-21), despite strong cyclic variability manifested in very different distributions, reflect the trend of higher concentrations at late crank angles for lower intake air temperature shown in Figure 8-19

and Figure 8-20. It is also interesting to note the persistent inhomogeneity in the NO distributions late in the engine cycle. This observation has to be kept in mind when comparing in-cylinder with exhaust gas measurements. From the chemiluminescence images one may expect to find a broader NO distribution for the high intake air temperature case. However, upon examination of individual chemiluminescence images it is plausible to expect initially more localized NO concentrations for low temperature and then mixing will disperse the NO. The random nature of this process eventually can lead to the observed broader distribution in the ensemble averaged NO images for low intake air temperature operation. This is a critical finding that has implications towards the interpretation of the NO formation pattern.

## 8.3 Impact of EGR on NO formation

Three EGR cases were compared by thermodynamic analysis, fast exhaust gas analysis, NO-LIF imaging and OH-chemiluminescence imaging. Recall that EGR was simulated by adding nitrogen to the intake air via a critical orifice setup. As shown in Figure 8-14, with the addition of nitrogen to the intake air, IMEP decreases and COV of IMEP increases substantially As is well-known, EGR reduces engine-out NO emissions strongly. The addition of 10% nitrogen led to a drop in NO to about half, while 15% EGR reduced engine-out emissions to one tenth. The COV of NO follows the same trend as the COV of IMEP with increasing EGR rate.

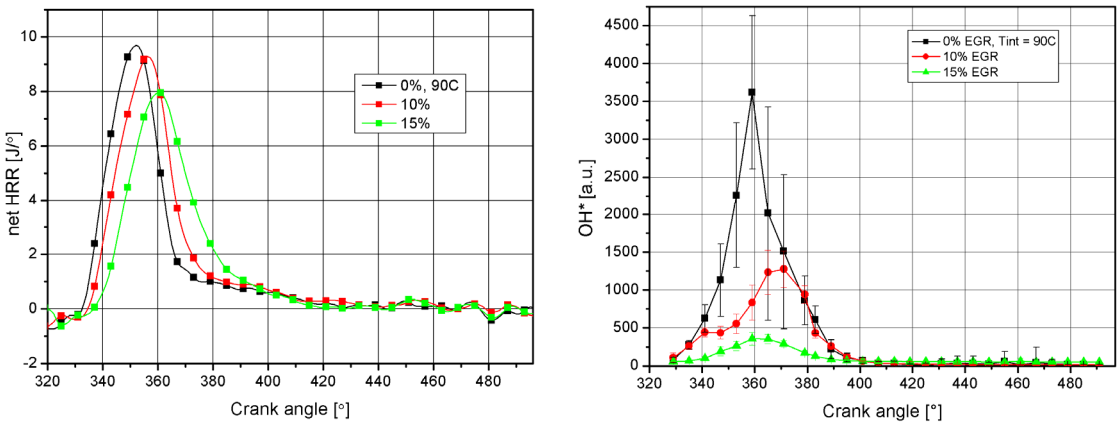


*Figure 8-22(a): The impact of EGR (nitrogen) on the heat release rate. Intake temperatures are kept constant at 90 °C. (b): OH-chemiluminescence for various amounts of EGR (nitrogen) added. Intake temperatures are kept constant at 90 °C.*

In agreement with the trend of IMEP dropping with increasing EGR, the heat release rate is reduced with its maximum delayed (Figure 8-22(a)). The OH* intensities (Figure 8-22(b)) are dropping significantly more than the HRR. It has to be kept in mind, that even though OH-chemiluminescence is somewhat correlated with the heat release rate, its intensity also depends on pressure, temperature and local equivalence ratio with a maximum at $\phi \approx$ 0.9 to 1.1 [Ikeda, Kaneko et al., 2001; Hardalupas and Orain, 2004]. Combustion temperatures are evidently lower for higher EGR rates due to the increased thermal capacity of the charge [Quader, 1971]. Also, the locally available oxygen concentration is reduced due to dilution, which leads to a higher equivalence ratio.

The cumulated heat release, as shown in Figure 8-23, is delayed with increasing EGR, as expected. The maximum heat release as an indicator of the efficiency of combustion is decreasing with larger amounts of EGR as well.

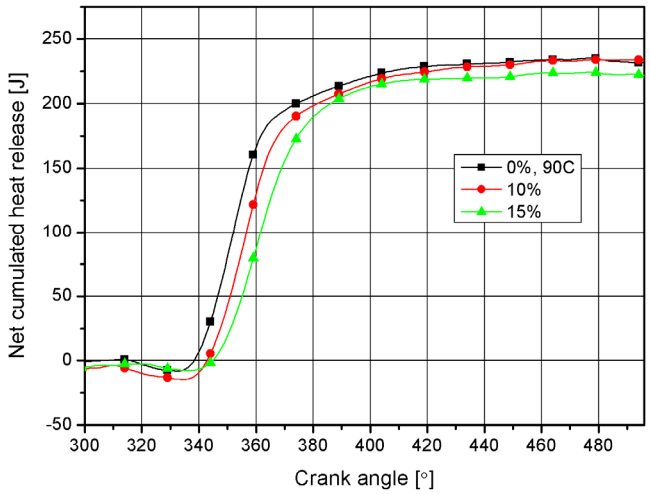


*Figure 8-23: Cumulative heat release rate for all EGR cases. Intake air temperature is constant at 90 °C.*

### 8.3.1 Combustion progress

The difference in heat release rate is reflected in the ensemble averaged OH images shown in Figure 8-24. The flame propagation is slowed down for higher EGR rates; as well as the chemiluminescence intensity being lower. The spatial intensity distribution is also altered. In the 0% EGR case the highest combustion activity is taking place in the center near the spark plug, while in the 15% EGR case highest OH levels can be found at the side opposing the spark in a crescent shape.

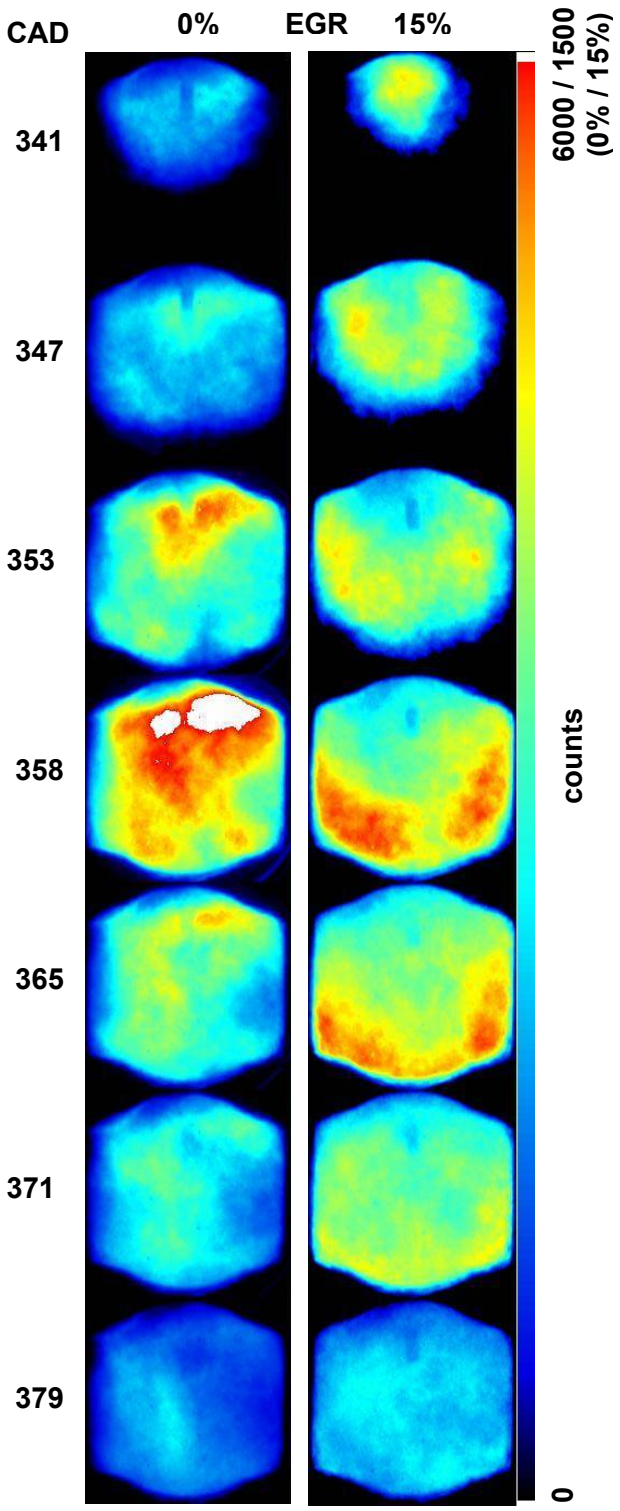


*Figure 8-24: OH images averaged over 50 cycles show the difference in flame propagation for 0 and 15% EGR.*

In Figure 8-25 individual images are shown for crank angles closest to the maximum heat release rate. Common for all images at 15% EGR is the visibly lower intensity. Even more pronounced than could be observed in the averaged images, there is more intensity at the lower section of the field of view on the side of the exhaust valves. The 0% EGR images have a tendency to display higher combustion activity around the spark plug (in the top section of the image). However, the images taken at 15% EGR rate more often show higher intensities close to the perimeter of the images.

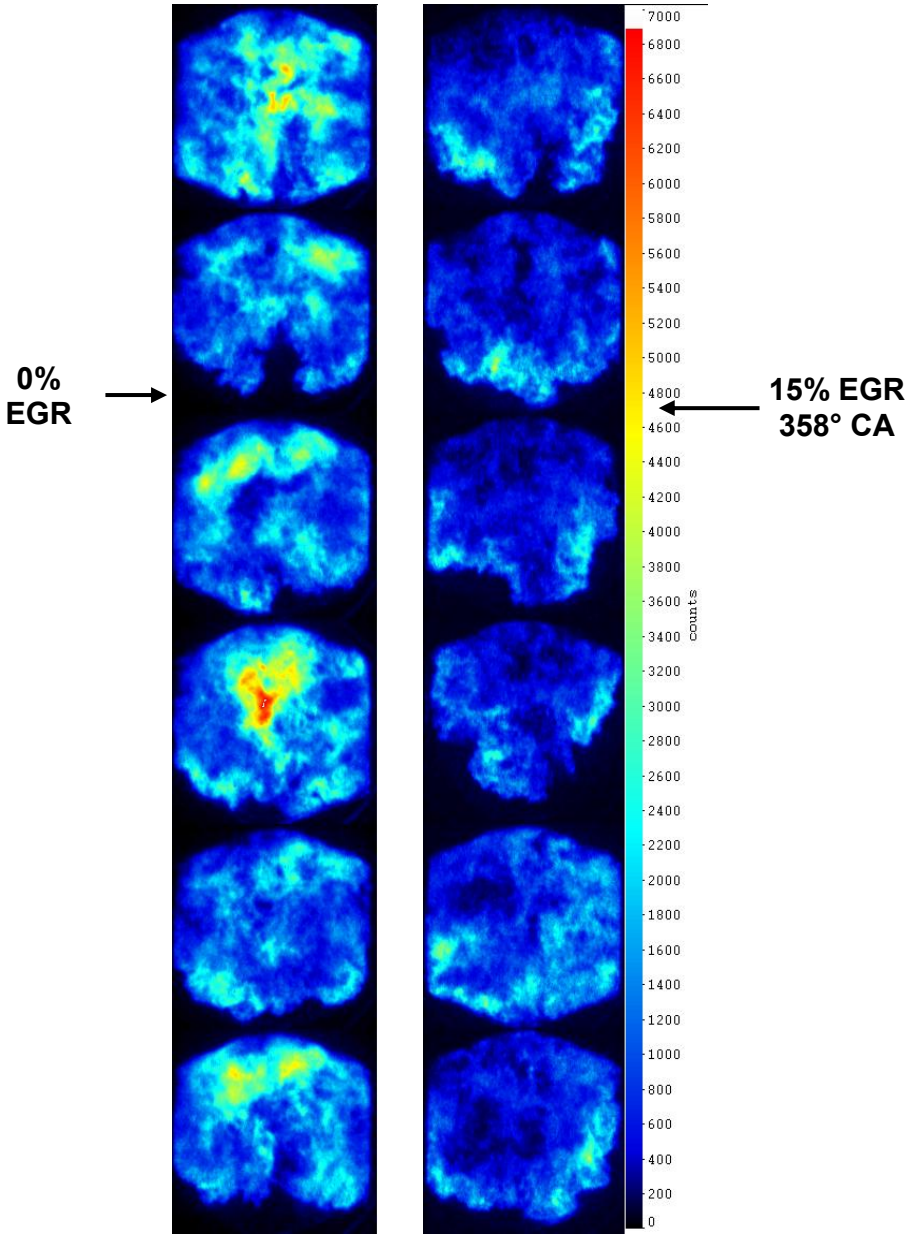


*Figure 8-25: Single OH images taken close to maximum heat release show the difference in flame propagation for 0 and 15% EGR.*

### 8.3.2 Nitric Oxide

The evolution of the in-cylinder NO concentration in the laser sheet plane is shown in Figure 8-26. The findings described reflect the influence of the high fuel stratification and the role of mixing for the measured level of local NO for the engine operating conditions studied here. Large cyclic variations of spatially averaged NO concentrations are observed, as indicated by the error bars. In agreement with the exhaust gas measurements, the LIF data show a strong decrease of NO concentrations with the addition of EGR.

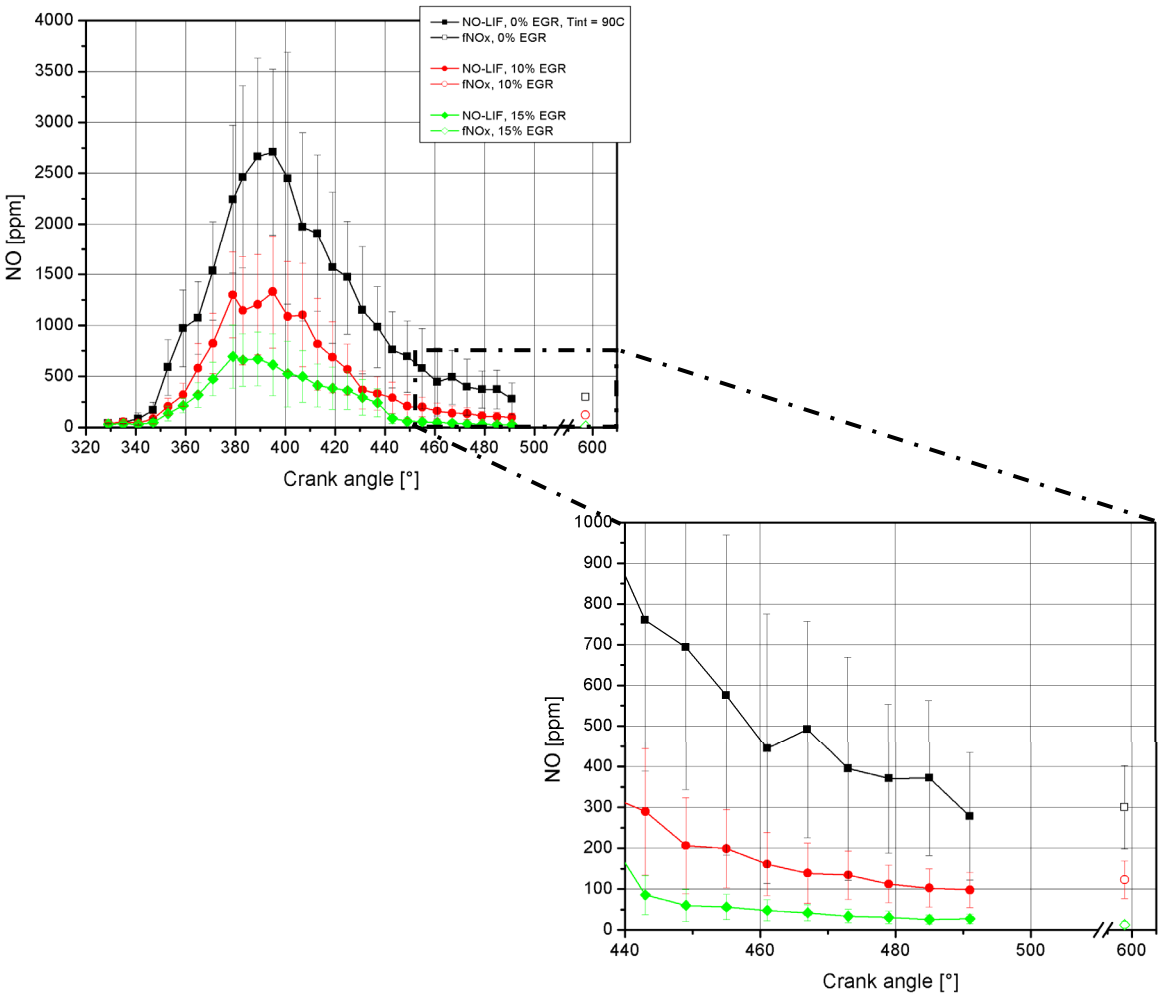


*Figure 8-26: Spatial average of NO mole fraction, ensemble averaged over 50 images. Error bars indicate the cyclic fluctuations. Late cycle NO concentrations (LIF) compare well to exhaust gas data.*

It is interesting to examine the evolution of NO mole fraction versus crank angle. The ratio of maximum concentration and that close to EVO is on the order of 8. This is high

compared with a factor of 4 to 5 that [Suck, Jakobs et al., 2004]obtained from measurements in a spray guided SIDI engine. They as well measure the highest concentrations around 390 CAD and observe a drop in concentration at approximately the same rate as measured in the present study during the expansion stroke. [Bessler, Schulz et al., 2001] conducted crank angle resolved NO LIF measurements (spatially averaged) in a SIDI engine operated in homogeneous mode. They found maximum concentrations between 380 and 395 CAD with concentration continuously dropping to about half the peak concentrations at 420 CAD. The concentrations obtained at that crank angle agreed well with exhaust gas measurements. It has to be emphasized that direct comparisons can only be of a qualitative nature, not only because of differing engine designs and operating conditions but also experimental factors such as size and location of the probed volume.

The blowup of Figure 8-26 illustrates how the exhaust gas measurements and averaged in-cylinder LIF concentrations taken at late crank angles agree for the cases investigated. For 0% and 10% EGR the agreement is very good, both in terms of averages and cyclic fluctuations. It should be kept in mind that NO concentrations for the highest EGR level are low and thus, the influence of noise in the NO LIF images may lead to a somewhat poorer agreement in that case. Yet, with the discussion of the spatial NO distribution for engine operation with different intake air temperature in mind it is also plausible that gas mixing effects may be more dominant for this operating condition. This will become more apparent through the examination of individual images as displayed in Figure 8-27 and a subsequent comparison of averaged and individual images.

The correlation between OH-chemiluminescence and NO concentration was investigated in Chapter 8.1.4. Some correlation was found for early crank angles when comparing OH-chemiluminescence and NO-LIF based concentrations. This correlation decreased for later crank angles and eventually disappeared for the comparison of OH-chemiluminescence and NO exhaust gas measurements (cycle-resolved!). In fact, this investigation was presented for engine operating conditions with 0% EGR, the same case studied here. Similar behavior for operation with some EGR is expected as a result from these previous studies. In Figure 8-27, single cycle images of OH-chemiluminescence and NO concentrations are presented on the same scale. While there are occasional matches in the spatial structures (high OH correlating with high NO etc.) this is not a

general observation. Clearly, the line-of-sight averaged images of OH-chemiluminescence will only correspond to NO concentration fields when the flames are predominantly structured in the horizontal plane of the laser sheet. Most pronounced, this effect can be observed when comparing the NO images that show large areas with no NO present to the corresponding OH image. Often, considerable levels of chemiluminescence are registered from areas above and/or below the laser sheet plane.

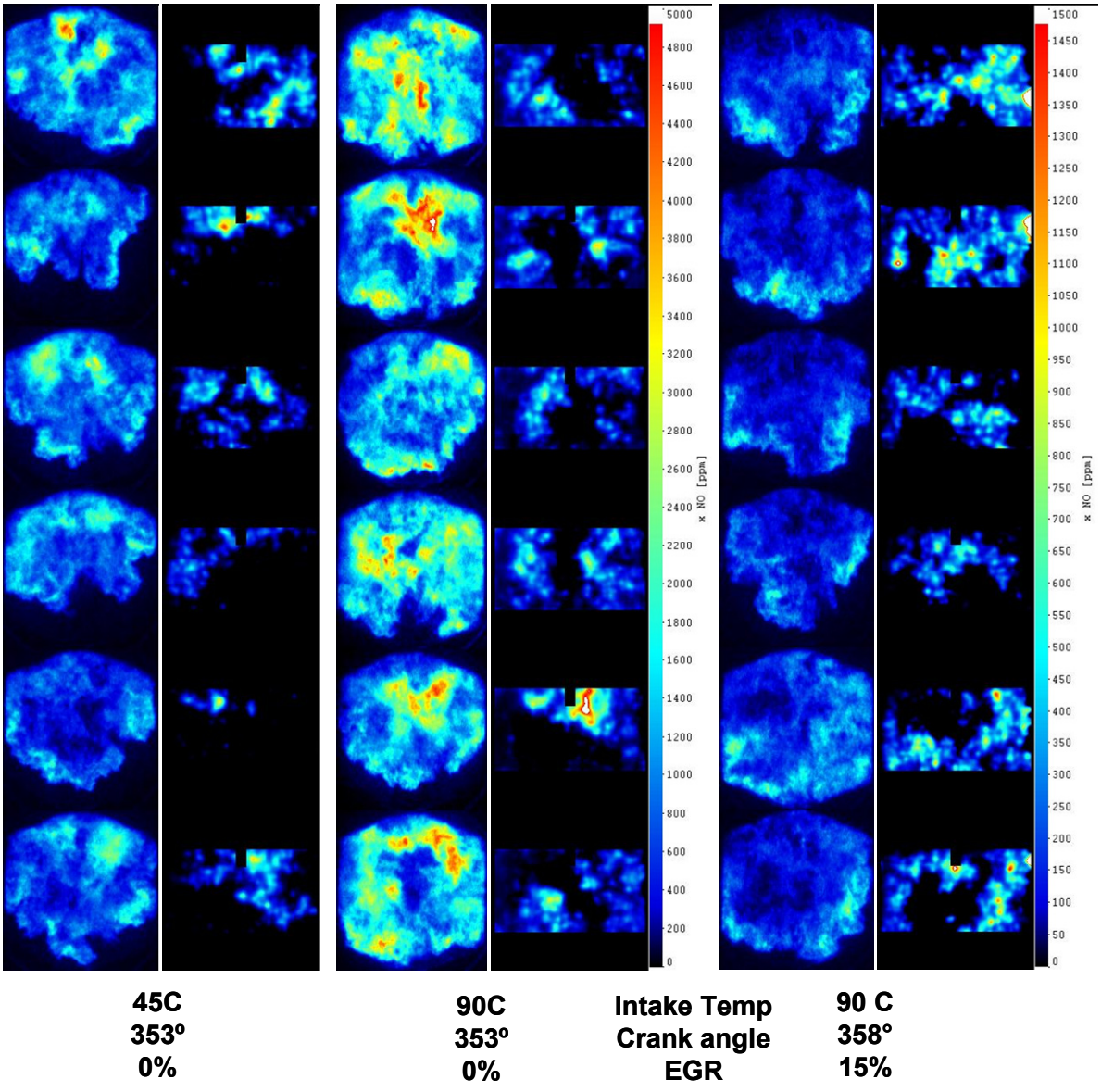


*Figure 8-27: Single OH*-images (1st, 3rd, and 5th column) and NO-images (2nd, 4th, and 6th column) taken at the crank angle of maximum heat release. Corresponding images were recorded simultaneously. The unit for the OH*- images is "counts" instead of "x NO", but the color scales are identical. Note the higher resolution for 15% EGR case.*

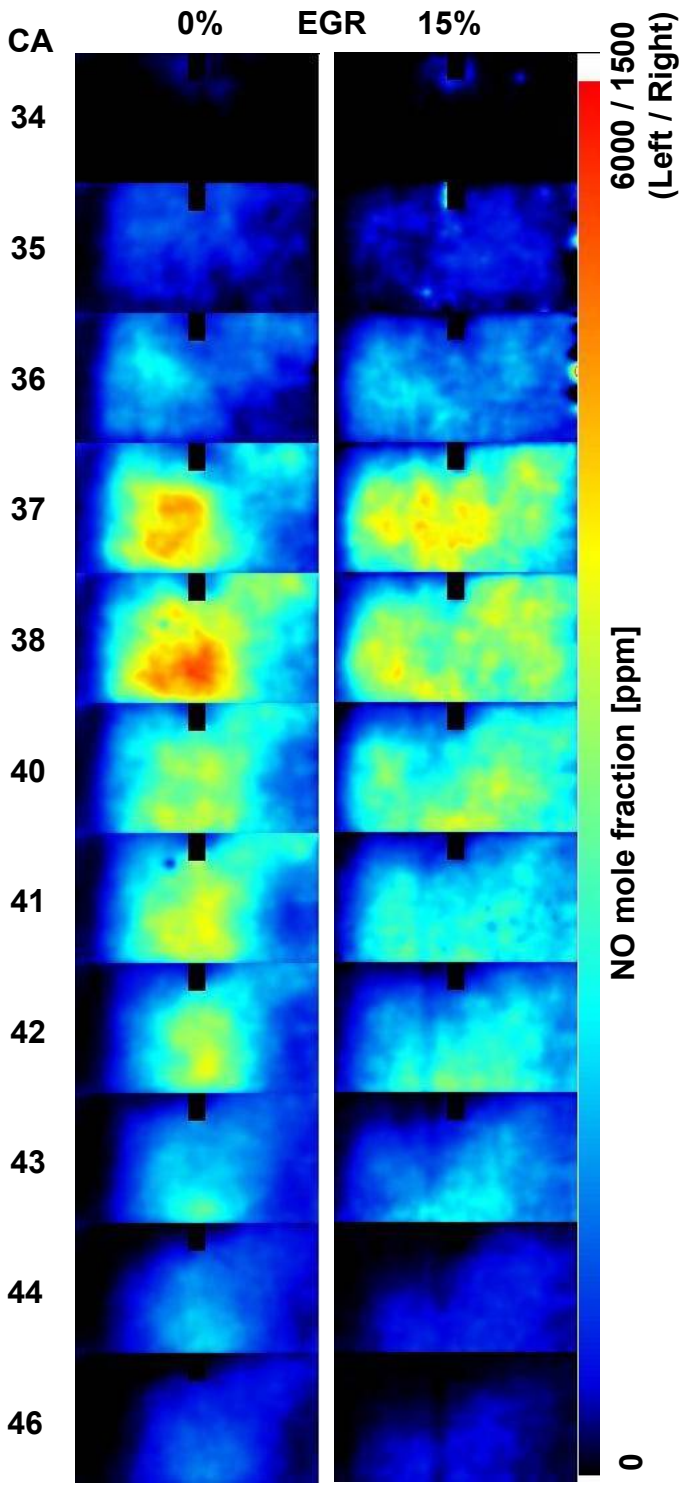


*Figure 8-28: Images of NO concentration averaged over 50 cycles for each crank angle for EGR rates of 0 and 15%.*

Figure 8-28 presents images of the nitric oxide concentration, averaged over 50 cycles, as a function of crank angle for 0% and 15% EGR operation. The most noteworthy

difference of the images taken with an EGR rate of 15% is the more homogeneous distribution of the NO. The highest concentrations are observed at a crank angle of 379 in both cases.

While at 389 CAD the image taken without EGR displays a high degree of stratification, in the 15% EGR case the highest concentrations are already much more dispersed. The areas of high concentrations disappear earlier in the stroke while at the same time shifting towards the periphery of the image with a bias towards the side opposed to the spark plug. A similar trend was observed in the OH images depicted Figure 16 as described above.

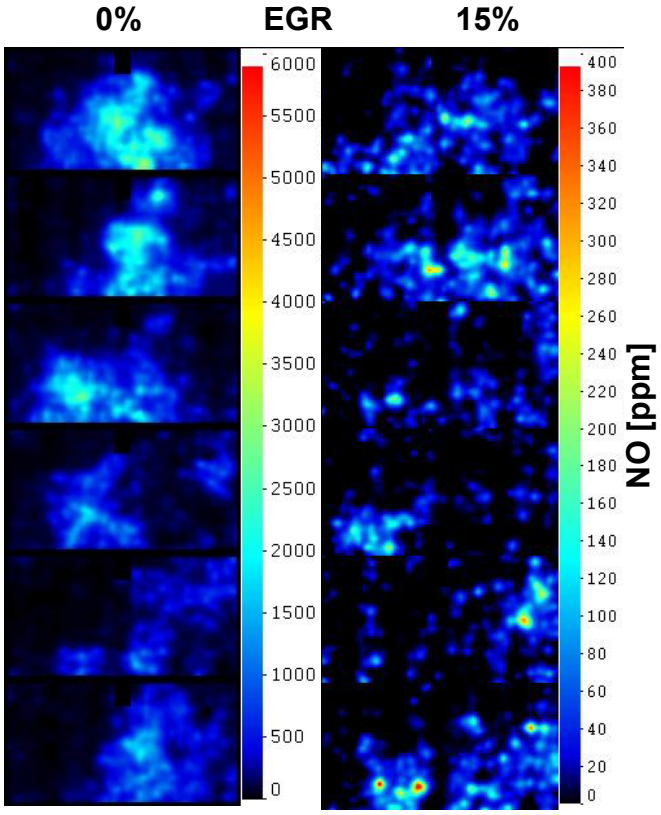


*Figure 8-29: These images show NO mole fraction measured in single cycles at 491 CAD. Note the scale for the 15% EGR case.*

It is noteworthy that the individual images of the mole fraction taken with high EGR show even more irregular distributions than the images taken without EGR. This is particularly true for images taken late in the stroke such as shown in Figure 8-29 and is apparent, despite the low concentrations and hence low signal to noise ratio. Spatial mixing effects, as discussed for the NO distributions measured for the intake air

temperature variation, once again seem to dominate the observed ensemble averaged NO concentration distribution. With more cyclic variations measured for high EGR levels, the ensemble average appears more homogeneous.

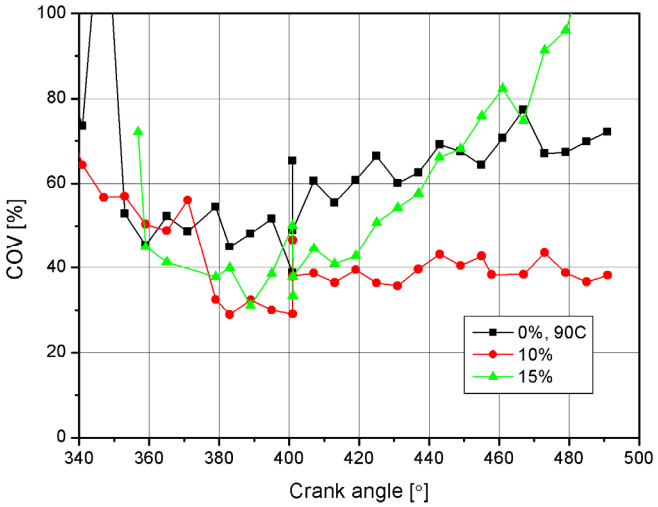


*Figure 8-30: Average coefficient of variance of NO mole fraction distribution over an image.*

To further illustrate the inhomogeneity in measured NO concentration distributions the coefficient of variation across individual images was examined. This will provide a measure of inhomogeneity allows a more quantitative comparison between different operating conditions [Reuss and Sick, 2005]. The COV of NO in-cylinder concentrations is lowest around 380 to 400 CAD as shown in Figure 8-30. This is after the end of combustion and most likely when the NO formation has ended due to decreasing pressures and temperatures. After that, local NO concentration distributions are governed by mixing due to the turbulent flow during the expansion stroke. Given the large scale inhomogeneity that was observed for the NO distributions, it is plausible to find high values for COV of NO concentration that may even increase during the expansion stroke. Again, recall that the NO LIF measurements probe only a small fraction of the in-cylinder volume.

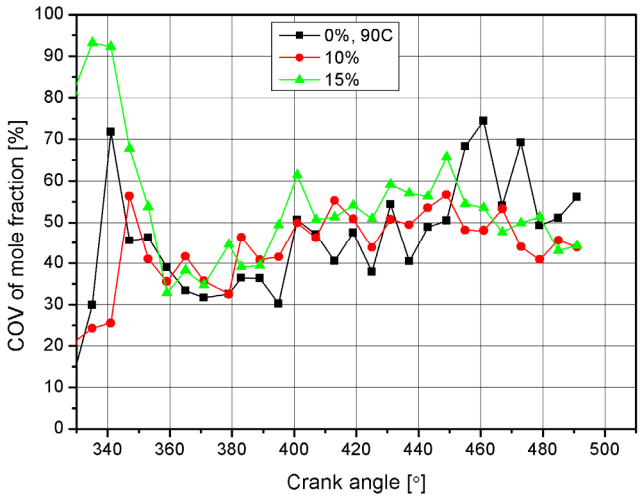


*Figure 8-31: Coefficient of variance of NO mole fraction from cycle to cycle*

The variation of the NO concentration from cycle to cycle is shown in Figure 8-31. Here, a minimum is found around 370 CAD. For later crank angles the COV increases. This is in part due to the temperature sensitivity characteristics of the signal and subsequently the corrections applied to the raw NO LIF signal (see Chapter 7.2.5 or [Fissenewert, 2005] for details). Around 370 CAD the temperatures are highest and the LIF signal is least temperature dependent. With increasing crank angle the temperatures drop eventually to levels where the inaccuracy of our temperature assumptions has an increasing impact on the correction factor that is calculated to process the LIF images. At crank angles before 370, the COV is more likely governed by the cyclic variability of the combustion. The increase in COV into the expansion stroke, again, may be just an artifact due to the increased temperature sensitivity. Note that on average, this effect seems to cancel if one compares the average NO concentration measured via LIF late in the cycles with those measured in the exhaust gas (see Figure 8-26).

In Figure 8-32 the NO mole fractions determined with LIF at a number of crank angles are compared to the exhaust gas measurement. This was done on an ensemble average basis of the cycle resolved exhaust gas measurement and the spatially averaged NO images. For each crank angle 50 images were evaluated, except for 401 CAD where 150 images were evaluated. The error bars symbolize one standard variation of the average as a measure of the cyclic variability. Best correlations were found at earlier crank angles.

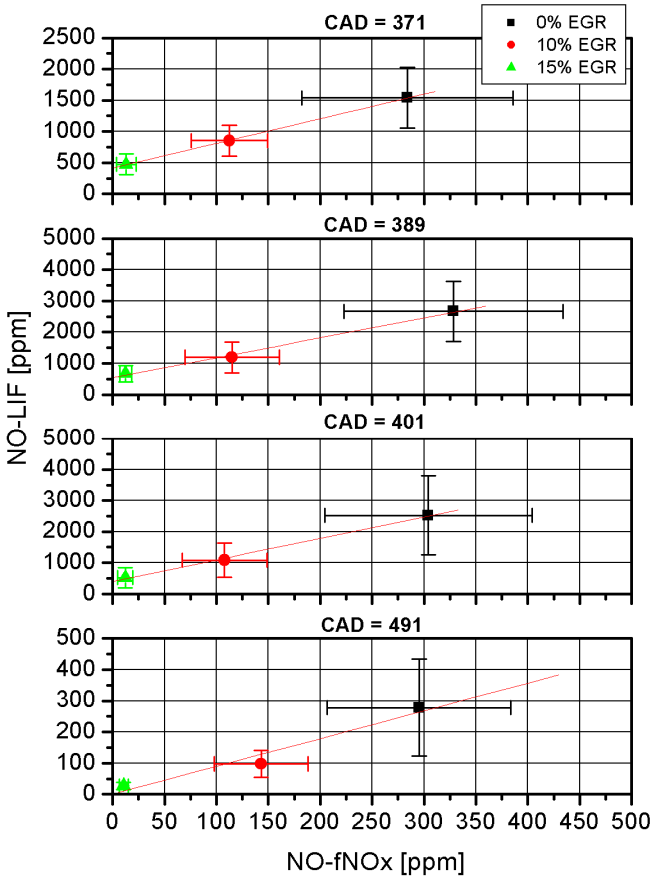


*Figure 8-32: Correlation of NO mole fraction measured with LIF and with the fast NO detector in the exhaust.*

The agreement at 491 CAD is good, albeit with large variations in the data from both measurements, which do not necessarily support the same trend on a single shot basis (Chapter 8.1.4)! Also, keep in mind that the accuracy of the in-cylinder measurements for single cycle data is reduced due to the increased level of importance of temperature-dependent corrections of the LIF signals

# 9 Conclusions

The formation of nitric oxide was investigated in a spray-guided spark-ignition direct-injection gasoline engine. Experiments were conducted in a single-cylinder optical engine simultaneously using planar laser-induced fluorescence of NO, fast NO exhaust gas detection, and imaging of OH chemiluminescence. The combination of these techniques allowed to validate the results of each measurement against each other, thus enabling a detailed insight of the NO formation process in this engine. Correlations have been found between engine out NO measurements and NO-LIF and between OH* and NO-LIF, but not between OH* and engine out NO. In addition thermodynamic results obtained with cylinder pressure analysis have been considered in the interpretation of the data obtained.

Of the three experimental methods used, the quantitative NO-PLIF imaging is the most complex and is therefore most error-prone. The parameters such as temperature and local equivalence ratios influencing the uncertainty of the NO-LIF measurement results have been carefully assessed. It could be shown that even with limited knowledge of these quantities meaningful results can be obtained.

One focus of the study was on cyclic variability. It turned out that looking at averaged results alone is insufficient, since these findings are not necessarily representative of single cycles.

## 9.1 Homogenous - Stratified

NO formation was investigated for early and late injection, i.e. homogeneous and stratified charge conditions.

The role of (unknown) spatial variations of temperature and gas composition on quantitative interpretation of NO PLIF images was addressed and found to remain an open issue in quantitative NO imaging diagnostics under IC engine conditions. Arguments for not correcting images for absorption effects were discussed.

OH* images provide a convenient means to evaluate the impact of changes in engine operating conditions on spatial and temporal flame propagation in the cylinder. Flame propagation is smooth for early injection conditions compared to late injection operation.

Under those conditions, the flames were found to exhibit strong spatial stratification – resembling the remaining structure of the fuel spray.

Similarly, instantaneous NO distributions have pronounced spatial concentration gradients for stratified engine operation – following the initial flame structure. The stratification in the NO distribution remains until very late in the exhaust stroke.

Despite some limitations towards truly quantitative NO concentration data within individual images, fluctuations and average data are in very good agreement with exhaust gas measurements. Cyclic fluctuations of in-cylinder NO decrease monotonically towards the exhaust stroke and stabilize at a COV of 20%. For stratified operation, the COV of NO remains at levels of 50% through the entire cycle. These results compare quite favorably with data from cycle-resolved NO exhaust gas measurements, where fluctuations of 16% and 19% were found for homogeneous operation and 34% for stratified charge operation.

No significant correlation of the in-cylinder NO measurements with the fast NO measurements in the exhaust on a cycle by cycle basis was found. In-cylinder stratification, even for early injection operation, seems to be large enough such that the amount of NO that is measured within the laser light sheet is not representative for the overall cylinder contents for the engine under investigation.

A significant correlation between OH* signals and NO PLIF data but not with engine-out NO emissions was found. OH* imaging could therefore not be used for an assessment of cyclic variations of total in-cylinder NO, i.e. engine-out NO.

### 9.2 Effect of Intake Air Temperature

The influence of variations in intake air temperature and simulated exhaust gas recirculation on the NO formation was examined.

Overall, it was found that cycle-resolved information is needed to explain the differences found between operating conditions, since the initial high stratification of fuel leads to large spatial gradients in the NO concentration.

An increase of the intake air temperature from 45°C to 90 °C increased the exhaust level NO concentration by a factor of three. In-cylinder measurements of NO concentrations in a horizontal plane that intersects the spark plug gap do not show the

same difference. Quite the contrary, spatially averaged NO concentrations can even be higher at some crank angles for lower intake air temperature operation. The examination of simultaneously recorded OH-chemiluminescence and NO concentration images show the dominating effect of high stratification of the initial fuel concentration and in turn local NO concentrations. Large scale mixing later in the expansion stroke disperses NO but by far not to a level where individual cycle in-cylinder measurements and exhaust gas samples would correlate.

### 9.3 Effect of Dilution

The addition of nitrogen to the intake air was used to simulate exhaust gas recirculation in a controlled manner. Up to 15% of the intake air was replaced and resulted in a drop of exhaust gas NO concentrations by a factor of ten. The ensemble average in-cylinder measurements late in the expansion stroke correlate well with the average exhaust gas measurements. A good correlation was found between averaged in-cylinder data and exhaust data for earlier crank angles as well. The coefficient of variation of cycle-resolved in-cylinder data taken late in the cycle and exhaust data are in good agreement as well. This is interesting since strong spatial NO gradients were observed until late in the expansion stroke.

As for the investigation of NO formation with intake air temperature variation, it was found that it was necessary to use the cycle-resolved OH-chemiluminescence and NO images to characterize the role of local inhomogeneity, introduced by the fuel stratification. Averaged in-cylinder NO distributions do not adequately reflect the formation process rather than show a smoothed distribution that may even be counter-intuitive based on averaged chemiluminescence data.

The strong impact of the high fuel stratification is also reflected in the temporal evolution of the in-cylinder NO concentrations. Spatially averaged peak concentrations can reach 2700 ppm for engine operation with 90 °C intake air temperature and no EGR. This compares to approximately 300 ppm as measured in the exhaust gas. This ratio is high for spark-ignition engines. However, given the high level of fuel stratification in this spray-guided engine, the observations are plausible and are supported by the measured high local concentrations of NO.

# 10 Future Work

As has been shown in the preceding chapter, the NO formation process can be comprehensively characterized with the combination of measurement techniques discussed in this thesis. There is certainly room for improvements of the experimental methods. Here, particularly the absorption of the laser light comes to mind, which introduces the biggest uncertainty to the NO-LIF measurements. Its dependence not only on burned gas composition and temperature but also path length through the burned region introduces the highest error to the NO-LIF measurements. The latter is hard to calculate as the usual assumption of a spherical flame front does not necessarily apply in a highly stratified combustion system. However, flame front information is available through the OH*-images. A laser path could be calculated on a line by line basis from these images, thus allowing a pixel by pixel correction of the NO images. The question is, whether the high computational effort is warranted by the improvement in accuracy. Additionally it leaves the uncertainty of temperature and composition. An improved absorption measurement setup including an assessment how much of the beam intensity is lost when passing the windows would be most beneficial.

A robust method for 2D temperature imaging could certainly prove useful in further improving accuracy not only with respect to absorption but also in regard to the correction for fluorescence quenching. As has been shown, the sensitivity of the latter to combustion temperature is small above approximately 1700K. So a real improvement in accuracy of the NO-LIF results could only be achieved in the later part of the expansion stroke.

It has been shown that the OH signal correlates with the simultaneously measured NO-LIF signal, but not with the engine out measurements. Measurements with a fast camera such as a CMOS camera in combination with an image intensifier might improve both correlations through enabling measurements with a higher repetition rate. Now a time history of the OH chemiluminescence can be recorded with a resolution of better than 1 CAD. Integrating this signal over the investigated cycle might give a better assessment of the overall chemiluminescence activity in that cycle. The cycle-integrated OH signal

might therefore correlate better with the exhaust gas measurements, which represent a time integrated signal as well.

While a high repetition camera can easily be employed to record crank angle resolved OH chemiluminescence, the application to NO-LIF is more difficult. Here the limiting factor is the maximum repetition rate of commercially available excimer lasers, which is restricted to approximately 100 Hz. Nonetheless, this would allow two NO-LIF images in the same cycle. The spatially averaged signal of each image could now be compared to spatially averaged OH*-signal taken slightly earlier in the same cycle. This way it could be accounted for the time the reaction from OH to NO needs to take place. It is conceivable that this approach would yield a better correlation between the two signals.

The establishment of a statistically relevant relationship between OH* and NO would eventually allow to replace direct NO measurements with OH* imaging. This would constitute a significant improvement, since quantitative NO measurements require an immense experimental and computational effort.

Besides improvements of the experimental techniques, it would be interesting to further investigate the impact of EGR on the NO formation within this particular combustion system. [Ladommatos, Abdelhalim et al., 1996a] were able to separate the effects, by which EGR reduces NO formation, into a dilution, a thermal and a chemical mechanism. (See also [Ladommatos, Abdelhalim et al., 1996b; Ladommatos, Abdelhalim et al., 1997a; Ladommatos, Abdelhalim et al., 1997b]). Their work was done on a conventional (non-transparent) diesel engine. It would be useful to apply their methods to the transparent SIDI engine and combine them with optical measurements.

# 11 Bibliography


Akihama, K., Fujikawa, T.*, et al.* (1998), *"Laser-induced fluorescence imaging of NO in a port-fuel-injected, stratified-charge SI engine~Correlations between NO formation region and stratified fuel distribution,"* SAE Paper, (981430).

Alkidas, A. C. and El Tahry, S. H. (2003), *"Contributors to the fuel economy advantage of DISI engines over PFI engines,"* SAE Paper, (2003-01-3101).

Alkidas, A. C., Lippert, A. M.*, et al.* (2002), *"Fuel Economy and Engine-Out Emissions from a Single -Cylinder Two Valve Direct-Injection S.I. Engine Operating in the Stratified-Combustion Regime,"* SAE Paper, (2002-01-2658).

Arnberg, B. T. (1962), *"Review of Critical Flowmeters for Gas Flow Measurements,"* Journal of Basic Engineering.

Ball, J., Stone, C.*, et al.* (1999), *"Cycle-by-cycle modelling of NO formation and comparison with experimental data,"* Journal of Automobile Engineering, **213**, (D2), 176-89.

Banwell, C. N. and McCash, E. M. (1994), *"Fundamentals of molecular spectroscopy,"* London ; New York, McGraw-Hill.

Bessler, W. G. (2003), *"Quantitative Nitric Oxide Concentration and Temperature Imaging in Flames over a Wide Pressure Range with Laser-Induced Fluorescence,"* Dissertation, Ruprecht-Karls-Universität, Heidelberg.

Bessler, W. G., Hofmann, M.*, et al.* (2004), *"Quantitative in-cylinder NO-LIF imaging in a realistic gasoline engine with spray guided direct injection,"* Proc. Comb. Inst., Chicago.

Bessler, W. G., Schulz, C.*, et al.* (2001), *"Quantitative In-Cylinder NO-LIF Imaging in a Direct-Injected Gasoline Engine with Exhaust Gas Recirculation,"* SAE Paper, (2001-01-1978).

Bessler, W. G., Schulz, C.*, et al.* (2002), *"Strategies for laser-induced fluorescence detection of nitric oxide in high-pressure flames. I. A–X(0,0) excitation,"* Applied Optics-LP, (18), 3547-57.

Bessler, W. G., Schulz , C.*, et al.* (2003), *"Carbon dioxide UV laser-induced fluorescence in high-pressure flames,"* Chem. Phys. Lett, (375), 344–49.

Bessler, W. G., Schulz, C.*, et al.* (2003a), *"Strategies for laser-induced fluorescence detection of nitric oxide in high-pressure flames. II. A–X(0,1) excitation,"* Applied Optics-LP, (12), 2031 - 42.

Bessler, W. G., Schulz, C.*, et al.* (2003b), *"Strategies for laser-induced fluorescence detection of nitric oxide in high-pressure flames. III. Comparison of A–X excitation schemes,"* Applied Optics-LP, (24), 4922 - 36.

Bessler, W. G., Schulz, C.*, et al.* (2003), *"A versatile modeling tool for nitric oxide LIF spectra,"* Proceedings of the Third Joint Meeting of the U.S. Sections of The Combustion Institute, Chicago, paper PI05.

Bowditch, F. W. (1961), *"A New Tool for Combustion Engine Research - A Quartz Piston Engine,"* SAE Paper, (610002).

Bowman, C. T. (1992), *"Control of Combustion Generated Nitric Oxide Emissions: Technology Driven By Regulation,"* Proc. Comb. Inst., Sydney, Combustion Institute.

Bräumer, A., Sick, V.*, et al.* (1995), *"Quantitative two-dimensional measurements of nitric oxide and temperature distributions in a transparent square piston SI engine,"* SAE Paper, (952462).

Britton, C. L. (1998), *"The Critical Flow Function, C*, For Humid Air,"* ASME Fluids Engineering Division Summer Meeting.

Caron, R. and Kegel, T. (1996), *""From NIST To Under The Hood": Flow Measurement Traceability at Ford,"* 42nd International Instrumentation Symposium.

Cole, R. L., Poola, R. B.*, et al.* (1998), *"Exhaust emissions of a vehicle with a gasoline direct-injection engine,"* SAE Paper, (982605).

Collier, T. and Gregory, D. (2000), *"Investigation into the Performance of an Ultrafast Response NO Analyser Equipped with a NO2 to NO Converter for Gasoline and Diesel Exhaust NOx Measurements,"* SAE Paper, (2000-01-2954).

Corcione, F. E., Merola, S. S.*, et al.* (2002), *"Absolute NO and OH concentrations during diesel combustion process by multiwavelength absorption spectroscopy,"* SAE Paper, (2002-01-0892).

Daily, J. W. (1997), *"Laser induced fluorescence spectroscopy in flames,"* Progress in Energy and Combustion Science, **23**, (2), 133-99.

Dec, J. E. and Canaan, R. E. (1998), *"PLIF imaging of NO formation in a DI diesel engine,"* SAE Paper, (980147).

Drake, M. C., Fansler, T. D.*, et al.* (2004), *"Stratified Charge Combustion: Modeling and Imaging of a Spray-Guided Injection Spark-Ignition Engine,"* Proc. Comb. Inst., Chicago.

Drake, M. C., Fansler, T. D.*, et al.* (2003), *"Piston fuel films as a source of smoke and hydrocarbon emissions from a wall-controlled spark-ignited direct- injection engine,"* SAE Paper, (2003-01-0547).

Driscoll, J. J., Sick, V.*, et al.* (2002), *"Measurements of NO Distributions and Fluorescence Lifetimes in a Nonpremixed Counterflow $CH_4$ / Air Flame using Picosecond Time-resolved Laser Induced Fluorescence,"* Proc. Comb. Inst.

Eckbreth, A. C. (1996), *"Laser diagnostics for combustion temperature and species,"* Amsterdam, The Netherlands, Gordon and Breach Publishers.

Fansler, T. D., Drake, M. C.*, et al.* (2003), *"Local fuel concentration, ignition and combustion in a stratified charge spark ignited direct injection engine: spectroscopic, imaging and pressure-based measurements,"* Int J Engine Research, (2), 61 - 86.

Fenimore, C. P. (1978), *"Studies of Fuel- Nitrogen Species in Rich Flame Gases,"* Proc. Comb. Inst., Leeds, England, The Combustion Institute.

Fischer, J., Kettner, M.*, et al.* (2002), *"Influence of an Adjustable Tumble System on In Cylinder Air Motion and Stratification in a Gasoline Direct Injection Engine,"* SAE Paper, (2002-01-1645).

Fissenewert, U. (1999), *"The Design of a Single Cylinder Engine Featuring Optical Access,"* Diplomarbeit, Technische Universität Berlin - University of Michigan, Berlin - Ann Arbor.

Fissenewert, U. (2005), *"Characterization of combustion and NO formation in a spray-guided gasoline direct-injection engine using chemilumines-cence imaging, NO-PLIF, and fast NO exhaust gas analysis,"* SAE Paper, (2005-01-2089).
Ford, R. and Collins, N. (1999), *"Measurement of residual gas fraction using a fast response NO sensor,"* SAE Paper, (1999-01-0208).
Frieden, D. and Sick, V. (2003), *"Investigation of the fuel injection, mixing and combustion processes in an SIDI engine using quasi-3D LIF imaging,"* SAE Paper, (2003-01-0068).
Geiger, J., Grigo, M.*, et al.* (1999), *"Direct injection gasoline engines~Combustion and design,"* SAE Paper, (1999-01-0170).
Gilmore, F. R. (1965), *"Potential energy curves for N2, NO, O2 and corresponding ions,"* Journal of Quantitative Spectroscopy and Radiative Transfer, **5**, (2), 369-89.
Glassman, I. (1996), *"Combustion,"* San Diego, Calif, Academic Press.
Haber, L. C. and Vandsburger, U. (2003), *"A Global Reaction Model For OH* Chemiluminescence Applied to a Laminar Flat-Flame Burner,"* Combustion Science and Technology, **175**, (10), 1859 - 91.
Hardalupas, Y. and Orain, M. (2004), *"Local measurements of the time-dependent heat release rate and equivalence ratio using chemiluminescent emission from a flame,"* Comb. Flame, **139**, (3), 188-207.
Heywood, J. B. (1988), *"Internal Combustion Engine Fundamentals,"* New York :, McGraw-Hill,.
Hildenbrand, F., Schulz, C.*, et al.* (1999), *"In Cylinder NO-LIF Imaging in a Realistic GDI Engine Using KrF Excimer Laser Excitation,"* SAE Paper, (1999-01-3545).
Hildenbrand, F., Schulz, C.*, et al.* (2001), *"Quantitative laser diagnostic studies of the NO distribution in a DI diesel engine with PLN and CR injection systems,"* SAE Paper, (2001-01-3500).
Hildenbrand, F., Schulz , C.*, et al.* (1998), *"Laser spectroscopic investigation of flow fields and NO formation in a realistic SI engine,"* SAE Paper, (980148).
Honda, T., Kawamoto, M.*, et al.* (2004), *"A Study of Mixture Formation and Combustion for Spray Guided Disi,"* SAE Paper, (2004-01-0046).
Ikeda, Y., Kaneko, M.*, et al.* (2001), *"Local A/F measurement by chemiluminescence OH*, CH* and C2* in SI engine,"* SAE Paper, (2001-01-0919).
Jackson, N. S., Stokes, J.*, et al.* (1997), *"Stratified and homogeneous charge operation for the direct-injection gasoline engine~High power with low fuel consumption and emissions,"* SAE Paper, (970543).
Jamette, P., V.Ricordeau*, et al.* (2001), *"Laser Induced Fluorescence Detection of NO in the Combustion Chamber of an Optical GDI Engine with A-X(0,1) Excitation,"* SAE Paper, (2001-01-1926).
Jones, E. H. and Seidel, W. F. (1997), *"Recent Advancement in Critical Flow Venturi Nozzle Technology,"* ASME Fluids Engineering Division Summer Meeting.
Josefsson, G., Magnusson, I.*, et al.* (1998), *"Multidimensional laser diagnostic and numerical analysis of NO formation in a gasoline engine.,"* Proc. Comb. Inst.
Krebs, R., Pott, E.*, et al.* (2002), *"Exhaust Gas Aftertreatment of Volkswagen FSI Fuel Stratified Injection Engines,"* SAE Paper, (2002-01-0346).

Kume, T., Iwamoto, Y., *et al.* (1996), *"Combustion Control Technologies for Direct Injection SI Engine,"* SAE Paper, (960600).
Ladommatos, N., Abdelhalim, S. M., *et al.* (1996a), *"The dilution, chemical, and thermal effects of exhaust gas recirculation on diesel engine emissions~Part 1: Effect of reducing inlet charge oxygen,"* SAE Paper, (961165).
Ladommatos, N., Abdelhalim, S. M., *et al.* (1996b), *"The dilution, chemical, and thermal effects of exhaust gas recirculation on diesel engine emissions~Part 2: Effects of carbon dioxide,"* SAE Paper, (961167).
Ladommatos, N., Abdelhalim, S. M., *et al.* (1997a), *"The dilution, chemical, and thermal effects of exhaust gas recirculation on diesel engine emissions~Part 3: effects of water vapor,"* SAE Paper, (971659).
Ladommatos, N., Abdelhalim, S. M., *et al.* (1997b), *"The dilution, chemical, and thermal effects of exhaust gas recirculation on diesel engine emissions~Part 4: effects of carbon dioxide and water vapor,"* SAE Paper, (971660).
Lavoie, G. A., Heywood, J. B., *et al.* (1970), *"Experimental and Theoretical Investigation of Nitric Oxide Formation in Internal Combustion Engines,"* Comb. Sci. Tech., **1**, 313-26.
Martz, J. (2000), Personal communication.
Millar, G. H., Gilllig, E., *et al.* (1961), *"Engine Air Flow Measurements with laminar Flow Elements,"* SAE Paper, (610002).
Müller, E. and Zillmer, M. (1998), *"Modeling of nitric oxide and soot formation in diesel engine combustion,"* SAE Paper, (982457).
N.N. (1999a), "ASM Handbook, American Society for Metals, **1**.
N.N. (1999b), "ASM Handbook, American Society for Metals, **2**.
N.N. (2003a), Glass Sealing Alloys : Thermal Expansion Table.
N.N. (2003b), Mechanical Properties of Optical Materials: Thermal.
Najm, H. N., Paul, P. H., *et al.* (1998), *"On the Adequacy of Certain Experimental Observables as Measurements of Flame Burning Rate,"* Comb. Flame, **113**, (3), 312-32.
Ortmann, R., Arndt, S., *et al.* (2001), *"Methods and Analysis of Fuel Injection, Mixture Preparation and Charge Stratification in Different Direct Injected SI Engines,"* SAE Paper, (2001-01-0970).
Parish, S. (2003), Personal Communication: The Injector Calibration and Uncertainity.
Peckham, M., Hands, T., *et al.* (1998a), *"Fast Response NO/HC Measurements in the Cylinder and Exhaust Port of a DI Diesel Engine,"* SAE Paper, (980788).
Peckham, M., Hands, T., *et al.* (1998b), *"Real Time In-Cylinder and Exhaust NO Measurements in a Production SI Engine,"* SAE Paper, (980400).
Polak, T. A., Pande, C., *et al.* (1999a), "Chapter 6 - Fluid Flow Measurement," "*Engineering measurements electronic resource : methods and intrinsic errors*, London, Knovel Professional Engineering.
Polak, T. A., Pande, C., *et al.* (1999b), "Chapter 10 - Internal Combustion Engine Testing," "*Engineering measurements electronic resource : methods and intrinsic errors*, London, Knovel Professional Engineering.
Preussner, C., Döring, C., *et al.* (1998), *"GDI: interaction between mixture preparation, combustion system and injector performance,"* SAE Paper, (980498).

Puzinauskas, P. V., Olsen, D. B.*, et al.* (2003), *"Mass integration of fast-response NO measurements from a two-stroke large-bore natural gas engine,"* Int. J. Engine Research, **4**, (3), 233-48.
Quader, A. A. (1971), *"Why intake charge dilution decreases nitric oxide emission from spark ignition engines,"* SAE Paper, (710009).
Reuss, D. L. and Sick, V. (2005), *"Inhomogeneities in HCCI Combustion: An Imaging Study,"* SAE Paper, (2005-01-2122).
Rosseel, E., Sierens, R.*, et al.* (1999), *"Evaluating piezo-electric transducer response to thermal shock from in-cylinder pressure data,"* SAE Paper, (1999-01-0935).
Schänzlin, K. (2003), Experimenteller Beitrag zur Charakterisierung der Gemischbildung und Verbrennung in einem direkteigespritzten, strahlgefuehrten Ottomotor, VDI.
Scherenberg, H. (1961), *"Der Erfolg der Benzin-Einspritzung bei Daimler-Benz,"* MTZ, **22**, (7), 241.
Schießl, R., Dreizler, A.*, et al.* (1999), *"Comparison of different ways for image post-processing: detection of flame fronts,"* SAE Paper, (1999-01-3651).
Schulz , C., Gronki, J.*, et al.* (2002), *"Temperature-dependent absorption by CO2: Implications for UV diagnostics in high-temperature flames,"* LACEA, Boulder, Colorado.
Schulz , C., Jeffries, J. B.*, et al.* (2002), *"Impact of UV Absorption by CO2 and H2O on NO LIF in High-Pressure Combustion Applications,"* Proceedings of the Combustion Institute.
Schulz, C., Koch, J. D.*, et al.* (2002), *"Ultraviolet absorption spectra of shock-heated carbon dioxide and water between 900 and 3050 K,"* Chem. Phys. Lett, **355**, (1-2), 82-88.
Schulz , C., Sick, V.*, et al.* (1999), *"Quantification of NO A X (0, 2) Laser-Induced Fluorescence: Investigation of Calibration and Collisional Influences in High-Pressure Flames,"* Applied Optics, **38**, (9), 1434 -43.
Schulz , C., Wolfrum, J.*, et al.* (1998), *"Comparative study of experimental and numerical NO profiles in SI combustion.,"* Proceedings of the Combustion Institute.
Schulz, C., Yip, B.*, et al.* (1995), *"A Laser-Induced Fluorescence Scheme for Imaging Nitric Oxide in Engines.,"* Chem. Phys. Lett, (242), p. 259-64.
Sick, V., Decker, M.*, et al.* (1996), *"Collisional Processes in the B state of O2,"* Chem. Phys. Lett, (249), p.335-40.
Sick, V., Hildenbrand, F.*, et al.* (1998), *"Quantitative laser-based measurements and detailed chemical kinetic modeling of nitric oxide concentrations in methane/air counterflow diffusion flames,"* Proc. Comb. Inst.
Solomon, A. S. and Szekely, G. A. (2003), *"Combustion Charakteristics of a Reverse-Tumble Wall-Controlled Direct Injection Stratified-Charge Engine,"* SAE Paper, (2003-01-0543).
Stan, C., Stanciu, A.*, et al.* (2004), *"GDI Compact Four Stroke Engine - an Advanced Concept for Vehicle Application,"* SAE Paper, (2004-01-0039).
Stoffels, G. G. M., Boom, E. J. v. d.*, et al.* (1999), *"In-Cylinder Measurement of NO Formation in a Diesel Engine,"* SAE Paper, (1999-01-1487).
Stojkovic, B. D., Fansler, T. D.*, et al.* (2003), *"Quantitative high-speed imaging of soot temperature and relative concentration in a spark-ignited direct injection*

*engine.,"* 3rd Joint Meeting of the US Sections of the Combustion Institute, Chicago, Ill, The Combustion Institute.

Stojkovic, B. D., Fansler, T. D.*, et al.* (2004), *"High-Speed Imaging of OH* and Soot Temperature and Concentration in a Stratified-Charge Direct-Injection Gasoline Engine,"* Proc. Comb. Inst., Chicago.

Stone, C. R. (1989), *"Air flow measurement in internal combustion engines,"* SAE Paper, (890242).

Suck, G., Jakobs, J.*, et al.* (2004), *"NO laser-induced fluorescence imaging in the combustion chamber of a spray-guided direct-injection gasoline engine,"* SAE Paper, (2004-01-1918).

Tamura, Y., Kikuchi, S.*, et al.* (2001), *"Development of advanced emission-control technologies for gasoline direct- injection engines,"* SAE Paper, (2001-01-0254).

Taylor, C. F. (1985), *"The Internal-Combustion Engine in Theory and Practice,"* Cambridge, Mass. :, M.I.T. Press,.

Warnatz, J., Maas, U.*, et al.* (2001), *"Verbrennung,"* Berlin, Heidelberg, New York, Springer.

Wermuth, N. and Sick, V. (2005), *"Absorption and fluorescence quantum yield at elevated pressures and temperatures using an optical engine,"* SAE Paper, (2005-01-2090).

Zeldovich, Y. B. (1946), *"The Oxidation of Nitrogen in Combustion and Explosions,"* Acta Physicochem. , (21), 557.

Zhang, R., Wermuth, N.*, et al.* (2004), *"Impact of Fluorescence Tracers on Combustion Performance in Optical Engine Experiments,"* SAE Paper, (2004-01-2975).

Zhao, F., Harrington, D.*, et al.* (2002), *"Automotive Gasoline Direct Injection Engine*, SAE.

Zhao, F., Lai, M.-C.*, et al.* (1999), *"Automotive spark-ignited direct-injection gasoline engines,"* Progress in Energy and Combustion Science, **25**, (5), 437-562.

Zhao, H. and Ladommatos, N. (2001), *"Engine Combustion Instrumentation and Diagnostics,"* Warrendale, Pa. :, Society of Automotive Engineers,.